

# STRIDES: Spectroscopic and photometric characterization of the environment and effects of mass along the line of sight to the gravitational lenses DES J0408–5354 and WGD 2038–4008

E. J. Buckley-Geer,<sup>1\*</sup> H. Lin,<sup>1</sup> C. E. Rusu,<sup>2</sup> J. Poh,<sup>3,4</sup> A. Palmese,<sup>1</sup> A. Agnello,<sup>5</sup> L. Christensen,<sup>5</sup> J. Frieman,<sup>1,3,4</sup> A. J. Shajib,<sup>6</sup> T. Treu,<sup>6</sup> T. Collett,<sup>7</sup> S. Birrer,<sup>6,8</sup> T. Anguita,<sup>9,10</sup> C. D. Fassnacht,<sup>11</sup> G. Meylan,<sup>12</sup> S. Mukherjee,<sup>13</sup> K. C. Wong,<sup>14</sup> M. Aguena,<sup>15,16</sup> S. Allam,<sup>1</sup> S. Avila,<sup>17</sup> E. Bertin,<sup>18,19</sup> S. Bhargava,<sup>20</sup> D. Brooks,<sup>21</sup> A. Carnero Rosell,<sup>22</sup> M. Carrasco Kind,<sup>23,24</sup> J. Carretero,<sup>25</sup> F. J. Castander,<sup>26,27</sup> M. Costanzi,<sup>28,29</sup> L. N. da Costa,<sup>16,30</sup> J. De Vicente,<sup>22</sup> S. Desai,<sup>31</sup> H. T. Diehl,<sup>1</sup> P. Doel,<sup>21</sup> T. F. Eifler,<sup>32,33</sup> S. Everett,<sup>34</sup> B. Flaugher,<sup>1</sup> P. Fosalba,<sup>26,27</sup> J. García-Bellido,<sup>17</sup> E. Gaztanaga,<sup>26,27</sup> D. Gruen,<sup>35,36,37</sup> R. A. Gruendl,<sup>23,24</sup> J. Gschwend,<sup>16,30</sup> G. Gutierrez,<sup>1</sup> S. R. Hinton,<sup>38</sup> K. Honscheid,<sup>39,40</sup> D. J. James,<sup>41</sup> K. Kuehn,<sup>42,43</sup> N. Kuropatkin,<sup>1</sup> M. A. G. Maia,<sup>16,30</sup> J. L. Marshall,<sup>44</sup> P. Melchior,<sup>45</sup> F. Menanteau,<sup>23,24</sup> R. Miquel,<sup>46,25</sup> R. L. C. Ogando,<sup>16,30</sup> F. Paz-Chinchón,<sup>23,24</sup> A. A. Plazas,<sup>45</sup> E. Sanchez,<sup>22</sup> V. Scarpine,<sup>1</sup> M. Schubnell,<sup>47</sup> S. Serrano,<sup>26,27</sup> I. Sevilla-Noarbe,<sup>22</sup> M. Smith,<sup>48</sup> M. Soares-Santos,<sup>49</sup> E. Suchyta,<sup>50</sup> M. E. C. Swanson,<sup>24</sup> G. Tarle,<sup>47</sup> D. L. Tucker,<sup>1</sup> and T. N. Varga<sup>51,52</sup>

(The DES Collaboration)

*Affiliations appear at the end of the paper*

Accepted XXX. Received YYY; in original form ZZZ

## ABSTRACT

In time-delay cosmography, three of the key ingredients are 1) determining the velocity dispersion of the lensing galaxy, 2) identifying galaxies and groups along the line of sight with sufficient proximity and mass to be included in the mass model, and 3) estimating the external convergence  $\kappa_{\text{ext}}$  from less massive structures that are not included in the mass model. We present results on all three of these ingredients for two time-delay lensed **quad** quasar systems, DES J0408–5354 and WGD 2038–4008. We use the Gemini, Magellan and VLT telescopes to obtain spectra to both measure the stellar velocity dispersions of the main lensing galaxies and to identify the line-of-sight galaxies in these systems. Next, we identify 10 groups in DES J0408–5354 and 2 groups in WGD 2038–4008 using a group-finding algorithm. We then identify the most significant galaxy and galaxy-group perturbers using the "flexion shift" criterion. We determine the probability distribution function of the external convergence  $\kappa_{\text{ext}}$  for both of these systems based on our spectroscopy and on the DES-only multiband wide-field observations. Using weighted galaxy counts, calibrated based on the Millennium Simulation, we find that DES J0408–5354 is located in a significantly underdense environment, leading to a tight (width  $\sim 3\%$ ), negative-value  $\kappa_{\text{ext}}$  distribution. On the other hand, WGD 2038–4008 is located in an environment of close to unit density, and its low source redshift results in a much tighter  $\kappa_{\text{ext}}$  of  $\sim 1\%$ , as long as no external shear constraints are imposed.

**Key words:** gravitational lensing: strong – quasars: individual: DES J0408–5354, WGD 2038–4008 – galaxies: groups: general

1 **1 INTRODUCTION**

2 When a source with a time-varying luminosity such as a quasar or  
 3 a supernova undergoes strong gravitational lensing, the light reach-  
 4 ing the observer from the multiple images takes different paths and  
 5 hence different travel times. It was noted by Refsdal (1964) that  
 6 these time-delays between the images can be used to measure cos-  
 7 mological distances and the Hubble constant  $H_0$ . In recent years, the  
 8  $H_0$  Lenses in COSMOGRAIL’s Wellspring (HOLiCOW) collabora-  
 9 tion has been leading an active time-delay cosmography program  
 10 to measure  $H_0$  using lensed quasars, see Suyu et al. (2017); Wong  
 11 et al. (2019) and references therein. For a recent review of the field  
 12 of time-delay cosmography see Treu & Marshall (2016). The sig-  
 13 nificant improvements in the uncertainty in the measurements of  
 14  $H_0$  in the last two decades have come from the understanding of  
 15 the key ingredients required to achieve an accurate measurement. In  
 16 particular, three of these ingredients are: 1) determining the velocity  
 17 dispersion of the lensing galaxy, 2) identifying galaxies and groups  
 18 along the line of sight that are close enough to the lens and massive  
 19 enough to be included in the mass model, and 3) estimating the ex-  
 20 ternal convergence  $\kappa_{\text{ext}}$  due to less massive structures that are not in-  
 21 cluded explicitly in the mass model. In this work, we present results  
 22 on these three ingredients for two time-delay lensed quasar systems,  
 23 DES J0408–5354 (source redshift  $z_s = 2.375$ , main deflector red-  
 24 shift  $z_d = 0.5967$ , Lin et al. 2017) and WGD 2038–4008 ( $z_s = 0.777$ ,  
 25  $z_d = 0.2283$ , Agnello et al. 2018), as part of the STRong Lensing  
 26 Insights into the Dark Energy Survey (STRIDES) campaign (Treu  
 27 et al. 2018), an external collaboration of the Dark Energy Survey.

28 It has been known for sometime that including stellar kinemat-  
 29 ics of the lensing galaxy allows one to break the degeneracies inher-  
 30 ent in the mass profile of the lens (Treu & Koopmans 2002). To ob-  
 31 tain the stellar velocity dispersion of the lens we took spectroscopic  
 32 observations of the main lensing galaxy in DES J0408–5354 and  
 33 WGD 2038–4008.

34 If the perturbers along the line of sight are not explicitly ac-  
 35 counted for in the lens modeling, these perturbations can result in  
 36 systematic errors of order a few percent in the inferred value of  
 37  $H_0$ . To reduce such systematics, we identify galaxies and galaxy  
 38 groups in the fields of DES J0408–5354 and WGD 2038–4008 that  
 39 may significantly impact the lensing potential of the system. These  
 40 galaxies and galaxy groups will be included in the lens models for  
 41 both DES J0408–5354 (Shajib et al. 2019a, Yildirim et al. in prep)  
 42 and WGD 2038–4008 (Wong et al. in prep).

43 To identify the most significant perturbing galaxies and galaxy  
 44 groups, we use the “flexion shift” diagnostic proposed by McCully  
 45 et al. (2014, 2017), which has also been used in the line-of-sight  
 46 analysis of the HOLiCOW lenses HE 0435–1223 (Sluse et al. 2017)  
 47 and WFI 2033–4723 (Sluse et al. 2019). This diagnostic estimates  
 48 the difference in lensed image positions caused by the leading order  
 49 non-tidal (i.e. third-order) perturbation produced by a nearby galaxy  
 50 or galaxy group. McCully et al. (2017) showed that by explicitly  
 51 modeling perturbers with flexion shifts larger than the conservative  
 52 limit of  $\Delta_{3x} > 10^{-4}''$ , we can constrain the bias on  $H_0$  due to this  
 53 uncertainty to the percent level.

54 In addition, we determine for both systems the probability  
 55 distribution function of the external convergence  $\kappa_{\text{ext}}$  due to less  
 56 massive structures, which do not need to be explicitly incorporated  
 57 in the mass modeling, but nonetheless contribute a uniform mass-  
 58 sheet. Indeed, if unaccounted for, this quantity would bias  $H_0$  such  
 59 that  $H_0 = H_0^{\text{model}}(1 - \kappa_{\text{ext}})$  (e.g., Suyu et al. 2010a), for  $H_0^{\text{model}}$   
 60 obtained from lens modeling. For the first time we determine  $\kappa_{\text{ext}}$   
 61 based on multi-band (*griz*), wide-field images obtained from the

62 Dark Energy Survey<sup>1</sup> (DES) data. Following previous work (Fass-  
 63 nacht et al. 2011; Greene et al. 2013; Rusu et al. 2017; Rusu et al.  
 64 2019; Birrer et al. 2019; Chen et al. 2019), we measure the un-  
 65 der/overdensity of the line of sight towards both lens systems rela-  
 66 tive to the “average” line of sight density throughout the Universe,  
 67 obtained from the cosmologically representative sample provided  
 68 by the DES in the form of a set of control fields. Aiming to con-  
 69 strain  $\kappa_{\text{ext}}$  as tightly as possible, as well as to study the effect of  
 70 different analysis choices, we determine under/overdensities using  
 71 various combinations of weighting schemes for the galaxy counts,  
 72 such as the radial distance to the lens/field center and the redshift.  
 73 Finally, we convert the measured under/overdensities into a  $\kappa_{\text{ext}}$   
 74 distribution, using ray-tracing through the Millennium Simulation  
 75 (MS; Springel et al. 2005). We explore several aperture sizes, and  
 76 two different photometric redshift algorithms, which we further test  
 77 through simulations.

78 We perform a spectroscopic survey to obtain redshifts of galax-  
 79 ies in the fields of DES J0408–5354 and WGD 2038–4008. This  
 80 redshift data is used to identify galaxy groups located in the envi-  
 81 ronment or along the line of sight to these strong lensing systems  
 82 as well as in the calculation of the under/overdensity of the line of  
 83 sight towards both lens systems.

84 The structure of this paper is as follows. In Section 2 we de-  
 85 scribe our photometric and spectroscopic data, and in Section 3 we  
 86 present our techniques to measure redshifts and stellar masses. In  
 87 Section 4 we derive the stellar velocity dispersions for the main  
 88 lensing galaxies in the two systems, and in Section 5 we describe  
 89 our technique to identify galaxy groups. In Section 6 we identi-  
 90 fy the structures which can potentially affect the modeling of  
 91 the lensing systems. In Section 7 we present our measurement of  
 92 the relative weighted galaxy count ratios for DES J0408–5354 and  
 93 WGD 2038–4008, including accounting for relevant errors. In Sec-  
 94 tion 8 we use ray-tracing through the MS in order to obtain  $P(\kappa_{\text{ext}})$   
 95 for the measured ratios, and present our tests for robustness. Finally,  
 96 we conclude in Section 9.

97 The current work represents one of a series of papers from the  
 98 STRIDES collaboration, which together aim to obtain an accurate  
 99 and precise estimate of  $H_0$  with a blinded approach, from a com-  
 100 prehensive modelling of DES J0408–5354 and WGD 2038–4008.  
 101 In particular, lens modeling is performed by two independent mod-  
 102 eling teams (Shajib et al. 2019a, as well as Yildirim et al. in prep,  
 103 Wong et al. in prep), both of which make use of the stellar velocity  
 104 dispersion, environment and line-of-sight constraints derived in the  
 105 present work. Throughout this paper, we assume a flat  $\Lambda$ CDM cos-  
 106 mology with  $H_0 = 70 \text{ km s}^{-1} \text{ Mpc}^{-1}$ ,  $\Omega_m = 0.3$  for convenience  
 107 when estimating physical individual galaxy and galaxy group prop-  
 108 erties (§5–§6). However, in the latter part of the analysis, where we  
 109 determine the under/overdensities of the fields of the lenses and then  
 110 derive  $\kappa_{\text{ext}}$  distributions using ray-tracing through the MS, we adopt  
 111 the MS cosmology,  $\Omega_m = 0.25$ ,  $\Omega_\lambda = 0.75$ ,  $h = 0.73$ ,  $\sigma_8 = 0.9$  for  
 112 consistency. This is not expected to have a significant effect on the  
 113 inference of  $H_0$  (see Section 8). We present all magnitudes in the  
 114 AB system. We define all standard deviations as the semi-difference  
 115 between the 84th and 16th percentiles.

<sup>1</sup> <https://www.darkenergysurvey.org>

## 2 DATA

The Dark Energy Survey (DES) is a deep sky survey that was carried out using the Dark Energy Camera (DECam, [Flaugher et al. 2015](#)) located on the Blanco 4m telescope at the Cerro Tololo Inter-American Observatory in the Chilean Andes. The survey ran from 2013–2019 ([Diehl et al. 2019](#)) and covered  $\sim 5100$  sq. degs of the southern sky in five optical filters (*grizY*). The DES data are processed by the DES Data Management team (DESDM, [Morganson et al. 2018](#)) to produce annual data releases that consist of coadded images and object catalogs. We have used two data sets for the work described here, the first year of DES data which is referred to as DES Year 1 (Y1) and the first three years known as DES Year 3 (Y3). The median single epoch PSF FWHM in the *i*-band is  $0.88''$  and the coadd magnitude limit in the *i*-band is 23.44. More details of the survey data can be found in [Abbott et al. \(2018\)](#).

### 2.1 Spectroscopic Observations

Spectroscopic observations were carried out using three instruments: (1) the Gemini Multi-Object Spectrograph (GMOS-S) on the Gemini South telescope; (2) the Low Dispersion Survey Spectrograph (LDSS-3) on the Magellan Clay telescope; and (3) the Multi Unit Spectroscopic Explorer (MUSE) on the European Southern Observatory (ESO) Very Large Telescope (VLT) Unit Telescope 4 (UT4). Table 1 summarizes details of the spectroscopic data taken using these three telescope+instrument setups.

The GMOS-S observations were taken as part of two programs: (1) a Gemini Large and Long Program (LLP; PI: E. Buckley-Geer; program IDs GS-2015B-LP-5 and GS-2017A-LP-5) of spectroscopic follow-up for DES strong lensing systems and for DES photometric redshift (photo-*z*) calibrations; and (2) a dedicated program (PI: H. Lin; program ID GS-2018B-Q-220) to observe line-of-sight galaxy redshifts and lensing galaxy velocity dispersions for our two lensed quasar systems. These programs observed a total of four GMOS-S multi-object spectroscopy (MOS) masks for DES J0408–5354 and two masks for WGD 2038–4008, and the data were taken in queue mode on Gemini South during the semesters 2015B, 2017A, and 2018B. Nearly all the masks were each observed using both the GMOS-S B600 and R400 gratings, in order to provide spectral coverage over both blue and red wavelength ranges, respectively, spanning approximately  $3800\text{\AA}$ – $7500\text{\AA}$  and  $5000\text{\AA}$ – $10500\text{\AA}$ . Multiple science exposures were taken to reject cosmic rays, and the grating central wavelength was dithered slightly for different exposures to fill in wavelength gaps due to spatial gaps between the three GMOS-S CCDs. Flat field and wavelength calibration exposures were interspersed with the science exposures.

The LDSS-3 observations were taken as part of a semester 2018A Magellan program (PI: J. Frieman) to obtain line-of-sight galaxy spectroscopy for DES J0408–5354 and two other lensed quad quasar systems. Four LDSS-3 MOS masks were observed for DES J0408–5354 over the two nights 2018 January 21,22 UT. Each mask was observed using the LDSS-3 VPH-All grism, with wavelength coverage of about  $3800\text{\AA}$ – $10500\text{\AA}$ . Multiple science exposures were taken to reject cosmic rays. Flat field and wavelength calibration exposures were taken immediately before and after the sequence of science exposures.

The VLT MUSE observations were taken as part of an ESO program (0102.A-0600(E), PI: A. Agnello) to do integral field spectroscopy of DES J0408–5354 and its surrounding field. The MUSE observations were done in wide-field mode with adaptive optics cor-

**Table 1.** Spectroscopic observations for the DES J0408–5354 and WGD 2038–4008 systems.

Telescope/Instrument			
Mask/Cube	Grating/ Grism	UT Date	Exposure time (sec)
DES J0408–5354			
Gemini South/GMOS-S			
(1) DESJ0408-5354_42	B600	2015 Dec 09	$4 \times 900$
(2) DESJ0408-5354_42	R400	2015 Dec 09	$4 \times 900$
(3) DESJ0408-5354_45	B600	2017 Apr 26–27	$5 \times 900$
(4) DESJ0408-5354_45	R400	2017 Mar 30–31	$4 \times 900$
(5) DESJ0408-5354_A	B600	2018 Dec 04	$4 \times 900$
(6) DESJ0408-5354_A2	R400	2019 Feb 04	$6 \times 1000$
(7) DESJ0408-5354_B	B600	2018 Dec 09	$4 \times 900$
(8) DESJ0408-5354_B	R400	2018 Dec 09	$4 \times 900$
Magellan Clay/LDSS-3			
(9) des0408a	VPH-All	2018 Jan 21	$7 \times 780$
(10) des0408b	VPH-All	2018 Jan 21	$6 \times 780$
(11) des0408c	VPH-All	2018 Jan 22	$7 \times 780$
(12) des0408d	VPH-All	2018 Jan 22	$6 \times 780$
VLT UT4/MUSE			
(13) MUSE		2019 Jan 11,13	14400
WGD 2038–4008			
Gemini South/GMOS-S			
(14) DESJ2038-4008_A	B600	2018 Nov 06	$4 \times 900$
(15) DESJ2038-4008_A	R400	2018 Nov 07	$4 \times 900$
(16) DESJ2038-4008_B	B600	2018 Nov 07	$4 \times 900$

rections and were carried out over the two nights 2019 Jan 11 and 13. The final MUSE data cube covered an area of  $92'' \times 95''$ , and the wavelength coverage spanned  $4700\text{\AA}$ – $5803\text{\AA}$  and  $5966\text{\AA}$ – $9350\text{\AA}$ . Additional spectroscopic analysis of the MUSE data and further details of the observations and data processing are given in [Shajib et al. \(2019a\)](#).

### 2.2 Spectroscopic target selection

Galaxy targets for the Gemini and Magellan masks were selected using DES photometry. The exact selection criteria changed somewhat with time, due to improvements in DES photometric measurements, star-galaxy separation, and object catalogs. Specifically, three sets of selection criteria were used for the masks in Table 1, listed below in order from earliest to latest in time.

(A) *Gemini South masks (1)–(4)*: Galaxies were selected from the DES Year 1 (Y1) “Y1A1 COADD” catalog ([Drica-Wagner et al. 2018](#)), using the *i*-band SExtractor AUTO magnitude ([Bertin & Arnouts 1996](#)) cuts  $20 \leq \text{MAG\_AUTO\_I} < 22.5$ . No Milky Way extinction corrections were applied to the magnitudes before selection. Star-galaxy separation used the SExtractor SPREAD\_MODEL classifier ([Desai et al. 2012](#)), also in the *i*-band:  $\text{SPREAD\_MODEL\_I} > 0.002$ .

(B) *Magellan masks (9)–(12)*: Galaxy targets were now selected from the deeper DES Year 3 (Y3) data set, specifically from the “Y3 GOLD” (Sevilla et al. in prep) version 1.0 catalog, using the *i*-band magnitude cuts  $18 \leq \text{MAG\_AUTO\_I} < 23$ , in particular extending the faint magnitude limit fainter to aim for a deeper sample. Again no Milky Way extinction corrections were applied to the magnitudes. Star-galaxy separation used the same *i*-band cut:  $\text{SPREAD\_MODEL\_I} > 0.002$ .

(C) *Gemini South masks (5)–(8) and (14)–(16)*: These masks were the latest to be designed and therefore used improved selection methods compared to the masks in (A) and (B). Galaxies were again selected from the “Y3 GOLD” data set, but using the most current version 2.2 catalog. We also changed the selection magnitudes from AUTO to MOF (Drlica-Wagner et al. 2018, Sevilla et al. in prep) magnitudes, where the latter provide improved photometry, based on simultaneous multiepoch, multiband, and multiobject fits. The adopted *i*-band cuts were  $15 \leq \text{MOF\_CM\_MAG\_CORRECTED\_I} < 23$ , where these MOF magnitudes also included Milky Way extinction corrections and several other sub-percent photometric zeropoint corrections (Sevilla et al. in prep). Finally, we also updated the star-galaxy separation classifier to EXTENDED\_CLASS\_MASH\_MOF (Sevilla et al. in prep), specifically using the cuts  $\text{EXTENDED\_CLASS\_MASH\_MOF} = 3$  (indicating “high confidence galaxies”) or 2 (indicating “mostly galaxies”). For  $i \leq 22.5$ , this classification should yield a galaxy efficiency  $> 98.5\%$  and a stellar contamination  $< 1\%$  (Sevilla et al. in prep).

Each Magellan LDSS-3 and Gemini South GMOS-S mask included galaxy targets distributed over about a  $5.5' \times 5.5'$  sky area centered on each lensed quasar system. Generally one to three slits on each mask were manually designed to target objects in or close to the lensed quasar system, e.g., to measure the redshift or velocity dispersion of the main lensing galaxy in each system, or to observe close nearby neighbor galaxies of the systems. The remaining targets were selected automatically by GMPMS<sup>2</sup> or maskgen<sup>3</sup>, the respective GMOS-S or LDSS-3 mask design software, both of which designed masks to maximize the number of targets observed. The potential set of galaxies that could be targeted was subject to the selection criteria described above. In addition, at the time each mask was designed, we removed from the initial target list any galaxies which already had high-confidence redshifts from previous observations, or which were already targeted on companion masks designed for the same semester’s (Gemini) observing queue or (Magellan) observing run. Moreover, for the Magellan LDSS-3 targets (only), we assigned targeting priorities as inputs to maskgen, depending on the *i*-band magnitude and on the radius from the DES J0408–5354 quad system. Specifically, for galaxies with radius  $\leq 3'$ , we assigned priorities based on MAG\_AUTO\_I (as in criteria (B) above), with highest priority given to bright galaxies  $\text{MAG\_AUTO\_I} < 19.5$ , next priority to galaxies otherwise brighter than  $\text{MAG\_AUTO\_I} = 22$ , and lowest priority to galaxies otherwise brighter than  $\text{MAG\_AUTO\_I} = 23$ . Finally, for galaxies with radius  $> 3'$ , we assigned lower priorities than for galaxies  $\leq 3'$ , and these priorities were tied linearly to MAG\_AUTO\_I (with brighter galaxies at higher priority).

### 2.3 Data for the determination of the line-of-sight under/overdensities

In order to determine the line-of-sight under/overdensities for DES J0408–5354 and WGD 2038–4008 we need a catalog of galaxy properties that includes magnitudes and photometric redshifts. We have used the catalogs from the Year 3 Gold version 2.2 catalog.

We have used the photometric redshifts computed using the DNF machine-learning algorithm described in De Vicente et al.

<sup>2</sup> <https://gmpms-documentation.readthedocs.io/en/latest/>

<sup>3</sup> <https://code.obs.carnegiescience.edu/maskgen>

(2016). We also repeat the analysis using the photometric redshifts derived with the Bayesian Photometric Redshift (BPZ: Benítez 2000; Hoyle et al. 2018) method. If an object has a spectroscopic redshift from Gemini or Magellan, as described below in §3.1, then we use that redshift instead of the photometric redshift. In Figure 1 we show the comparison of the photometric redshifts from the DNF algorithm to the spectroscopic redshifts for objects with  $i < 22.5$ . The comparison of the DNF and BPZ photo-*z*’s for the objects that only have photometric redshifts is shown also in Figure 1 for both DES J0408–5354 and WGD 2038–4008. We observe that there is no obvious mismatch between the two algorithms so we have used results from both of them in the subsequent analysis. We note that the photometric redshifts are computed using the photometry in the *griz* filters only, as Hoyle et al. (2018) have found that the *Y*-band adds little to no predictive power.

#### 2.3.1 The Control Field: DES

To to apply the weighted number counts technique we need a control field against which to determine an under/overdensity, the constraint we will eventually use to determine  $P(\kappa_{\text{ext}})$ . As both lensing systems are within the DES footprint we have chosen to use the full DES survey footprint of 5100 sq. deg to provide our control field. This differs from our approach in the past, where we have used control fields observed with the *Hubble Space Telescope (HST)* (Suyu et al. 2010b; Fassnacht et al. 2011; Suyu et al. 2013; Greene et al. 2013), and from CFHTLenS (Heymans et al. 2012), (e.g., Rusu et al. 2017; Rusu et al. 2019; Birrer et al. 2019; Chen et al. 2019). The choice of control fields from DES itself, as opposed to other large-scale cosmological surveys, is optimal. This choice avoids potential biases to which our technique of obtaining  $\kappa_{\text{ext}}$  from weighted number count ratios may be sensitive, such as due to mismatches in image resolution, depth and star-galaxy classification between the lens (target) fields and the control fields (e.g., Rusu et al. 2017). The full Year 6 DES survey footprint consists of 10169 tiles, each  $10,000 \times 10,000$  pixels or 0.53 sq deg in area. We take a sample of tiles from the center of the footprint that are far from the survey edges and also eliminate tiles that contain very bright stars or very large galaxies. This results in a total of 5402 tiles of which we select 843 from across the survey footprint. For each tile we select six fields each of  $1000 \times 1000$  pixels. This gives us a total of 5094 control fields spread over the sky and covering  $\approx 27$  sq deg. The location of these six fields are shown in Figure 2 for one of the DES tiles. This should allow us to account for sample variance.

#### 2.3.2 The galaxy samples for the target and control fields

For the target fields we make an initial selection of all objects from the Y3 Gold catalog that fall within a  $4' \times 4'$  box centered on the lens. For the control fields we make the same selection but using the center of the control field. We select all objects that satisfy  $\text{FLAGS\_GOLD} = 0$  and  $\text{EXTENDED\_CLASS\_SOF} \geq 2$ , which selects galaxies<sup>4</sup>. We are using the Single-Object Fitting (SOF) magnitudes that are computed using a simplified version of the Multi-Object Fitting (MOF) algorithm described in section 6.3 of Drlica-

<sup>4</sup> When comparing with the available *HST* data, we found that five objects in the WGD 2038–4008 field are erroneously classified by this pipeline, mainly in the form of stars wrongly classified as galaxies. As some of these are close enough to the lens to bias the inference described below, we were careful to correct the classification.

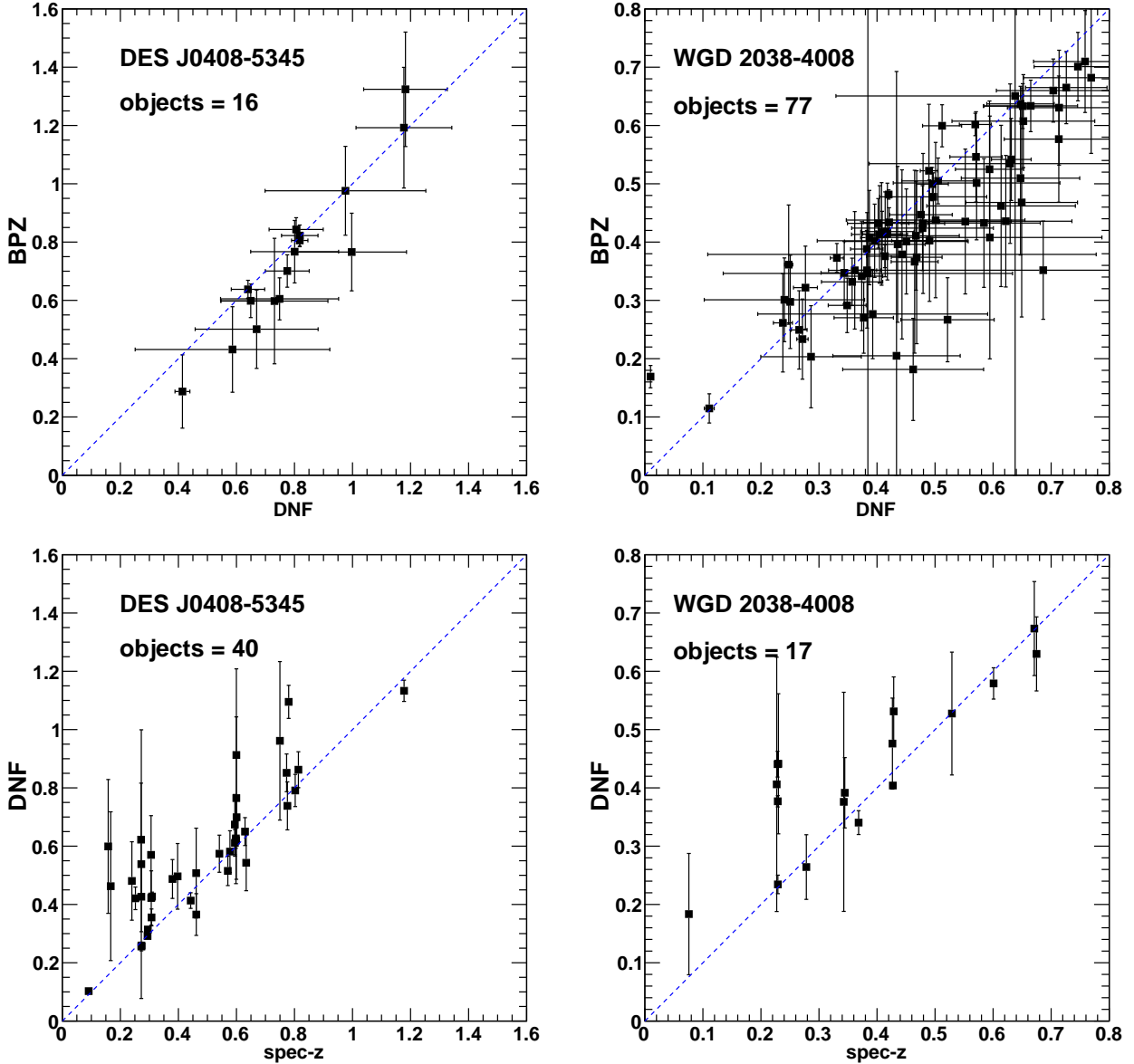


**Figure 1.** Upper figures: Comparison of the DNF and BPZ photometric redshifts for galaxies with no spectroscopic redshift which have  $i < 22.5$  within 120 arcsec of the lens center. The dashed line indicates  $\text{BPZ} = \text{DNF}$ . Left figure DES J0408–5354, right figure WGD 2038–4008. Lower figures: Comparison of spectroscopic and DNF photometric redshifts for galaxies with  $i < 22.5$  within 120 arcsec of the lens center. The dashed line indicates  $\text{spec-z} = \text{DNF photo-z}$ . Left figure DES J0408–5354, right figure WGD 2038–4008.

314 [Wagner et al. \(2018\)](#). We select all objects with  $i$ -band magnitude  
 315  $0 < \text{SOF\_CM\_MAG\_CORRECTED\_I} < 22.5$ . The faint-end limiting  
 316 magnitude, which is the same one used in [Rusu et al. \(2019\)](#) based  
 317 on the analysis in [Sluse et al. \(2019\)](#), also for the purpose of con-  
 318 straining  $H_0$ , ensures that the galaxy classification is reliable, and  
 319 that the galaxy catalog is complete. It is also deep enough ([Collett  
 320 et al. 2013](#)) to keep biases on  $\kappa_{\text{ext}}$  due to depth significantly be-  
 321 low the 1% level. We are using the photometric redshifts that were  
 322 calculated using the SOF magnitudes, namely  $\text{DNF\_ZMEAN\_SOF}$   
 323 or  $\text{BPZ\_ZMEAN\_SOF}$ . We also require that the redshift  $\text{DNF\_ZMEAN\_SOF}$   
 324 or  $\text{BPZ\_ZMEAN\_SOF}$  of the objects satisfy  $z < z_S$ , where  $z_S$  is the  
 325 source redshift, and that their distance  $\Delta r$  from the center of the field  
 326 is less than  $120''$ . Figure 3 shows the objects that pass these selection

327 criteria in a  $1000 \times 1000$  pixel field around DES J0408–5354 and  
 328 WGD 2038–4008.

### 3 REDSHIFTS AND STELLAR MASSES

329 In this section we first describe our spectroscopic redshift mea-  
 330 surement procedure, summarize the results, and show the line-of-  
 331 sight galaxy redshift distributions for each lensing system. We then  
 332 describe and plot the spectroscopic redshift completeness for the  
 333 overall galaxy samples in the two systems. Finally, we detail the  
 334 procedures for measuring stellar masses using photometric model  
 335 fitting for our galaxies.  
 336

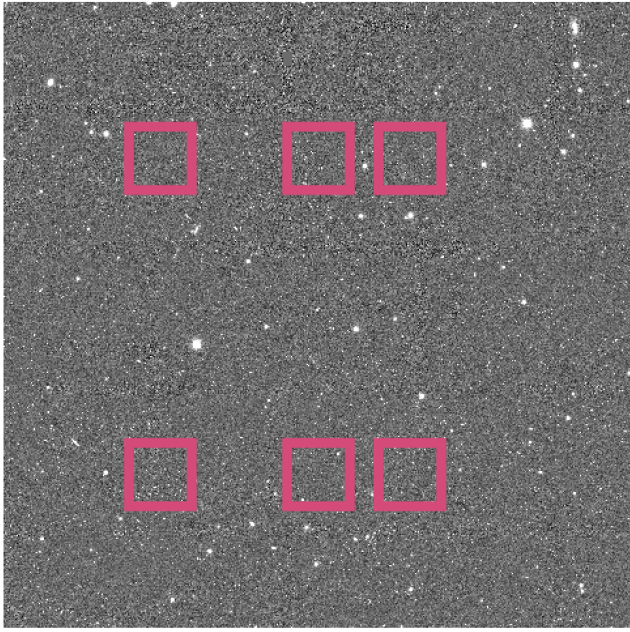


**Figure 2.** A typical DES tile showing the location of the control fields. Each magenta box is  $1000 \times 1000$  pixels.

### 3.1 Spectroscopic redshifts

337

338 The Gemini and Magellan data were processed to 2D and 1D spectra  
 339 using the IRAF Gemini and COSMOS (Dressler et al. 2011; Oem-  
 340 ler et al. 2017) reduction packages, respectively. Initial redshifts  
 341 were determined automatically (without visual inspection) using  
 342 the IRAF external package *rvsao* (Kurtz & Mink 1998) to cross  
 343 correlate the 1D spectra against a set of SDSS galaxy templates.  
 344 All processed 2D and 1D spectra, along with the corresponding  
 345 automated redshift results, were visually inspected in order to as-  
 346 sign final quality flags to the redshifts. If necessary, an automa-  
 347 ted redshift may be overridden and manually re-measured from the 2D  
 348 or 1D spectrum. Only high-confidence redshifts were included in  
 349 the subsequent analyses.

350 For DES J0408–5354, we obtained 101 high-confidence  
 351 galaxy redshifts from Gemini South GMOS-S and 70 from Mag-  
 352 ellan LDSS-3. From the VLT MUSE data we obtained another 28  
 353 redshifts that were not already among the Gemini and Magellan  
 354 redshifts, thus resulting in a total of 199 high-confidence redshifts  
 355 for DES J0408–5354. For WGD 2038–4008 we obtained a total of  
 356 54 high-confidence galaxy redshifts, all obtained from the Gemini  
 357 South GMOS-S data. The above counts include the two redshifts of  
 358 the main lensing galaxies in the systems. Figure 4 shows histograms  
 359 of the redshift distributions for each lensing system.

### 3.2 Redshift completeness

360

361 We define spectroscopic redshift completeness to be the fraction of  
 362 DES Y3 Gold (Sevilla et al. in prep) galaxies that have redshifts (as  
 363 described in §3.1). To define our photometric galaxy sample, we use  
 364 the latest and best available version of the Y3 Gold catalog, version  
 365 2.2, and we also use the same magnitude and star-galaxy separation  
 366 cuts as listed in target selection criteria (C) of §2.2 above.

367 For DES J0408–5354, the resulting spectroscopic redshift  
 368 completeness is 0.68 for  $18 \leq \text{MOF\_CM\_MAG\_CORRECTED\_I} < 23$

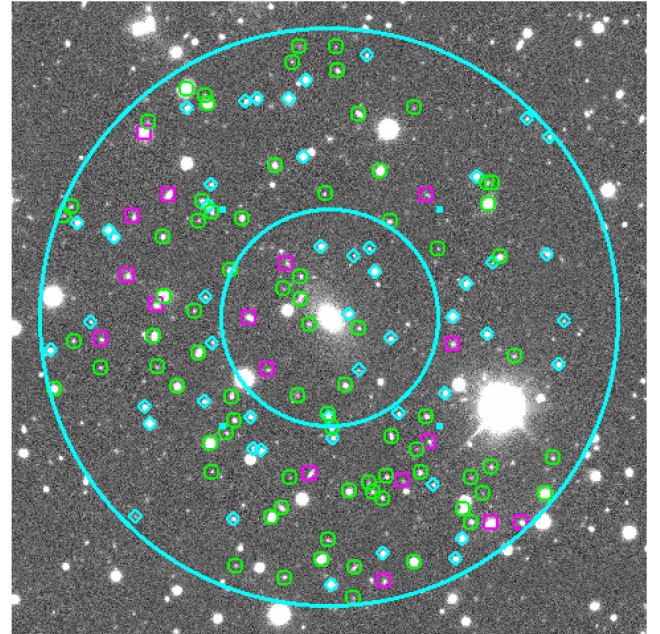
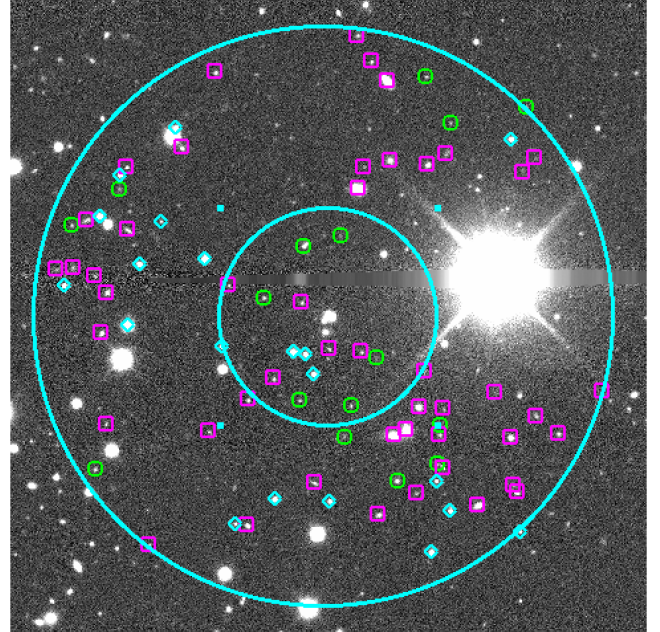


**Figure 3.** The  $1000 \times 1000$  pixel field of view for DES J0408–5354 (upper figure) and WGD 2038–4008 (lower figure). North is up and East is left. The  $i < 22.5$  galaxies inside the  $120''$  radius aperture are indicated by magenta squares for the objects with a spectroscopic redshift and green circles for the objects with no spectroscopic redshift. Stars are indicated by the cyan diamonds. The two concentric cyan circles indicate the apertures of  $120''$  and  $45''$  radius respectively.

369 galaxies and  $5'' \leq \text{radius} < 3'$ ; see the top panels of Figure 5. For  
 370 WGD 2038–4008, the redshift completeness is 0.16 for the same  
 371  $i$ -band magnitude and radius ranges, as shown in the bottom panels  
 372 of Figure 5. Within the plotted magnitude and radius ranges, the  
 373 redshift completeness stays fairly constant for both systems. The  
 374 inner radius cut of  $5''$  is intended to exclude the quasar images from

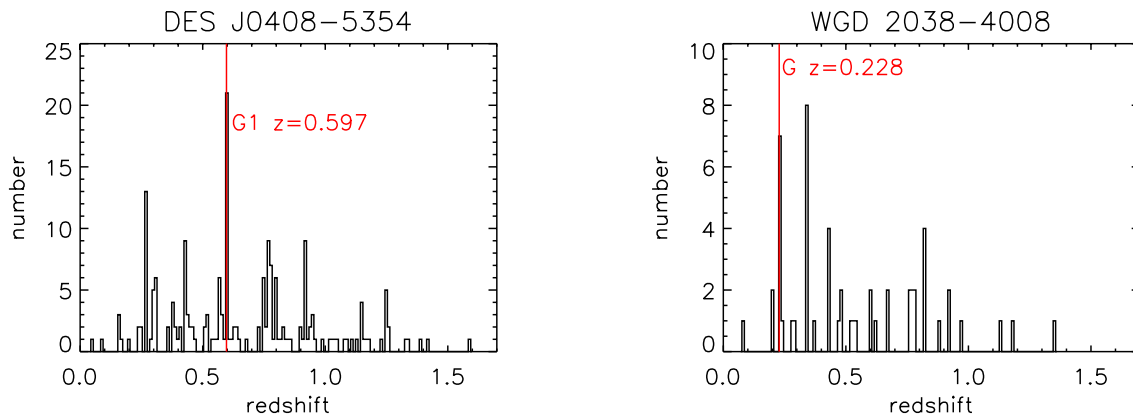


**Figure 4.** Histograms of line-of-sight galaxy spectroscopic redshifts (§3.1) for the (left) DES J0408–5354 and (right) WGD 2038–4008 systems. In each panel the red vertical line indicates the redshift of the main lensing galaxy in each system.

375 consideration. The outer radius cut is set at  $3'$  as the redshift com- 413  
 376 pleteness drops very rapidly beyond this radius for either system. 414

### 377 3.3 Stellar masses

378 Stellar masses necessary for the computation of the flexion shift, the 413  
 379 criterion used to separate between the structures which need to be 414  
 380 accounted for in the lensing model, and those which can be incorpo- 415  
 381 rated inside  $\kappa_{\text{ext}}$  (see §6.1) were computed using the galaxy template 416  
 382 fitting code Le PHARE (Arnouts et al. 1999; Ilbert et al. 2006). In 417  
 383 the Le PHARE fits, we either used our spectroscopic redshifts when 418  
 384 available, or DES Y3 Gold DNF photo- $z$ 's (DNF\_ZMEAN\_S0F), com-  
 385 bined with MOF photometry (Drlica-Wagner et al. 2018) from the  
 386 DES Y3 Gold (Sevilla et al. in prep) version 2.2 catalog. Specifi-  
 387 cally, we used the MOF\_CM\_MAG\_CORRECTED magnitudes and their  
 388 associated errors in the  $griz$  filters, as these magnitudes included  
 389 Milky Way extinction and other small photometric corrections (see  
 390 2.2).

391 The galaxy template set used in the Le PHARE fits were taken 427  
 392 from the BC03 (Bruzual & Charlot 2003) spectral energy distribu- 428  
 393 tion (SED) library. Specifically, we used a set of 27 BC03 simple 429  
 394 stellar population models, computed using the Padova 1994 stellar 430  
 395 evolution library (described in Bruzual & Charlot 2003) and the 431  
 396 Chabrier (2003) initial mass function. The 27 models consisted of 432  
 397 9 exponentially declining star formation rate (SFR) histories (with 433  
 398 decay times  $\tau = 0.1, 0.3, 1, 2, 3, 5, 10, 15, 30$  Gyr), each computed 434  
 399 at 3 different metallicity values (0.4, 1, and 2.5 times solar). Each of 435  
 400 the 27 models was also computed at different ages (ranging from 0.2 436  
 401 to 13.5 Gyr) and redshifts (up to a maximum redshift of 1.1, in steps 437  
 402 of 0.03 in redshift). No dust extinction was included in the models, 438  
 403 but recall the DES magnitudes already included correction for fore- 439  
 404 ground Milky Way extinction. The stellar masses and uncertainties 440  
 405 computed from the Le PHARE fits are tabulated in Table A1.

406 For a few of the close neighbor galaxies of the two lensed quasar 441  
 407 systems, the original object deblending and resulting photometry in 442  
 408 the DES Y3 catalog were clearly incorrect upon visual inspection of 443  
 409 the images. In particular, for DES J0408–5354, the neighbor galaxy 444  
 410 with ID number 488066768 (or name G5, in Table 4 or Table A1) had 445  
 411 magnitudes that were too bright, and for WGD 2038–4008, the three 446  
 412 neighbor galaxies with ID numbers 13, 14, and 15 (Table A1) were 447

originally merged into a single object. To correct these photometry 413  
 414 problems, we used the galaxy image fitting code GALFIT (Peng 415  
 416 et al. 2010) to redo the galaxy model fitting and photometry for 417  
 418 these objects, based on the DES Y3 coadd images in the  $griz$  filters. 418  
 These GALFIT results were used to compute stellar masses via Le  
 PHARE.

## 4 VELOCITY DISPERSIONS OF LENSING GALAXIES

420 The main lensing galaxies in both the DES J0408–5354 and 421  
 422 WGD 2038–4008 systems were specifically targeted for stellar ve- 423  
 424 locity dispersion measurements on a number of the spectroscopic 424  
 425 masks listed above in Table 1. For these observations we describe 425  
 426 below the details of the targeting on the spectroscopic slits, the pro-  
 cedures used to extract the lensing galaxy spectra, and the method  
 employed to measure velocity dispersions.

### 4.1 DES J0408–5354 G1

428 The main lensing galaxy G1 in DES J0408–5354 was measured 429  
 430 from four independently observed spectra: two from Magellan 431  
 432 LDSS-3, one from Gemini South GMOS-S, and one from VLT 433  
 434 MUSE.

435 G1 was targeted on two of the four Magellan LDSS-3 masks 436  
 437 listed in Table 1, “des0408a” and “des0408b”; hereafter these two 437  
 438 masks will be denoted “Magellan a” and “Magellan b”. The slit setup 438  
 439 for G1 was the same on both masks, while the remaining targets were 439  
 440 different on the two masks. Specifically, the slit was oriented so that 440  
 441 it included both G1 and quasar image B (the naming convention for 441  
 442 the lensing galaxy G1 and the lensed quasar images A, B, and D 442  
 443 are shown in Lin et al. 2017). In addition, some contaminating flux 443  
 444 from quasar image A was also visible in the 2D spectrum from the 444  
 445 slit. To extract the 1D spectrum of G1, we first fit the spatial profiles 445  
 446 along the slit (at each wavelength) of G1, B, and A by two Moffat 446  
 447 profiles and a Gaussian profile, respectively. Moffat profiles were 447  
 adopted for G1 and B because Gaussian profiles gave worse fits  
 as determined by visual inspection. We subtracted off the best-fit  
 spatial profiles for B and A and summed the remaining flux over an  
 extraction window along the slit of  $1''$  (approximately the FWHM

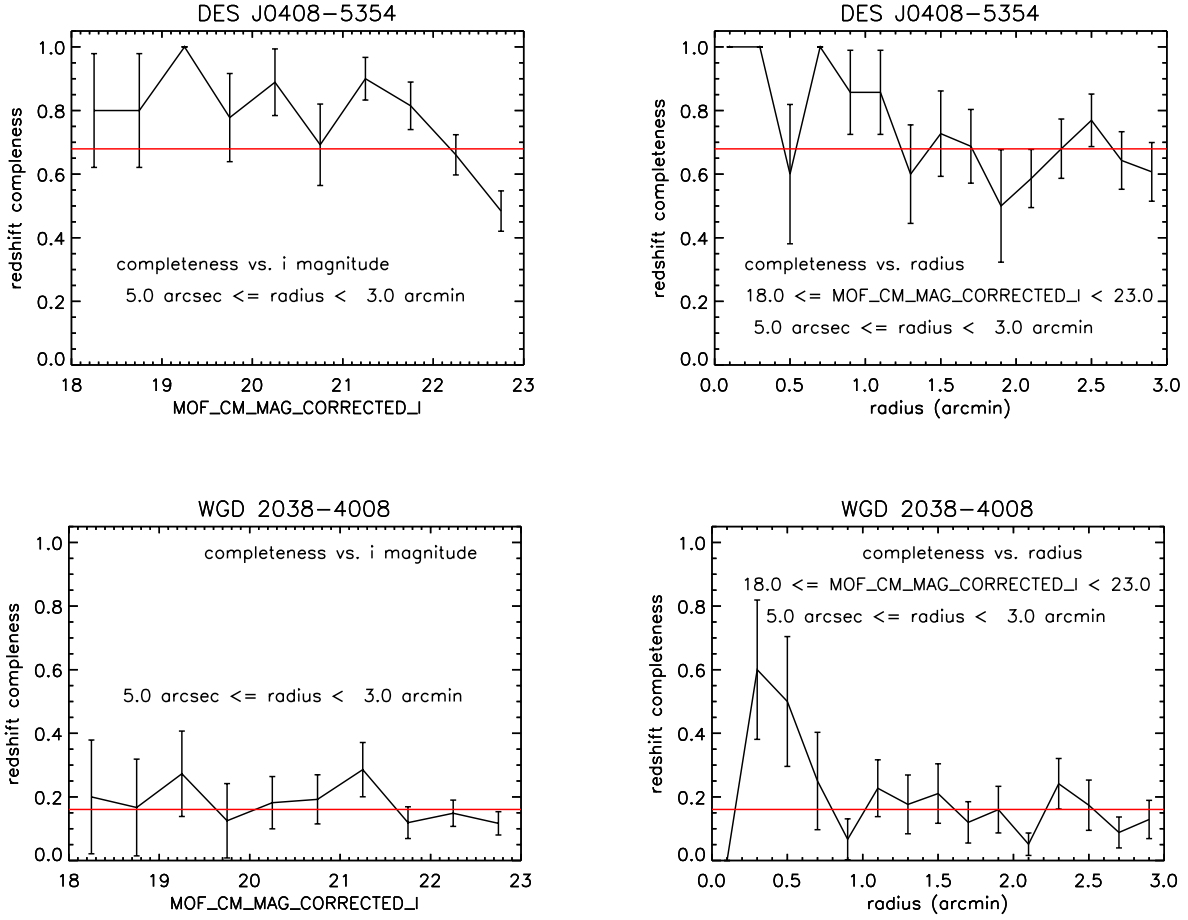


**Figure 5.** Spectroscopic redshift completeness (defined in §3.2) for DES J0408–5354 (top panels) and WGD 2038–4008 (bottom panels). The left panels show redshift completeness vs.  $i$ -band magnitude, within the radius range  $5''$  to  $3'$  from the lens galaxy in each system. The right panels show redshift completeness vs. radius, within the  $i$ -band magnitude range 18 to 23. In all panels the red horizontal line indicates the overall redshift completeness within the indicated magnitude and radius ranges for each system.

of G1’s Moffat profile) or  $2''$  (about the extent of G1’s profile) in order to extract G1’s 1D spectrum.

G1 was targeted on one of the Gemini South GMOS-S masks in Table 1, “DESJ0408-5354\_A2” (R400 grating), hereafter denoted “Gemini A2,” on a slit which also included quasar image D. The procedure to extract G1’s 1D spectrum was entirely analogous to that described above for the Magellan data. To fit the spatial profiles of G1 and D, Moffat profiles were again found to be better than Gaussians.

In the VLT MUSE data cube, the quasar and source light components were first modeled and removed, and the region near C and G2 was masked out. The remaining light from G1 was then extracted to a 1D spectrum by summing the light over a  $1'' \times 1''$  box or a  $2.2'' \times 2.2''$  box.

The velocity dispersion of G1 was then measured from the above data using the ULYSS (Koleva et al. 2009) galaxy spectral modeling package. In the rest wavelength range  $4800\text{\AA}$  to  $5500\text{\AA}$ , including the  $H\beta$ , Mg, and CaFe features, the G1 spectra were fit to Vazdekis et al. (2010) stellar population models, which used the MILES stellar library (Sánchez-Blázquez et al. 2006) and the Salpeter (1955) initial mass function. The wavelength dependent line spread function (LSF) in the Magellan and Gemini-South data

were determined from the widths of the arc lamp lines in the respective wavelength calibration spectra, while the LSF of the MUSE data were taken from the fits given in §3.1 of Guérou et al. (2017). Because the Gemini-South and in particular Magellan LSFs were noticeably non-Gaussian, we modified the ULYSS package so that it could make use of an empirical LSF, instead of an analytic Gaussian (or low-order Gauss-Hermite) LSF. The resulting velocity dispersion measurements and associated statistical errors are given in Table 2, showing good agreement among the results from the four independent data sets. Plots of the 1D spectra and best-fit models for the  $1''$  extraction window cases are shown in Figure 6.

#### 4.2 WGD 2038–4008 G

The main lensing galaxy G in WGD 2038–4008 was measured from one spectrum observed using Gemini South GMOS-S, specifically on mask (14) listed in Table 1: “DESJ2038-4008\_A” (B600 grating), hereafter denoted “Gemini A” for simplicity. One slit on this mask targeted galaxy G together with the quasar images C and D (the naming convention for the lensing galaxy and the lensed quasar images are shown in Figure 1 of Agnello et al. 2018). To extract the 1D spectrum of G, we used the same method described above



**Table 2.** Velocity dispersion results for the main lensing galaxies in the DES J0408–5354 and WGD 2038–4008 systems. Details of the measurements are given in §4.

Data set	Velocity dispersion (km/s)	Slit width (arcsec)	Extraction window (arcsec)	Seeing FWHM (arcsec)	Moffat index $\beta$
DES J0408–5354					
Magellan a	230 ± 37	1.0	1.0	0.68	2.97
Magellan b	236 ± 42	1.0	1.0	0.76	3.20
Gemini A2	220 ± 21	0.75	1.0	0.52	3.06
MUSE	227 ± 9	1.0	1.0	0.61	1.55
Magellan a	209 ± 37	1.0	2.0	0.68	2.97
Magellan b	230 ± 47	1.0	2.0	0.76	3.20
Gemini A2	261 ± 21	0.75	2.0	0.52	3.06
MUSE	227 ± 9	2.2	2.2	0.61	1.55
WGD 2038–4008					
Gemini A	296 ± 19	0.75	1.0	0.90	1.74
Gemini A	303 ± 24	0.75	2.0	0.90	1.74

in §4.1. Specifically, we fit the spatial profiles of G, C, and D with three Moffat profiles, subtracted off the best-fit profiles of C and D, and then summed the remaining flux over extraction windows of 1'' or 2'' along the length of the slit. The velocity dispersion of G was then measured with ULySS, using the same rest wavelength range and the same stellar population models as above in §4.1. The resulting velocity dispersion measurements and statistical errors are given in Table 2. The 1D spectrum and best-fit model for the 1'' extraction window case are shown in Figure 6.

## 5 GALAXY GROUP IDENTIFICATION

### 5.1 Galaxy Group Identification Algorithm

For galaxy-group identification, we employed the same algorithm used in the spectroscopic analysis of the fields of HOLiCOW lenses HE 0435–1223 (Sluse et al. 2017) and WFI 2033–4723 (Sluse et al. 2019), which is based on the group-finding algorithms of Wilman et al. (2005) and Ammons et al. (2014). Wilson et al. (2016) uses a similar method, the results of which were used in the analysis of the HOLiCOW lens PG 1115+080 (Chen et al. 2019). We summarize the method here, and refer interested readers to Sluse et al. (2017) for a more complete description and explanation of parameter choices in this algorithm.

The first step towards identifying galaxy groups involves searching for candidate groups in the spectroscopic redshift distribution of the surveyed galaxy catalog. We begin by constructing a redshift histogram with bins of width 2000 km s<sup>-1</sup>. We identify redshift bins with 5 or more members as candidate groups. To ensure that candidate group members are not split across two bins due to an arbitrary choice of bin boundaries, we construct a second redshift histogram with the bins shifted by half a width of a bin (1000 km s<sup>-1</sup>), and count all non-duplicate redshift peaks from both histograms as candidate groups. We include all other galaxies that are within 1500 km s<sup>-1</sup> of a candidate group member in that candidate group.

Once we have identified the candidate groups, we use a bi-weight location estimator (Beers et al. 1990) to calculate the mean (group) redshift of each candidate group. The group centroid is also calculated from the positions of the candidate group members. Since Sluse et al. (2019) found that using a luminosity-weighted scheme to calculate the centroid does not improve the match between the

group centroid and brightest galaxy in this method, we do not use luminosity-weighted centroids here.

Once candidate groups have been identified, they are subjected to an algorithm that iteratively removes outliers in both redshift and angular space until the algorithm converges to a stable solution or a group membership of zero. The latter indicates that the candidate group is not gravitationally linked and is spurious. The algorithm is as follows:

(i) We set the initial observer-frame velocity dispersion,  $\sigma_{\text{obs}}$  to 500 km s<sup>-1</sup>. This value will be revised in subsequent iterations.

(ii) Candidate group members that are further than twice the velocity dispersion away from the group redshift are excluded from the group. This corresponds to the following limit

$$\delta z_{\text{max}} = n \times \sigma_{\text{obs}} / c \quad (1)$$

where  $n = 2$ . This redshift limit is converted into an angular separation limit

$$\delta \theta_{\text{max}} = \frac{c \times \delta z_{\text{max}}}{b(1+z)H(z)D_{\theta}(z)} \quad (2)$$

where  $H(z)$  is the Hubble parameter at redshift  $z$  and  $D_{\theta}(z)$  is the angular diameter distance from the observer to redshift  $z$ . Following Sluse et al. (2017), we set the aspect ratio  $b = 3.5$ . Candidate group members that have an angular separation that is larger than  $\delta \theta_{\text{max}}$  from the group centroid are excluded from the group.

(iii) Once cuts have been made in both redshift and angular separation, we recalculate the group centroid, group redshift and observed-frame velocity dispersion  $\sigma_{\text{obs}}$  from the remaining candidate group members. We obtain the latter two quantities following this framework:

- If there are more than 10 galaxies remaining, we use the biweight location and scale estimators to calculate the group redshift and velocity dispersion, respectively (Mosteller & Tukey 1977).
- If there are between 4 and 10 galaxies remaining (inclusive), we use the biweight location to calculate the group redshift and the gapper estimator to calculate the velocity dispersion (Wainer & Thissen 1976; Beers et al. 1990).
- If there are fewer than 4 galaxies, we use the mean redshift as the group redshift and the standard deviation as the velocity dispersion.

Steps (ii) and (iii) are repeated until we reach a stable solution. Galaxies that are members of these identified groups are then used to infer group properties, such as the group redshift, centroid, velocity dispersion, and flexion shift (following the method described in §6.1. The rest-frame velocity dispersions are calculated from the observer-frame velocity dispersions using

$$\sigma_{\text{rest}} = \frac{\sigma_{\text{obs}}}{1 + \bar{z}_{\text{group}}} \quad (3)$$

We then estimate uncertainties in the group properties by bootstrapping (i.e. random sampling with replacement) the group members of each group 1000 times. We recalculate the group properties of the resampled groups, and use the bootstrapped distribution in those quantities to estimate their uncertainties.

Because the associated measurement uncertainties of the galaxies in the spectroscopic redshift catalog ( $\Delta v_{\text{err}} \sim 100$  km s<sup>-1</sup>, see §3) are of order the measured velocity dispersion of many of the identified groups, care must be given to account for these uncertainties. To this end, we forward-model the kinematic datasets to infer

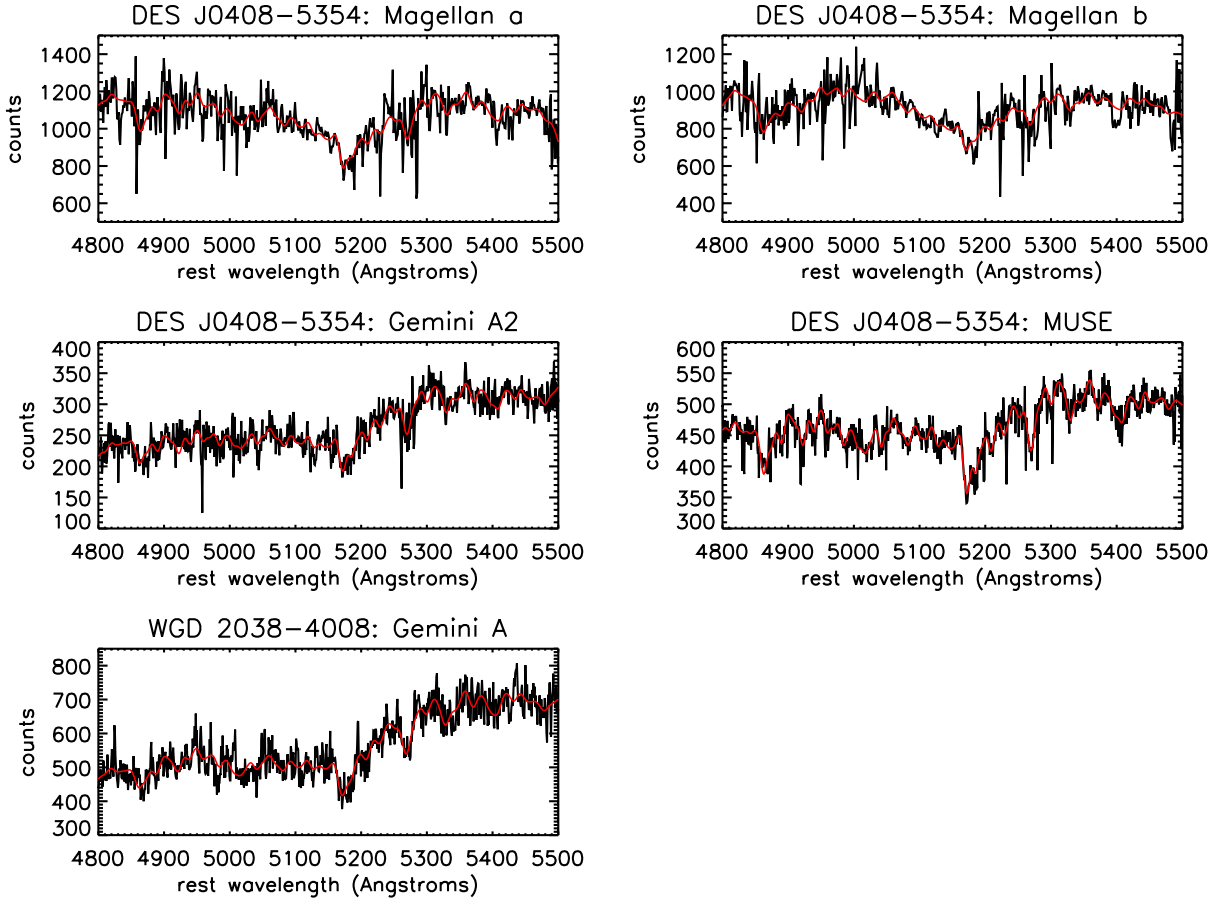


**Figure 6.** The 1D spectra and fits involved in the velocity dispersion measurements of the main lensing galaxies G1 in the DES J0408–5354 system (top and middle panels) and G in the WGD 2038–4008 system (bottom panel), as described in §4 and listed in Table 2. The black curves in the plots show the observed data, in units of counts vs. rest-frame wavelengths in Angstroms, while the red curves show the best-fit models (details in §4). All the data and fits shown are for the case of a 1'' extraction window (see §4 and Table 2).

576 the velocity dispersion given measurement uncertainties, following  
 577 techniques used in dwarf-galaxy studies (e.g. Kposov et al. (2011);  
 578 Walker & Peñarrubia (2011); Amorisco & Evans (2012)), where it  
 579 has been found to be especially relevant for systems with small  
 580 numbers of discrete kinematic tracers (Martin et al. 2018; Laporte  
 581 et al. 2019). We construct a generative likelihood model for the data  
 582 and evaluate the posterior probability distribution for the intrinsic  
 583 velocity dispersion,  $\sigma_{\text{int}}$ . The likelihood function is

$$\mathcal{L} = \prod_i \frac{1}{\sqrt{2\pi}\sigma_{\text{obs}}} \exp\left(-0.5 \left(\frac{v_i - \langle v \rangle}{\sigma_{\text{obs}}}\right)^2\right) \quad (4)$$

584 where  $\langle v \rangle$  is the mean velocity, the product is over all member  
 585 galaxies  $i$  of the galaxy group, and  $\sigma_{\text{obs}}^2 = \sigma_{\text{int}}^2 + \Delta v_{\text{err}}^2$ . We assume  
 586  $\Delta v_{\text{err}} = 100 \text{ km s}^{-1}$ , and a non-informative Jeffreys prior for the  
 587 intrinsic velocity dispersion  $\sigma_{\text{int}}$  (i.e.  $p(\sigma_{\text{int}}) \propto 1/\sigma_{\text{int}}$ ) over the  
 588 range 1 to 1000  $\text{km s}^{-1}$ . We also assume a uniform prior for the  
 589 mean group velocity  $\langle v \rangle$  over the range -500 to 500  $\text{km s}^{-1}$  and  
 590 treat it as a nuisance parameter. We then sample the posterior PDF

591 using the emcee affine invariant Markov Chain Monte Carlo sampler  
 592 (Foreman-Mackey et al. 2013; Goodman & Weare 2010). We then  
 593 report the median and 68th percentile confidence intervals of the  
 594 posterior PDF for  $\sigma_{\text{int}}$  in Table 3. For groups where the posterior  
 595 PDF for  $\sigma_{\text{int}}$  peaks near zero and the lower bounds are not well-  
 596 constrained, we report only the 68th percentile upper limits.

## 5.2 Identified Groups in the Environment of DES J0408–5354

599 We applied the galaxy-group identification algorithm to the com-  
 600 bined catalog of 199 galaxies with high-confidence redshifts in the  
 601 field of DES J0408–5354 described in §3. We identified 10 galaxy  
 602 groups comprising of 76 galaxies from this spectroscopic sample,  
 603 which we label Group 1-10 in order of increasing group redshift.  
 604 Their properties are summarized in Table 3, and Figure 7 shows,  
 605 for each identified galaxy group, the positions of both accepted and  
 606 rejected trial member galaxies of that group in right ascension and

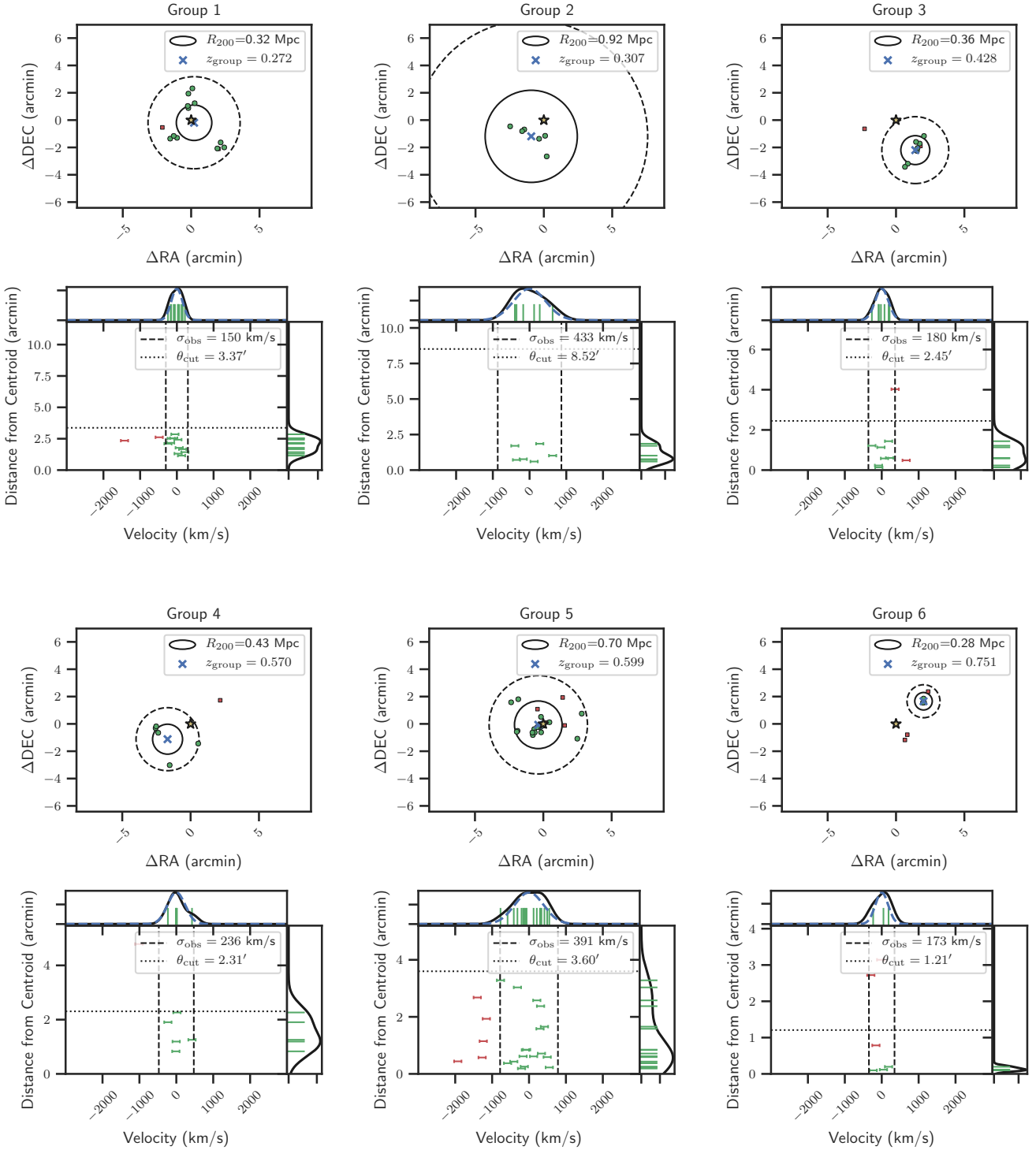


**Figure 7.** Galaxy groups identified in the spectroscopic sample of galaxies in the field of view of DES J0408–5354. For each group, the first plot (above) shows the positions of the candidate member galaxies associated with that group relative to the lens galaxy, with rejected group members represented as red squares and accepted group members represented as green circles. The lens galaxy DES J0408–5354 (star) and group centroid (cross) are also displayed. The  $R_{200}$  radius of the group is represented by a solid line, while the dashed circle represents the angular separation cut of the group-finding algorithm in its final iteration. The second plot (below) shows the observer-frame velocity of individual member galaxies relative to the group centroid as a function of that galaxy's angular distance from the centroid. Galaxies that passed the iterative algorithm described in §5.1 are shown in green, while trial galaxy members that were cut through the algorithm are shown in red. Horizontal error bars represent the measurement error for each galaxy (see §3). The final observer-frame velocity dispersion and angular separation cuts from the group-finding algorithm are presented as dashed and dotted lines respectively. We also show 1-D histograms and rug plots of the velocity and distance distributions of the member galaxies. The 1-D histograms are produced using a Kernel Density Estimate (KDE) with a bandwidth determined using Scott's Rule. In the 1D velocity histogram, the dashed blue line shows a gaussian with width equal to the observer-frame velocity dispersion of the group.

**Table 3.** Group properties in the field of view of DES J0408–5354 and WGD 2038–4008. The columns show the group ID, group redshift, number of spectroscopically identified galaxies in that group, the group rest-frame velocity dispersion (rounded to the nearest 10 km s<sup>-1</sup>), the group centroid (in RA and Dec), projected distance of the centroid to the lens ( $\Delta\theta$ ), and median flexion shift  $\log(\Delta_3x)$  (arcsec) (see §6.1 for methodology). All reported values are median quantities of 1000 bootstrapped samples, with uncertainties given by the 16th and 84th confidence intervals of the distribution of the bootstrapped quantity. Velocity dispersion estimates are rounded to nearest 10 km s<sup>-1</sup>. See §6.1.2 for further discussion.

ID	$\bar{z}_{\text{group}}$	N	$\sigma_{\text{rest}}$ (km s <sup>-1</sup> )	$\sigma_{\text{int}}$ (km s <sup>-1</sup> )	$R_{200}$ (Mpc)	RA <sub>ctr</sub> , DEC <sub>ctr</sub> (deg)	error(RA <sub>ctr</sub> , DEC <sub>ctr</sub> ) (arcmin)	$\Delta\theta$ (arcsec)	$\log_{10}(\Delta_3x)$ (log <sub>10</sub> (arcsec))
DES J0408–5354									
1	0.272	11	110 ± 20	< 70	0.30 <sup>+0.05</sup> <sub>-0.06</sub>	62.096099, -53.903136	0.67, 0.46	32 <sup>+22</sup> <sub>-16</sub>	< -5.88
2	0.307	6	290 <sup>+60</sup> <sub>-90</sub>	300 <sup>+160</sup> <sub>-80</sub>	0.81 <sup>+0.15</sup> <sub>-0.24</sub>	62.065082, -53.919339	0.71, 0.31	94 <sup>+10</sup> <sub>-10</sub>	-4.79 <sup>+0.74</sup> <sub>-0.63</sub>
3	0.428	7	110 ± 30	< 70	0.31 <sup>+0.07</sup> <sub>-0.09</sub>	62.130389, -53.936509	0.29, 0.29	156 <sup>+10</sup> <sub>-8</sub>	< -8.04
4	0.570	5	140 <sup>+30</sup> <sub>-90</sub>	< 160	0.41 <sup>+0.09</sup> <sub>-0.25</sub>	62.042510, -53.918109	1.00, 0.52	122 <sup>+28</sup> <sub>-21</sub>	< -6.53
5 ★	0.599	17	240 <sup>+30</sup> <sub>-40</sub>	220 <sup>+60</sup> <sub>-50</sub>	0.68 <sup>+0.08</sup> <sub>-0.11</sub>	62.079749, -53.901149	0.54, 0.18	26 <sup>+16</sup> <sub>-12</sub>	-3.86 <sup>+0.97</sup> <sub>-0.72</sub>
6	0.751	3	80 ± 40	< 100	0.21 <sup>+0.11</sup> <sub>-0.11</sub>	62.147320, -53.872270	0.05, 0.09	156 <sup>+3</sup> <sub>-2</sub>	< -8.06
7	0.768	5	120 <sup>+30</sup> <sub>-50</sub>	< 120	0.34 <sup>+0.10</sup> <sub>-0.15</sub>	62.084144, -53.898689	0.28, 0.24	17 <sup>+12</sup> <sub>-7</sub>	< -4.83
8	0.799	6	340 <sup>+60</sup> <sub>-80</sub>	370 <sup>+170</sup> <sub>-100</sub>	0.96 <sup>+0.18</sup> <sub>-0.22</sub>	62.143634, -53.894864	0.64, 0.71	120 <sup>+22</sup> <sub>-22</sub>	-5.46 <sup>+0.72</sup> <sub>-0.59</sub>
9	0.918	9	300 <sup>+40</sup> <sub>-50</sub>	310 <sup>+120</sup> <sub>-70</sub>	0.86 <sup>+0.10</sup> <sub>-0.15</sub>	62.051793, -53.892228	0.49, 0.45	90 <sup>+16</sup> <sub>-17</sub>	-5.70 <sup>+0.58</sup> <sub>-0.52</sub>
10	1.252	7	240 <sup>+30</sup> <sub>-50</sub>	240 <sup>+110</sup> <sub>-70</sub>	0.67 <sup>+0.09</sup> <sub>-0.15</sub>	62.124690, -53.913336	0.69, 0.12	87 <sup>+22</sup> <sub>-21</sub>	-6.92 <sup>+0.80</sup> <sub>-0.71</sub>
WGD 2038–4008									
1 ★	0.229	7	200 <sup>+70</sup> <sub>-60</sub>	200 <sup>+90</sup> <sub>-70</sub>	0.53 <sup>+0.18</sup> <sub>-0.16</sub>	309.528309, -40.126006	0.41, 0.28	62 <sup>+23</sup> <sub>-24</sub>	-5.30 <sup>+0.90</sup> <sub>-0.83</sub>
2	0.342	8	380 <sup>+70</sup> <sub>-90</sub>	400 <sup>+150</sup> <sub>-100</sub>	1.05 <sup>+0.19</sup> <sub>-0.26</sub>	309.543495, -40.142963	0.54, 0.28	91 <sup>+26</sup> <sub>-27</sub>	-5.39 <sup>+0.73</sup> <sub>-0.59</sub>

**Note:** ★ Group contains the lens galaxy.

declination, as well as the distances and velocities relative to the converged group centroid.

The largest galaxy group identified in this spectroscopic sample is Group 5, which contains 17 member galaxies, including the lens galaxy of DES J0408–5354. The centroid of this group is close to DES J0408–5354 (26<sup>+16</sup><sub>-12</sub> arcsec), which is also the most luminous member galaxy in the group.

Aside from group 5, the identified groups are generally small, with no identified group containing more than 11 member galaxies. For Groups 1, 3, 4, 6 and 7, the posterior PDFs for the intrinsic velocity dispersions peak at or near zero, and the lower limits are not well-constrained. For these distributions, we report the upper 68th percentile confidence intervals for these distributions and treat it as the upper limit of the intrinsic velocity dispersion for that group.

For groups 8 and 9, the distribution of member galaxies in velocity space appears to be bimodal, with two separate subgroups separated by ~ 1000 km s<sup>-1</sup>. However, there are not enough member galaxies in that redshift range to successfully separate these two subgroups into separate groups as none of the individual subgroups have more than 5 potential members.

The choice of parameters used in the group-finding algorithm described in §5.1 can impact the final membership of each galaxy group. As mentioned in §5.1, the choice of fiducial values for the initial observer-frame velocity dispersion  $\sigma_{\text{obs}} = 500$  km s<sup>-1</sup>, velocity threshold  $n = 2$  (Eq. 1), aspect ratio  $b = 3.5$  (Eq. 2) follow that of previous group-finding analyses (Sluse et al. 2017; Sluse et al. 2019; Wilman et al. 2005). We relaxed the parameter  $n$  to  $n = 3$  to investigate the effect of a more conservative (i.e. more inclusive) choice in the group finding algorithm and found that relaxing the parameters results in groups that contain outlier members, or have bi- or multimodal configurations, all of which are likely to be spurious.

As an additional sanity check, we inspected the Chandra X-ray images of the field (PI: Pooley; Program 20419; ACIS-S; 25ks). No

diffuse emission is detected (Pooley, D & Gallo, E. 2019, private communication), with an upper limit (90% CL) of ~ 10<sup>44</sup> erg/s within a 1Mpc radius (with considerable error bars depending on the assumed temperature). The non-detection makes it unlikely that the lens galaxy is a member of a galaxy cluster.

### 5.3 Identified Groups in the Environment of WGD 2038–4008

We applied the group-finder to the 54 galaxies with high confidence redshifts in the field of WGD 2038–4008. From this sample, we identified 2 galaxy groups. The results and properties of these galaxy groups are summarized in Table 3, and Figure 8 show, for each identified galaxy group, the positions of both accepted and rejected member galaxies of that group, as well as the distances and velocities of individual galaxies relative to the group centroid. Group 1 in WGD 2038–4008’s field contain the eponymous lens galaxy of that field.

## 6 CONTRIBUTION OF ENVIRONMENT GALAXIES AND GALAXY-GROUPS TO THE LENS STRUCTURE

### 6.1 Flexion Shift Formalism

A major objective of this analysis is to identify galaxies or galaxy groups along the line of sight or in the environment of lensing systems that significantly perturb the lensing potential of that system and require explicit modeling in the cosmological analysis. Perturbations that are weak can be treated as a tidal perturbation, producing external convergence and external shear at the position of the lens galaxy. However, perturbers that produce non-negligible third order (i.e. flexion) and higher perturbations to the lens potential cannot be well-approximated by the tidal approximation and will need to

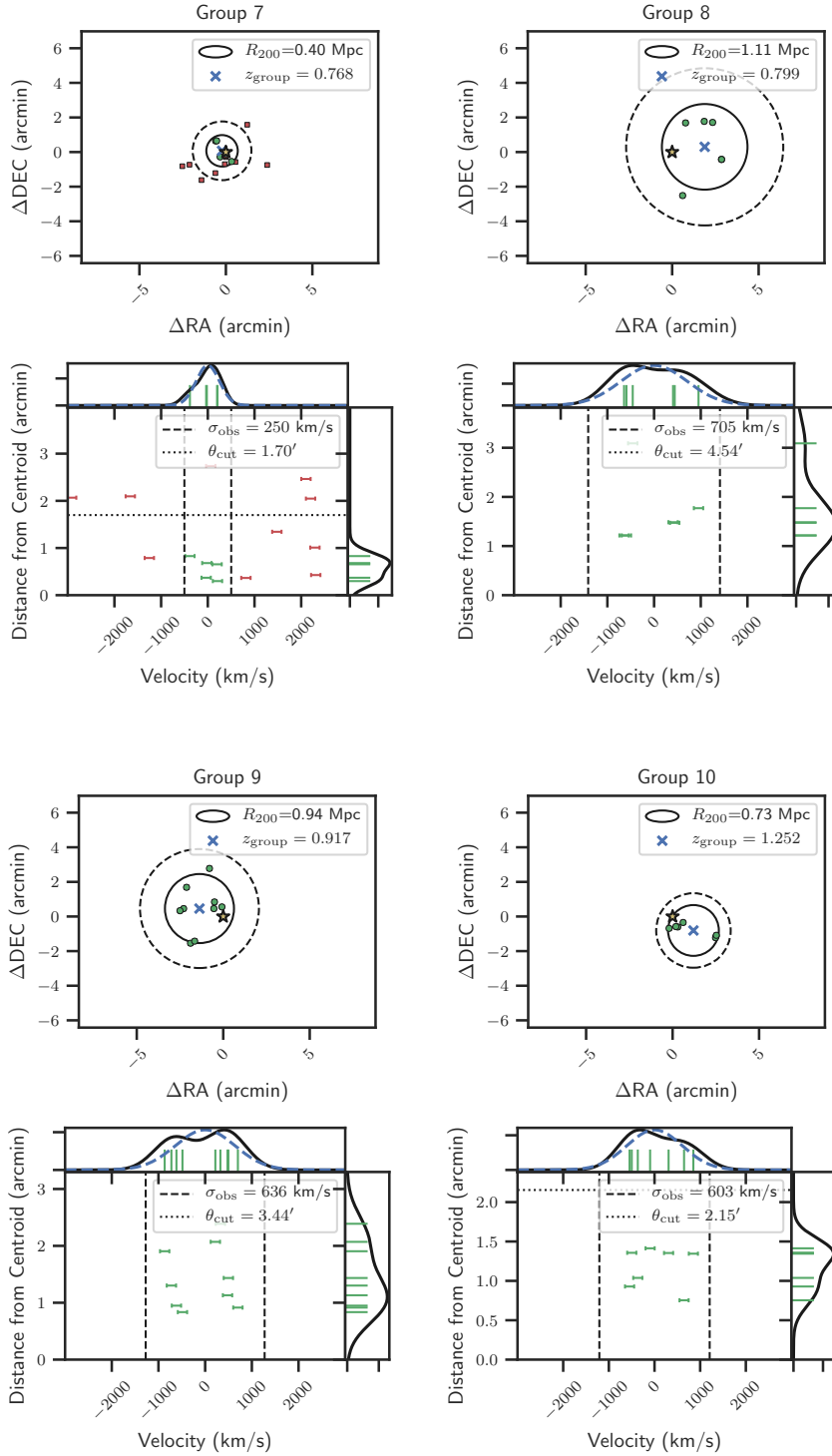
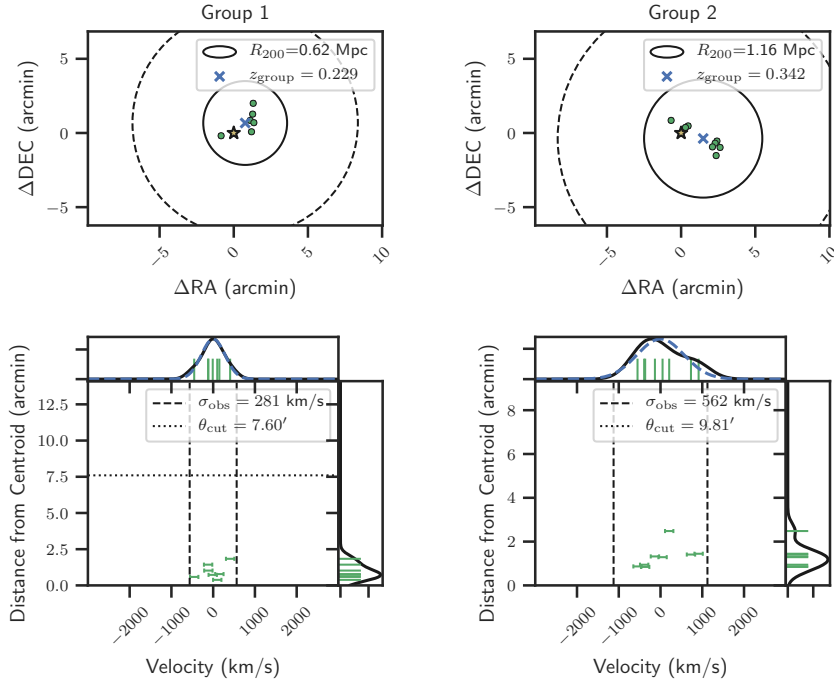


Figure 7. (continued)

669 be explicitly treated in the lens model. Since the largest terms in the  
 670 lens potential that are neglected in the tidal approximation are the  
 671 third order flexion terms, McCully et al. (2017) proposes a simple  
 672 diagnostic, the “flexion shift”, which is a measurement of the differ-  
 673 ence in lensed image positions caused by the inclusion of the flexion  
 674 terms from a perturber. As long as the flexion shift of a perturbing

675 galaxy or galaxy group is much smaller than the astrometric preci-  
 676 sion of the observed lensed images, the perturber does not need to  
 677 be explicitly treated in the lens model in a cosmographical analysis.



**Figure 8.** Galaxy groups identified using the spectroscopic sample of galaxies in the environment of WGD 2038–4008. See Figure 7 for an explanation of the figures.

678 Following McCully et al. (2017), the flexion shift is given by

$$\Delta_{3x} = f(\beta) \times \frac{(\theta_E \theta_{E,p})^2}{\theta^3}, \quad (5)$$

679 where  $\theta_E$  and  $\theta_{E,p}$  are the Einstein radii of the main lens and  
680 perturber respectively, and  $\theta$  is the angular separation on the sky  
681 between them. The function  $f(\beta)$  is

$$f(\beta) \in \left\{ \begin{array}{ll} (1 - \beta)^2 & \text{if perturber is behind the lens} \\ 1 & \text{if perturber is in the foreground} \end{array} \right\}, \quad (6)$$

where

$$\beta = \frac{D_{dp} D_{os}}{D_{op} D_{ds}}, \quad (7)$$

682 is a combination of angular diameter distances involving the obser-  
683 ver (o), deflector (d), perturber (p), and source (s), where the  
684 subscripts  $D_{ij} = D(z_i, z_j)$  indicate the angular diameter distance  
685 between redshifts  $z_1$  and  $z_2$ .

686 This diagnostic provides a simple quantity to estimate the  
687 difference in lensed image positions caused by the leading order  
688 non-tidal (i.e. third-order) perturbation produced from a per-  
689 turber. McCully et al. (2017) showed that by explicitly modeling  
690 perturbers with flexion shifts larger than the conservative limit of  
691  $\Delta_{3x} > 10^{-4}''$ , we can constrain the bias on  $H_0$  due to this un-  
692 certainty to the percent level. We explain how the Einstein radii,  
693  $\theta_{E,p}$ , as well as the flexion shift uncertainties for each perturber, are  
694 determined for galaxies in §6.1.1, and for galaxy groups in §6.1.2.

695 We calculated the flexion shift for all galaxies in the spec-  
696 troscopic survey, as well as the flexion shift of all galaxy groups  
697 identified from the survey (§6.1.2). For individual galaxies, we

698 exclude 4 objects that are in DES Y1 Gold catalog but not in  
699 the DES Y3 Gold catalog. We also exclude 12 galaxies with  
700 spectroscopic redshifts from MUSE because they do not have  
701 DES Y3 photometry. In addition, one galaxy in the spec-  
702 troscopic sample (488065214) was found to have bad MOF mag-  
703 nitudes (MOF\_CM\_MAG\_CORRECTED magnitudes of -9999 for all  
704 bands), and two other galaxies (488069251, 488066060) were  
705 found to have bad MOF fits, with unrealistically large sizes  
706 (MOF\_CM\_T values on the order of  $\sim 5000$  square arcseconds) and  
707 MOF\_CM\_MAG\_CORRECTED\_I magnitudes that are brighter than their  
708 MAG\_AUTO\_CORRECTED\_I magnitudes by more than 4 magnitudes  
709 (18.638176 and 17.868253 compared to 23.349312 and 22.776083  
710 respectively). For these three galaxies with spurious MOF photom-  
711 etry, we used the MAG\_AUTO\_CORRECTED photometry to calculate  
712 the stellar masses of these galaxies instead.

For completeness, we also calculated the flexion shifts of all  
likely galaxies with photometric redshift estimates in the DES "Y3  
Gold" photometric catalog within  $10'$  of the lens galaxies, excluding  
galaxies that are in the spectroscopic sample. To do this, we made the  
following selections to the DES Y3 Gold catalog: First, we selected  
all objects within  $10'$  of the lens galaxies in the Y3 Gold catalog  
that satisfied `FLAGS_GOLD = 0` and `EXTENDED_CLASS_MASH_MOF`  
 `$\geq 2$` , which selected likely galaxies. From this catalog, we ex-  
cluded all galaxies that have `COADD_OBJECT_IDS` that matched  
galaxies already in the spectroscopic sample. We then selected ob-  
jects with DNF photometric redshifts that satisfied `DNF_ZMEAN_SOF`  
 `$> 0$`  and `DNF_ZSIGMA_SOF`  `$< 10$` , which removed several objects  
with spurious redshifts. Finally, we made the following cuts spec-  
ific to the field of each lens galaxy: For DES J0408–5354,  
we removed objects with `COADD_OBJECT_ID = 488068193`,  
488069583, 488067795, as they are features of the lens sys-

tem and not galaxies in the environment of the lens. For WGD 2038–4008, we removed objects with COADD\_OBJECT\_ID = 169192447, 169193208, 169192589, 169193438 as they are misclassified stars, and reincluded 169190696, which is a galaxy misclassified as a star (see footnote in §2.3.2). After applying these selection criteria, we obtained a photometric catalog of 5082 objects within 10' of DES J0408–5354 and 4438 objects within 10' of WGD 2038–4008. We then performed the same analysis on these objects as on the spectroscopic sample, using DNF\_ZMEAN\_SOF in lieu of spectroscopic redshift when necessary.

For the lens galaxies, we use the following quantities in our analysis: For DES J0408–5354, we use coordinates {RA, DEC} = {62.090417, –53.899889}, lens redshift  $z_d = 0.59671$ , source redshift  $z_s = 2.375$ , and Einstein radius  $\theta_E = 1.80$  (Lin et al. 2017; Shajib et al. 2019b). For WGD 2038–4008, we use {RA, DEC} = {309.511379, –40.137024},  $z_d = 0.22829$ ,  $z_s = 0.777$ ,  $\theta_E = 1.38$  (Agnello et al. 2018; Shajib et al. 2019b).

### 6.1.1 Individual Galaxies

We follow the general methodology described in Sluse et al. (2019) to estimate the Einstein radii of galaxies.

First, we inferred the stellar masses of galaxies from DES photometry using the galaxy template fitting code Le PHARE (see §3.3). We then use an empirical scaling relation to estimate the line-of-sight central velocity dispersion of the galaxy,  $\sigma$ . In this work, we use and compare results derived from two different scaling relations, one from Zahid et al. (2016) and another from Auger et al. (2010). The Zahid et al. (2016) relation was derived from a sample of  $\sim 3.7 \times 10^5$  SDSS elliptical galaxies at  $z < 0.7$  with stellar masses in the range  $\log_{10}(M_\star/M_\odot) \in [9.5, 11.5]$ . The relation is fit with a broken power law given by Eqn 5 of Zahid et al. (2016), which we rewrite here in logarithmic form:

$$\begin{aligned} \log_{10}(\sigma) &= \log_{10}(\sigma_b) + \alpha_1 (\log_{10}(M_\star) - \log_{10}(M_b)) \text{ for } M_\star \leq M_{b06} \\ \log_{10}(\sigma) &= \log_{10}(\sigma_b) + \alpha_2 (\log_{10}(M_\star) - \log_{10}(M_b)) \text{ for } M_\star > M_{b07} \end{aligned} \quad (8)$$

where  $\log_{10}(\sigma_b) = 2.073$ ,  $\log_{10}(M_b/M_\odot) = 10.26$ ,  $\alpha_1 = 0.403$ , and  $\alpha_2 = 0.293$ . Since Zahid et al. (2016) found no significant change of the scaling relation at different redshift bins, we assume that the stellar-mass-to-velocity-dispersion scaling relation does not evolve with redshift.

Alternatively, we also used the scaling relation from Auger et al. (2010), which was obtained from fitting a sample of 73 elliptical galaxy lenses from the SLACS survey. The best-fit relation is

$$\log_{10}(\sigma) = 0.18 \log_{10} \left( M_\star / (10^{11} M_\odot) \right) + 2.34 \quad (9)$$

where we have opted to use the best fit parameters for the model that includes the intrinsic scatter, which is  $0.04 \pm 0.01$  in the fit. The elliptical galaxies used for this fit are generally more massive compared to the sample used in the Zahid et al. (2016) analysis, and have stellar masses in the range  $\log_{10}(M_\star/M_\odot) \in [10.5, 12]$ . We also assume that the stellar-mass-to-velocity-dispersion scaling relation does not evolve with redshift.

Once we obtain line-of-sight velocity dispersion estimates for each galaxy, we convert the velocity dispersion to the Einstein radius,  $\theta_{E,p}$ , assuming a Singular Isothermal Sphere (SIS) model

$$\theta_{E,p} = 4\pi \left( \frac{\sigma}{c} \right)^2 \frac{D_{ps}}{D_{os}} \quad (10)$$

, from which the flexion shift can be calculated with Eq.(5).

The uncertainties for the flexion shifts are calculated by adding two different sources of uncertainty in quadrature. The first source comes from the uncertainty in the stellar mass estimates from Le PHARE. The second source of uncertainty comes from the intrinsic scatter in the scaling relation between stellar mass and velocity dispersion. For the Zahid et al. (2016) relation, we quantify this uncertainty by taking half the difference in the central 68th percentile limits of the velocity dispersion distribution at a given stellar mass and use that as the uncertainty from the intrinsic scatter of the scaling relation (see Figure 9(A) of Zahid et al. 2016). For the Auger et al. (2010) relation, we use their fit for the intrinsic scatter, which is  $\Delta \log_{10}(\sigma) = 0.05$  (taking the more conservative limit). The two sources of uncertainties are added in quadrature, and then propagated forward into an uncertainty in the flexion shift.

Flexion shift estimates for galaxies in the spectroscopic sample with stellar mass estimates that are significantly outside the mass ranges used to derive the Zahid et al. (2016) and Auger et al. (2010) scaling relations should be treated with caution, as the scaling relations (and errors) are extrapolated. Therefore, flexion shift estimates for galaxies in our sample with stellar masses  $\log_{10}(M_\star/M_\odot) < 9.5$  should be treated with caution, as both the scaling relations from Zahid et al. (2016) and Auger et al. (2010) may not be valid at the lower end of the stellar mass range. However, the validity of this extrapolation does not affect the main results of this study, since the most significant perturbers (i.e. galaxies that contribute the largest flexion shift contributions) tend to be more massive. The 10 galaxies with the largest flexion shift contributions at the lens positions of DES J0408–5354 and WGD 2038–4008 (Table 4) are within the stellar mass ranges used to derive at least one of the two scaling relations.

### 6.1.2 Galaxy Groups

For galaxy-groups, we obtain a probability density function for the Einstein radius by adopting the same SIS approximation described in Eq. (10), and sampling 1000 values from the posterior PDF of the intrinsic velocity dispersion of the groups identified in §5.1 as well as from the bootstrapped PDF of the redshift of each group.

To obtain the flexion shifts of the galaxy groups and corresponding uncertainties, we use Eq. (5), sampling from the PDF of the Einstein radius as well as the bootstrapped group centroid position.

## 6.2 Flexion shifts for galaxies and galaxy groups in the field of DES J0408–5354 and WGD 2038–4008

We present a table of the properties of the 10 galaxies with the largest flexion shifts at the lens position in the fields of DES J0408–5354 and WGD 2038–4008. Comparing the results from the two scaling relations, The scaling relation from Auger et al. (2010) is shallower than the fit by Zahid et al. (2016), but produces larger estimates of the line-of-sight velocity dispersion for galaxies with stellar masses  $\log_{10}(M_\star/M_\odot) \lesssim 11.45$ . Since the majority of galaxies in the sample have smaller stellar mass estimates than that, the Auger et al. (2010) scaling relation produces larger flexion shifts than that from the Zahid et al. (2016) for this sample, and can be treated as the more conservative estimate of

**Table 4.** Properties of the 10 galaxies with the largest flexion shifts, sorted in order of decreasing 68th percentile upper limits, in the field of DES J0408–5354 and WGD 2038–4008. The columns display, in order, the DES Y3 Object ID (and ID used in future papers), coordinates (RA, DEC in degrees; ICRS), redshift  $z$ , distances to the lensing galaxy and flexion shifts, calculated using the scaling relations by Zahid et al. (2016) and Auger et al. (2010) respectively. Galaxies marked with \* are not in the spectroscopic survey and only have photometric redshifts; we report the DNF\_ZMEAN\_SOF redshift value and DNF\_ZSIGMA\_SOF uncertainties. Spectroscopic redshift uncertainties are about  $100 \text{ km s}^{-1}$ , or 0.00033 in redshift. Stellar masses and corresponding uncertainties were calculated using the Le PHARE galaxy template fitting code and DES Y3 photometry (see §3.3). Galaxies marked with † have spurious MOF magnitudes. For these galaxies, we use MAG\_AUTO\_CORRECTED photometry to calculate stellar masses instead. Flexion shifts and uncertainties are calculated following the method described in §6.1-6.1.1. For a complete list of galaxies, see Table A1

ID	RA (deg)	DEC (deg)	$z$	$i$ -band Magnitude	$\log_{10}(M_*)$ ( $\log_{10}(M_{\odot})$ )	$\Delta\theta$ (arcsec)	$\log_{10}(\Delta_3 x_{\text{Zahid}})$ ( $\log_{10}(\text{arcsec})$ )	$\log_{10}(\Delta_3 x_{\text{Auger}})$ ( $\log_{10}(\text{arcsec})$ )
DES J0408–5354								
488068102 (G3)	62.090965	-53.901634	0.76866	20.096	$11.42^{+0.10}_{-0.12}$	6.4	$-2.21^{+0.25}_{-0.29}$	$-2.20^{+0.21}_{-0.22}$
488065185 (G6)	62.095575	-53.898291	0.59441	21.867	$10.29^{+0.10}_{-0.17}$	12.4	$-3.95^{+0.42}_{-0.58}$	$-3.42^{+0.21}_{-0.24}$
488066144 (G4)	62.090243	-53.903609	0.77069	22.015	$10.66^{+0.13}_{-0.17}$	13.4	$-4.07^{+0.38}_{-0.51}$	$-3.72^{+0.22}_{-0.24}$
488066768 (G5)	62.092923	-53.900091	1.03197	23.682	$9.68^{+0.24}_{-0.25}$	5.4	$-4.93^{+0.63}_{-0.93}$	$-3.87^{+0.26}_{-0.27}$
488066462	62.083912	-53.903969	0.60048	22.304	$9.88^{+0.12}_{-0.19}$	20.2	$-5.24^{+0.52}_{-0.79}$	$-4.37^{+0.22}_{-0.25}$
MUSE6 / 488065214 †	62.077898	-53.903878	0.59797	22.303	$10.37^{+0.11}_{-0.16}$	30.2	$-5.02^{+0.41}_{-0.56}$	$-4.53^{+0.21}_{-0.23}$
488070148	62.084648	-53.885204	0.27247	18.309	$10.99^{+0.04}_{-0.04}$	54.3	$-4.81^{+0.31}_{-0.37}$	$-4.61^{+0.20}_{-0.20}$
488066886	62.090541	-53.904725	0.77568	22.925	$9.91^{+0.16}_{-0.30}$	17.4	$-5.46^{+0.53}_{-0.90}$	$-4.61^{+0.23}_{-0.30}$
488070807	62.072770	-53.910296	0.59811	19.975	$11.27^{+0.05}_{-0.06}$	53.0	$-4.69^{+0.25}_{-0.30}$	$-4.61^{+0.20}_{-0.21}$
MUSE8 / 488067782	62.103108	-53.897861	0.59832	22.100	$10.11^{+0.13}_{-0.20}$	27.9	$-5.29^{+0.48}_{-0.71}$	$-4.62^{+0.22}_{-0.25}$
WGD 2038–4008								
169192350 *	309.514393	-40.137815	$0.349 \pm 0.033$	21.999	$9.53^{+0.15}_{-0.29}$	8.8	$-5.71^{+0.59}_{-1.03}$	$-4.52^{+0.22}_{-0.30}$
169193255 *	309.529391	-40.151522	$0.240 \pm 0.138$	18.806	$10.76^{+0.06}_{-0.10}$	72.0	$-5.94^{+0.35}_{-0.45}$	$-5.63^{+0.20}_{-0.21}$
169190952 *	309.503723	-40.120144	$0.277 \pm 0.021$	19.052	$10.78^{+0.05}_{-0.09}$	64.3	$-6.02^{+0.34}_{-0.44}$	$-5.72^{+0.20}_{-0.21}$
169192931 *	309.508988	-40.144869	$0.421 \pm 0.044$	20.446	$10.62^{+0.05}_{-0.07}$	29.0	$-6.17^{+0.37}_{-0.47}$	$-5.80^{+0.20}_{-0.21}$
169191098 *	309.487406	-40.124006	$0.238 \pm 0.016$	18.360	$10.69^{+0.04}_{-0.03}$	80.9	$-6.16^{+0.36}_{-0.45}$	$-5.82^{+0.20}_{-0.20}$
169191973 *	309.536238	-40.134562	$0.331 \pm 0.011$	18.444	$11.15^{+0.03}_{-0.03}$	69.0	$-6.05^{+0.27}_{-0.33}$	$-5.92^{+0.20}_{-0.20}$
169193929 *	309.520149	-40.160086	$0.250 \pm 0.005$	19.137	$10.63^{+0.05}_{-0.09}$	86.5	$-6.41^{+0.36}_{-0.47}$	$-6.04^{+0.20}_{-0.21}$
169190452	309.539131	-40.115839	0.22917	18.213	$10.76^{+0.04}_{-0.04}$	107.9	$-6.39^{+0.35}_{-0.43}$	$-6.08^{+0.20}_{-0.20}$
169192596	309.492815	-40.140131	0.23003	21.389	$9.28^{+0.11}_{-0.18}$	52.3	$-7.61^{+0.60}_{-0.96}$	$-6.21^{+0.21}_{-0.24}$
169191228	309.535586	-40.122881	0.22900	20.025	$10.13^{+0.07}_{-0.11}$	83.9	$-6.86^{+0.45}_{-0.62}$	$-6.21^{+0.21}_{-0.22}$

**Note:** \* Galaxy is not in the spectroscopy survey; stellar masses and flexion shift estimates are from photometric redshifts.

† Galaxy has spurious MOF photometry. For these galaxies, we use MAG\_AUTO\_CORRECTED photometry to calculate stellar masses instead.

the two. In figures 9 and 10, we show the distribution of flexion shifts of the spectroscopic and photometric catalogs for the environment of DES J0408–5354 and WGD 2038–4008, using both the Zahid et al. (2016) and Auger et al. (2010) scaling relations. The  $\log_{10}(\Delta_3 x) > -4$  criteria is indicated by the dashed vertical line.

When calculating flexion shifts for the photometric catalog, we found some objects with spurious MOF\_CM\_MAG\_CORRECTED photometry. For these objects we instead used stellar masses computed from MAG\_AUTO photometry, including the same Milky Way extinction and other photometric corrections as for the MOF magnitudes.

Using this criterion, for DES J0408–5354, there are four galaxies (G3, G4, G5, G6) with flexion shift contributions above  $\log_{10}(\Delta_3 x) > -4$  when using the stellar masses from the Auger et al. (2010) scaling relation. These four galaxies are explicitly modeled in the lens model analysis (Shajib et al. 2019a). In addition, the group including the lensing galaxy, group 5, has a flexion shift of  $-3.86^{+0.97}_{-0.72}$ ". The large uncertainties in the flexion shift of group 5 is due to a combination of the close proximity of the group centroid to DES J0408–5354 and the uncertainty in the centroid

location, with the upper limits of the flexion shift being produced when the group centroid is near the lens galaxy.

For WGD 2038–4008, we did not identify any galaxies or galaxy groups with a flexion shift  $\log_{10}(\Delta_3 x) > -4$ .

### 6.3 Photometrically Identified Galaxy-Groups

#### 6.3.1 RedMaPPer Clusters in the Field of the Lenses

Due to the low spectroscopic completeness of the survey of WGD 2038–4008, we complemented our spectroscopic group-identification efforts with a search of all photometrically-identified clusters with richness  $\lambda > 5$  in the field of view of WGD 2038–4008 using the redMaPPer algorithm Rykoff et al. (2014). We used the sixth release of the redMaPPer cluster catalog on DES Y3A2 data (v6.4.22+2) and found two redMaPPer clusters within 3' of WGD 2038–4008 (with unique IDs MEM\_MATCH\_ID = 62659, 138669).

One of the clusters (62659) has a photometric cluster redshift of  $z_{\text{photo}} = 0.221 \pm 0.008$  and a richness of



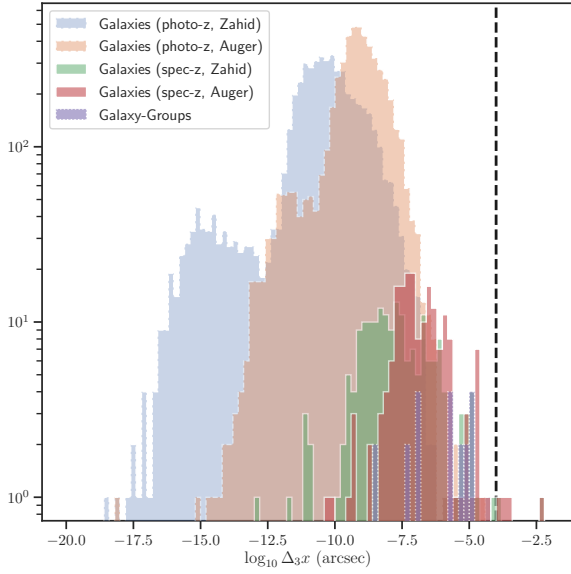


**Figure 9.** Flexion shift histograms for galaxies and galaxy groups in the environment of DES J0408–5354.

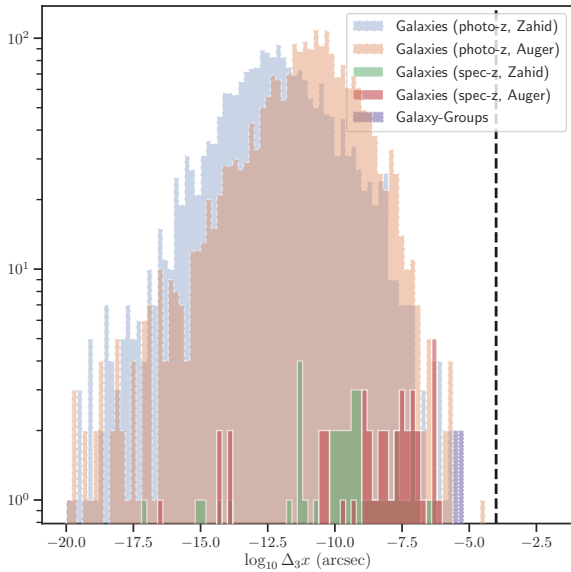


**Figure 10.** Flexion shift histogram for galaxies and galaxy groups in the environment of WGD 2038–4008.

865  $\lambda = 5.1 \pm 1.7$ . The photometric cluster redshift of cluster  
 866 62659 is consistent with the spectroscopically-identified Group  
 867 1 ( $z_{\text{group}} = 0.229$ ), and its algorithmically-identified central  
 868 galaxy, COADD\_OBJECT\_ID = 169190452, is also a member of  
 869 Group 1 (see Table A2), suggesting that redMaPPer cluster  
 870 62659 and Group 1 are the same group. Only two of the  
 871 seven spectroscopically-identified group members in Group 1  
 872 (COADD\_OBJECT\_ID = 169190452, 169189459) are also mem-  
 873 bers of the redMaPPer cluster 62659. However, this could be sim-  
 874 ply due to bad photometric redshift estimates, as 4 of the 5 group  
 875 members have DNF\_ZMEAN\_SOF photometric redshift estimates that  
 876 range from 0.38 – 0.44, and the lens galaxy (169191076) has a  
 877 spurious redshift estimate of 0.00977.

878 The second redMaPPer cluster (138669) has a cluster redshift  
 879 of  $z_{\text{photo}} = 0.405 \pm 0.017$  and a richness of  $\lambda = 10.8 \pm 2.0$ . None  
 880 of the galaxies in this cluster share group membership with the  
 881 spectroscopically-identified Group 2, suggesting that this group is  
 882 distinct from Group 2.

883 For completeness, we also searched for redMaPPer clusters in  
 884 the field of DES J0408–5354, though the spectroscopic complete-  
 885 ness of the field of DES J0408–5354 is much higher than that of  
 886 WGD 2038–4008. However, we did not find any clusters within  
 887 3' of DES J0408–5354. One reason for this paucity is that a nearby  
 888 region of the lens has been flagged and precluded from redMaPPer  
 889 analysis due to a bright star in the foreground.

### 890 6.3.2 Flexion Shifts for redMaPPer Clusters near the lenses

891 We performed the same flexion shift calculations on the redMaP-  
 892 Per clusters as the spectroscopic groups, following the procedure  
 893 outlined in §6.1, using the same lens parameter quantities, and us-  
 894 ing the same conservative SIS approximation described by Eq. 10  
 895 for the perturber. We use the scaling relation given by Eq. (17) of  
 896 Andreon & Hurn (2010) to convert the cluster richness into a ve-  
 897 locity dispersion estimates for the SIS model. From this, we obtain  
 898 flexion shifts for the redMaPPer clusters. For cluster 62659, we ob-  
 899 tain a flexion shift of  $\log_{10}(\Delta_3x) = -5.1^{+0.3}_{-0.4}$ . For cluster 138669,  
 900 we obtain a flexion shift of  $\log_{10}(\Delta_3x) = -6.0 \pm 0.2$ . The esti-  
 901 mated uncertainties come from propagating both the uncertainties  
 902 in cluster richness, as well as the uncertainties in the scaling rela-  
 903 tion. The properties of both groups are summarized in Table A3.  
 904 Neither redMaPPer groups in the field of WGD 2038–4008 exceeds  
 905 the threshold of  $\log_{10}(\Delta_3x) > -4$ .

## 906 7 DETERMINING LINE-OF-SIGHT UNDER/OVERDENSITIES USING WEIGHTED NUMBER COUNTS

### 909 7.1 Description of the technique

910 To determine the line-of-sight under/overdensities we follow the  
 911 technique described in section 5 of Rusu et al. (2017). Like the  
 912 CFHTLenS control fields used in Rusu et al. (2017), the DES fields  
 913 also have saturated stars and other artifacts that are masked. Each  
 914 DES coadd tile contains a mask plane that contains the bleed trails  
 915 for the saturated stars but not the mask for the stars themselves. The  
 916 masks for the stars and other artifacts such as dead CCD regions  
 917 are contained in the mang1e masks (Swanson et al. 2008; Hamilton  
 918 & Tegmark 2004) that are computed by DESDM for each tile. As  
 919 can be seen from the upper image in Figure 3 there is a large  
 920 saturated star in the DES J0408–5354 field close to the lens. The  
 921  $i$ -band and  $z$ -band mang1e masks defined a very large mask around  
 922 this star such that the entire  $1000 \times 1000$  pixel area around the  
 923 lens was masked. We therefore chose to use the mang1e masks for  
 924 the  $r$ -band images for both the target field and the control fields  
 925 which did not have this problem. We also chose to use the  $r$ -band  
 926 mask for WGD 2038–4008 for consistency. For each field (target  
 927 and control) we combine the mask plane and the mang1e mask  
 928 to obtain the complete mask. We also use a  $5.26''$  radius mask at  
 929 the center of the DES J0408–5354 target field and a  $2.63''$  radius  
 930 mask for WGD 2038–4008 to remove the lensing galaxy and quasar  
 931 images from the calculation. We then apply each control field mask  
 932 to the target field and apply the target field mask to each control  
 933 field, as described in section 5.1 of Rusu et al. (2017). Following

the example of (Rusu et al. 2019), for DES J0408–5354 we are manually removing from the target field catalogue four galaxies that are incorporated in the mass models of Shajib et al. (2019a), in order to avoid double-counting their contribution to  $\kappa_{\text{ext}}$ .

We compute the median of the weighted counts for the target field  $W_q^{\text{meds},t} = N_{\text{gal}}^t \times \text{median}(q_i^t)$ , where  $q_i^t$  is the chosen weighting scheme, with  $i = 1, \dots, N_{\text{gal}}^t$  and  $N_{\text{gal}}^t$  is the number of galaxies in the aperture. We compute the same quantity for the control field  $W_q^{\text{meds},c} = N_{\text{gal}}^c \times \text{median}(q_i^c)$ . For each target field and control field combination we calculate the ratio  $\zeta_q = W_q^{\text{meds},t} / W_q^{\text{meds},c}$  for each target and control field combination. Our final weighted count for weighting scheme  $q$  is the median of this ratio over all target/control field combinations  $\overline{\zeta_q^{\text{meds}}}$ .

We focus on four weighting schemes we used in Birrer et al. (2019),  $q = 1$  which is just the raw counts  $N_{\text{gal}}^t / N_{\text{gal}}^c$ , weighting by redshift  $q_z = z_s \times z_i - z_i^2$ , weighting by distance to the lens/center of the field  $q_r = 1/r$  and weighting by distance to the lens/center of the field and redshift  $q_{z/r} = (z_s \times z_i - z_i^2)/r$ . We have used two apertures, one of radius  $120''$  and the other of radius  $45''$ . In Figure 11 and Figure 12 we show the relative weights of each galaxy in the DES J0408–5354 and WGD 2038–4008 fields for  $i < 22.5$  and the two apertures  $120''$  and  $45''$ .

## 7.2 Resulting distribution for $\zeta_q$

We present our results for  $\overline{\zeta_q^{\text{meds}}}$  in Table 5. The uncertainties are derived from taking 20 samplings of the redshift and magnitude errors from a Gaussian PDF distribution corresponding to each galaxy. We show the results for both apertures and for both the DNF and BPZ redshift selections. In Figure 13 we show the ratio  $\zeta_q^{\text{meds}}$  for the four weighting schemes for both DES J0408–5354 and WGD 2038–4008. Figure 14 shows a radial plot of the measured over/underdensity for each weight for four different aperture radii:  $45''$ ,  $60''$ ,  $90''$  and  $120''$  for both DES J0408–5354 and WGD 2038–4008. Our analysis shows that the field of DES J0408–5354 is significantly under-dense (more so than any of the existing HOLiCOW lenses), and this is expected to lead to a tight, negative-value distribution of  $\kappa_{\text{ext}}$  (e.g., Greene et al. 2013). On the other hand the field of WGD 2038–4008 is of about unit density in the  $45''$ -aperture, and over-dense in the  $120''$ -aperture compared to the random fields.

## 7.3 Computing simulated $\zeta_q$ in the MS

We follow the approach described in Rusu et al. (2017), in order to implement the same observational constraints to the galaxies in the MS as are relevant to the computation of  $\zeta_q$  in the DES data. MS is a dark matter-only simulation of the  $\Lambda$ CDM cosmology, having a periodic box of  $500 h^{-1} \text{Mpc}$  on a side with  $2160^3 \approx 1.0078 \times 10^{10}$  particles. The simulation run was performed with a modified version of the GADGET-2 code Springel et al. (2005); Lemson & Virgo Consortium (2006) and has the spatial resolution limit of  $5 h^{-1} \text{kpc}$  (Plummer-equivalent). The mass resolution  $8.6 \times 10^8 h^{-1} M_{\odot}$  and the volume are enough to include a large variety of well-resolved objects from faint quasars to galaxy-clusters. Galaxies can be painted onto these dark matter-only halos using semi-analytical models. Previous HOLiCOW work has employed the models by De Lucia & Blaizot (2007), but here we are also exploring, for comparison, the newer models of Henriques et al. (2015). The assignment of these galaxies to halos follows different physical prescriptions, which are

adjusted to fit typically low redshift observables. The available catalogues contain synthetic photometry in various bands; we select the *griz* magnitudes for each galaxy, and sample from them by assigning uncertainties taken from observed DES galaxies, over the same range of magnitude bins. We account for the fraction of galaxies in the target fields that have available spectroscopy, and also for the known DES galaxy-star contamination and incompleteness fractions. The latter fractions are corrected to account for the fraction of the target field apertures covered by *HST*, as *HST* imaging is assumed to result in the most reliable classification.

In Figure 15 we plot the resulting comparison of photometric redshifts and catalogue redshifts for a representative sample of the De Lucia & Blaizot (2007) and Henriques et al. (2015) galaxies, up to the redshift of DES J0408–5354 (including for the redshift limit of WGD 2038–4008). Our photometric redshifts measured with BPZ have negligible bias up to a redshift of  $z \sim 1$ , above which there is significant scatter, due to the absence of infrared photometry beyond  $z$ -band. For the De Lucia & Blaizot (2007) models this is a small effect, as there are very few galaxies above this redshift (Figure 16), but the effect may be more pronounced for the Henriques et al. (2015) models, which predict a significant number of galaxies at large redshift.

## 8 DETERMINING $P(\kappa_{\text{EXT}})$

Our method of obtaining  $P(\kappa_{\text{ext}})$  relies on selecting lines of sight from the MS which match the observed  $\zeta_q$  constraints, and constructing the PDF of their associated  $\kappa_{\text{ext}}$  distributions, using the  $\kappa_{\text{ext}}$  maps produced by the ray tracing technique of Hilbert et al. (2009). This method has been described in detail in Rusu et al. (2017), and updated in Birrer et al. (2019) and Rusu et al. (2019). One point we wish to emphasize is that when we computed the relative over/underdensity of the DES J0408–5354 lens fields in Section 7.1 we removed individual galaxy perturbers that were explicitly incorporated into the lens modeling. By doing so, we ensure that these galaxies do not contribute to the  $P(\kappa_{\text{ext}})$  we estimate, and we therefore avoid biasing our estimate high. This is accomplished without the need to alter the input  $\kappa_{\text{ext}}$  maps.

Furthermore, we have shown in Section 6.2 that the group of galaxies at the redshift of the lens in DES J0408–5354 contributes a flexion shift close to our threshold for incorporating this structure into the mass models. We therefore compute  $P(\kappa_{\text{ext}})$  for two cases. In the first case, “w/group”, we ignore the existence of this structure, and we include the LOS contribution of the constituent galaxies to  $P(\kappa_{\text{ext}})$ . In the second case, “w/o group”, we expect that the structure will be included in the lensing models of Shajib et al. (2019a), Yildirim et al. in prep. and Wong et al. in prep, and we therefore exclude it from the LOS analysis. This is accomplished by removing the galaxy group members from the catalogue of galaxies around the lens, when computing the weighted count ratio constraints reported in Table 5. We adopt the technique from Rusu et al. (2019) and Chen et al. (2019) to account for spectroscopic incompleteness. That technique consists of two different methods, one which uses the Andreon & Hurn (2010) relation between group velocity dispersion and richness, and one which assumes Poisson statistics to compute the number of additional galaxy members potentially missed due to sparse spectroscopy. We choose to use only the second method, as the first relies on numerous physical assumptions, and cannot reconcile the small velocity dispersion of the group ( $\sim 230 \text{ km/s}$ ) with the large number of observed members (17). We found a similar

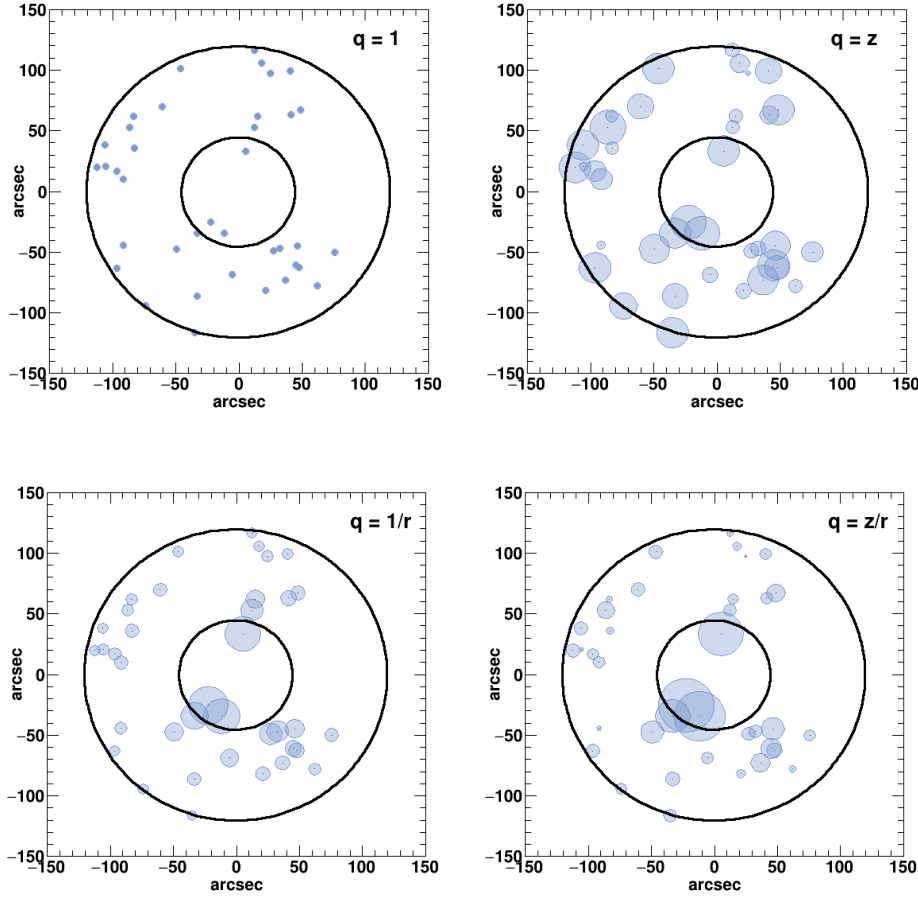


**Figure 11.** The relative weights of the galaxies around DES J0408–5354 for the four weighting schemes  $q = 1$ ,  $q_z = z_s \times z_i - z_i^2$ ,  $q_r = 1/r$  and  $q_{z/r} = (z_s \times z_i - z_i^2)/r$ . The galaxies satisfy  $i < 22.5$  and are represented by circles with areas proportional to their weights. The black circles indicate the 120'' and 45'' apertures.

mismatch between the two methods in [Chen et al. \(2019\)](#) for the lens PG 1115+080.

In Figures 17 and 18 we plot the resulting distributions of  $P(\kappa_{\text{ext}})$  for DES J0408–5354 and WGD 2038–4008, respectively, for a selection of weights, using the [De Lucia & Blaizot \(2007\)](#) galaxy models. The  $\zeta_q$  constraints are taken from Table 5, where we marginalize over the DNF and BPZ values. As in [Birrer et al. \(2019\)](#); [Rusu et al. \(2019\)](#), we combine the  $\zeta_q$  constraints from the 45'' and 120'' apertures. We consider as fiducial distributions, to be used in the cosmological analysis, the ones which use as constraints the most robust  $\zeta_q$  constraints, i.e. those with  $q = 1$  and  $q = 1/r$  in both apertures. In previous work we also used the external shear values corresponding to the best-fit mass models as an additional constraint. At the time our analysis was completed, the final shear values from [Yildirim et al. in prep.](#) and [Wong et al. in prep.](#), which will complement the cosmographic inference of [Shajib et al. \(2019a\)](#), as well as for WGD 2038–4008, were unknown. Therefore, we choose to report the statistics of  $P(\kappa_{\text{ext}} | \zeta_1^{45''}, \zeta_{1/r}^{45''}, \zeta_1^{120''}, \zeta_{1/r}^{120''}, \gamma)$  for a variety of  $\gamma$  values, in Table 6.

For the choices in Figure 17, we found that the use of the [Henriques et al. \(2015\)](#) models results in  $P(\kappa_{\text{ext}})$  lower by  $\kappa_{\text{ext}} \lesssim 0.01$ , therefore at the  $\lesssim 1\%$  level. Based on the fact that the photometric redshift distribution of the DES galaxies in Figure 16 is more consis-

tent with that of the [De Lucia & Blaizot \(2007\)](#) models (e.g., the large peak at  $z \sim 0.5$  and the absence of galaxies above  $z \sim 1.5$ ), as well as for consistency with our previous work on H0LiCOW lenses, we adopt the [De Lucia & Blaizot \(2007\)](#) models. We will test in more detail the impact of a particular choice of semi-analytical galaxy models, which appears to be comparatively larger for large source redshifts and over/under-densities, in another work, [Mukherjee et al., in prep.](#)

As expected from the significantly underdense field of DES J0408–5354, the resulting fiducial  $P(\kappa_{\text{ext}})$  distributions are tight (approximately 0.03 width in  $\kappa_{\text{ext}}$ ), with medians around  $\kappa_{\text{ext}} \sim -0.04$  -  $-0.05$ , or 4 - 5%.<sup>5</sup> As the group contribution is removed from the LOS,  $P(\kappa_{\text{ext}})$  decreases by  $\lesssim 0.01$ .

<sup>5</sup> The distributions of  $P(\kappa_{\text{ext}})$  presented in this paper differ slightly from the ones used in the blind cosmographic analysis of DES J0408–5354 by [Shajib et al. \(2019a\)](#). In addition to that work using the shear constraint derived therein, there is a minor difference owing to a clerical error discovered after unblinding, which corresponds to a change in  $H_0$  of 0.13%, much smaller than the statistical uncertainty of 3.9%. In order to preserve the blindness of the  $H_0$  measurement, this correction has not been propagated through the [Shajib et al. \(2019a\)](#) measurement. However, future measurements based on DES J0408–5354 should use the corrected distribution of  $P(\kappa_{\text{ext}})$  given in this paper.

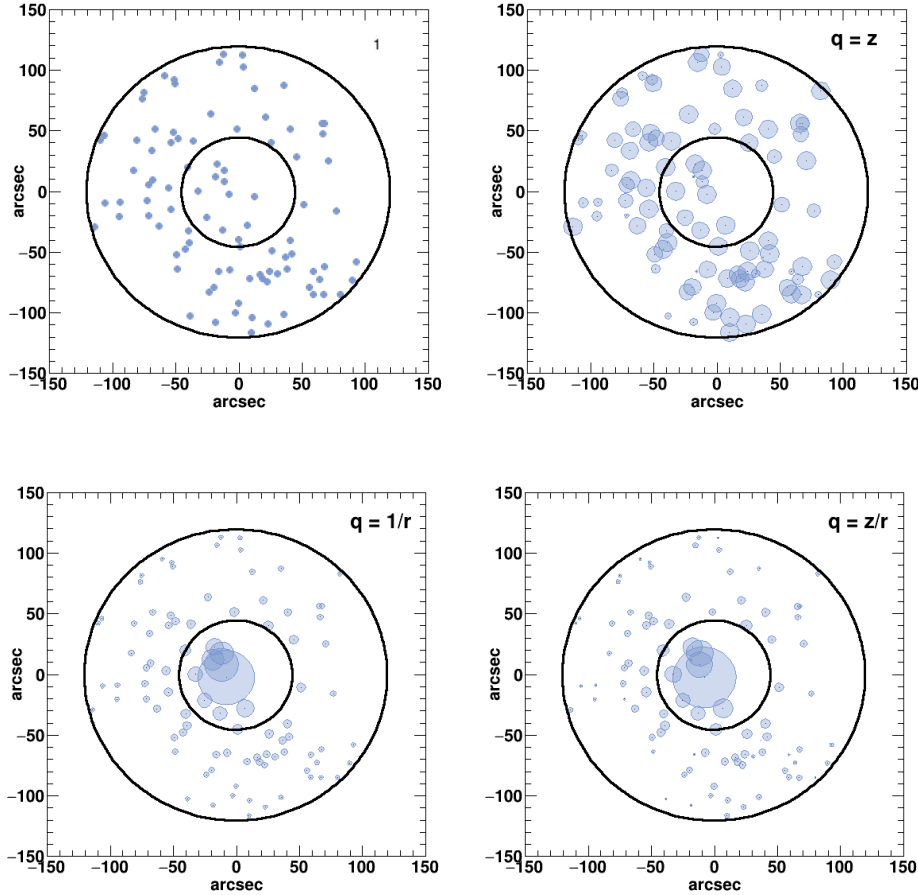


**Figure 12.** The relative weights of the galaxies around WGD 2038–4008 for the four weighting schemes  $q = 1$ ,  $q_z = z_s \times z_i - z_i^2$ ,  $q_r = 1/r$  and  $q_{z/r} = (z_s \times z_i - z_i^2)/r$ . The galaxies satisfy  $i < 22.5$  and are represented by circles with areas proportional to their weights. The black circles indicate the 120'' and 45'' apertures.

1084 The distributions for WGD 2038–4008 are much tighter, with 1105  
 1085 width  $\sim 1\%$ . This is expected due to the significantly lower source 1106  
 1086 redshift, as there are fewer structures in the MS along the LOS 1107  
 1087 to contribute convergence. The tightening of the distributions as 1108  
 1088 information from multiple apertures is used is evident (see also 1109  
 1089 Figure E2 in Rusu et al. 2019). The medians of the distributions are 1110  
 1090 close to null. 1111

1091 Appendix C of Rusu et al. (2017) shows that our use of the MS 1112  
 1092 to derive  $P(\kappa_{\text{ext}})$  can bias the inference because of the different set 1113  
 1093 of assumed cosmological parameters. However, since our  $P(\kappa_{\text{ext}})$  1114  
 1094 is close to zero, the expected value of the bias, if we assume the 1115  
 1095 cosmological parameters derived from *Planck* (e.g., *Planck Collab-* 1116  
 1096 *oration et al. 2016*), is at a level of  $\sim 0.5\%$ , below the 1% level of 1117  
 1097 accuracy currently aimed at from time delay cosmography (Suyu 1118  
 1098 et al. 2017). 1119

## 1109 9 CONCLUSIONS

1100 In this paper we have presented work on three of the ingredients 1124  
 1101 that are necessary to make a high-precision measurement of the 1125  
 1102 Hubble constant  $H_0$  using the lensed quasars DES J0408–5354 and 1126  
 1103 WGD 2038–4008. These are 1) determining the velocity disper- 1127  
 1104 sion of the lensing galaxy, 2) identifying galaxies and groups along 1128

the line of sight that are close enough to the lens and massive 1105  
 enough that they need to be included in the mass model, and 3) 1106  
 estimating the external convergence  $\kappa_{\text{ext}}$  due to less massive 1107  
 structures that do not need to be included explicitly in the mass 1108  
 model. These ingredients require spectroscopic redshifts for the 1109  
 galaxies in the fields of the two lenses. To obtain these we have car- 1110  
 ried out spectroscopic observations using Gemini South/GMOS-S, 1111  
 Magellan/LDSS-3 and VLT/MUSE. As detailed in §3.1–3.2, we ob- 1112  
 tained a total of 199 high-confidence redshifts from the three instru- 1113  
 ments for DES J0408–5354, corresponding to a redshift complet- 1114  
 eness of 68% for galaxies with  $18 \leq i < 23$  and  $5'' \leq \text{radius} < 3'$ . For 1115  
 WGD 2038–4008 we obtained 54 high-confidence redshifts from 1116  
 the Gemini South/GMOS-S data, with a 16% redshift completeness 1117  
 for the same  $i$ -band magnitude and radius ranges. 1118

As described in §4, in our redshift survey observations we 1119  
 also set aside slits to measure the stellar velocity dispersions of the 1120  
 main lensing galaxies in our two systems. The velocity dispersion 1121  
 of the main deflector G1 in DES J0408–5354 was measured using 1122  
 four independent spectra from the above three instruments, with a 1123  
 consistent result of about  $230 \text{ km s}^{-1}$  (see Table 2). The velocity 1124  
 dispersion for the main lensing galaxy G in WGD 2038–4008 was 1125  
 obtained from one spectrum taken using Gemini South/GMOS-S, 1126  
 with a resulting value of about  $300 \text{ km s}^{-1}$ . The detailed velocity 1127  
 dispersion measurements and uncertainties are given in Table 2. 1128

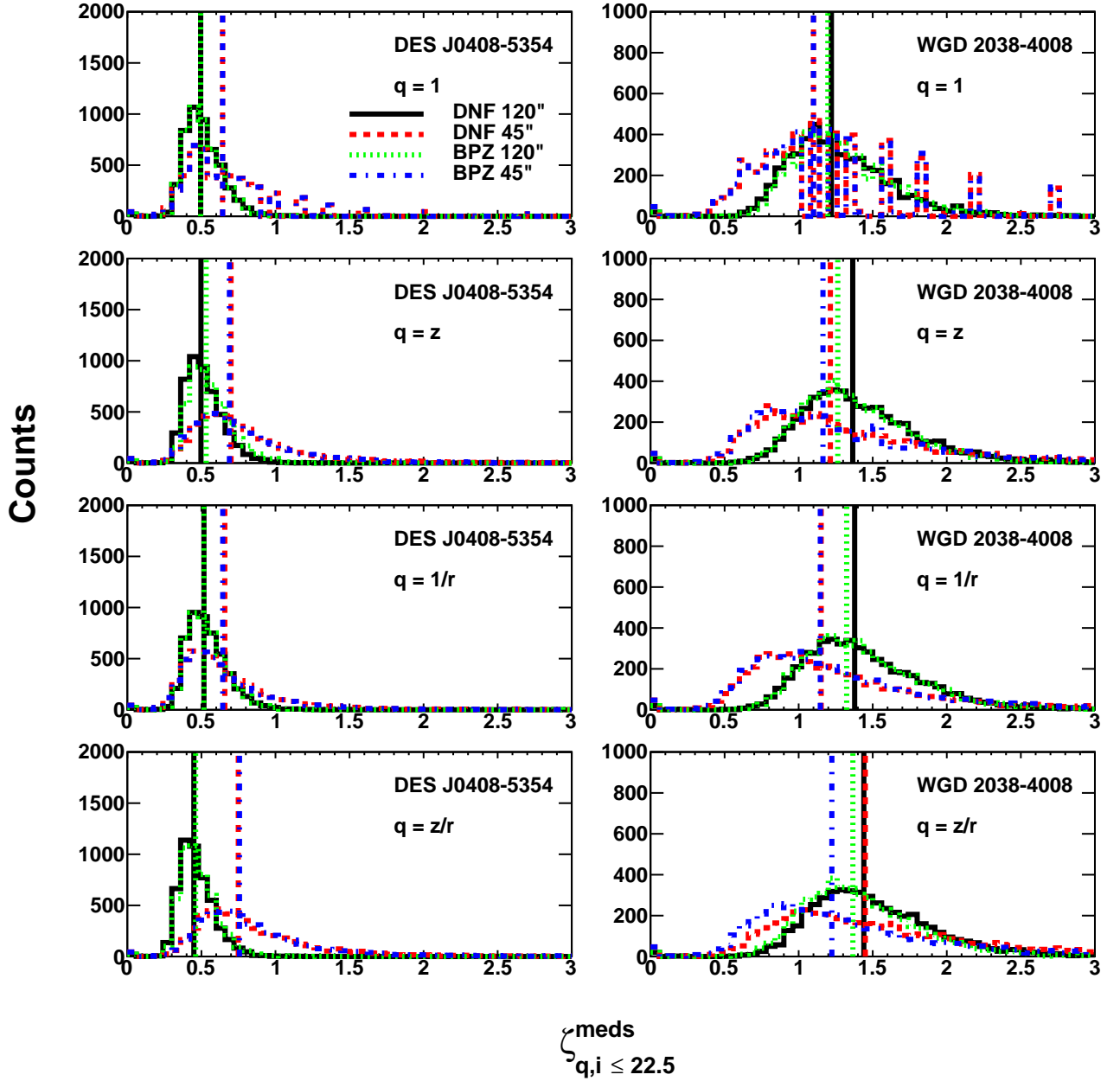


**Figure 13.** The histograms of the weighted ratios for all  $\zeta_q^{meds}$  for DES J0408–5354 and WGD 2038–4008. The vertical lines mark the median of the corresponding distributions. Black solid line - 120'' aperture and DNF redshifts. Green dotted line - 120'' aperture and BPZ redshifts. Red dashed line - 45'' aperture and DNF redshifts. Blue dashed-dotted line - 45'' aperture and BPZ redshifts.

1129 The galaxy group identification uses the spectroscopic red- 1136  
 1130 shifts described above and the same algorithm that was used for 1137  
 1131 the analysis of the H0LiCOW lenses HE 0435–1223 (Sluse et al. 1138  
 2017) and WFI 2033–4723 (Sluse et al. 2019). We find 10 galaxy 1139  
 1132 groups in DES J0408–5354 for which we then compute the flexion 1140  
 1133 shift  $\Delta_{3,x}$  proposed by McCully et al. (2017). McCully et al. (2017) 1141  
 1134 showed that explicitly modeling perturbers with flexion shifts larger 1142

than  $\Delta_{3,x} > 10^{-4}$  allows one to constrain the bias on  $H_0$  due to this uncertainty to the percent level. Out of our 10 groups in DES J0408–5354 we find one group (labelled 5 in Table 3) that has a flexion shift of  $\log_{10} \Delta_{3,x} = -3.86^{+0.97}_{-0.72}$ . This group has 17 members, one of which is the lensing galaxy G1 and the centroid of this group is close to the lens. However Shajib et al. (2019a) show that the change in  $H_0$  of including this group would result

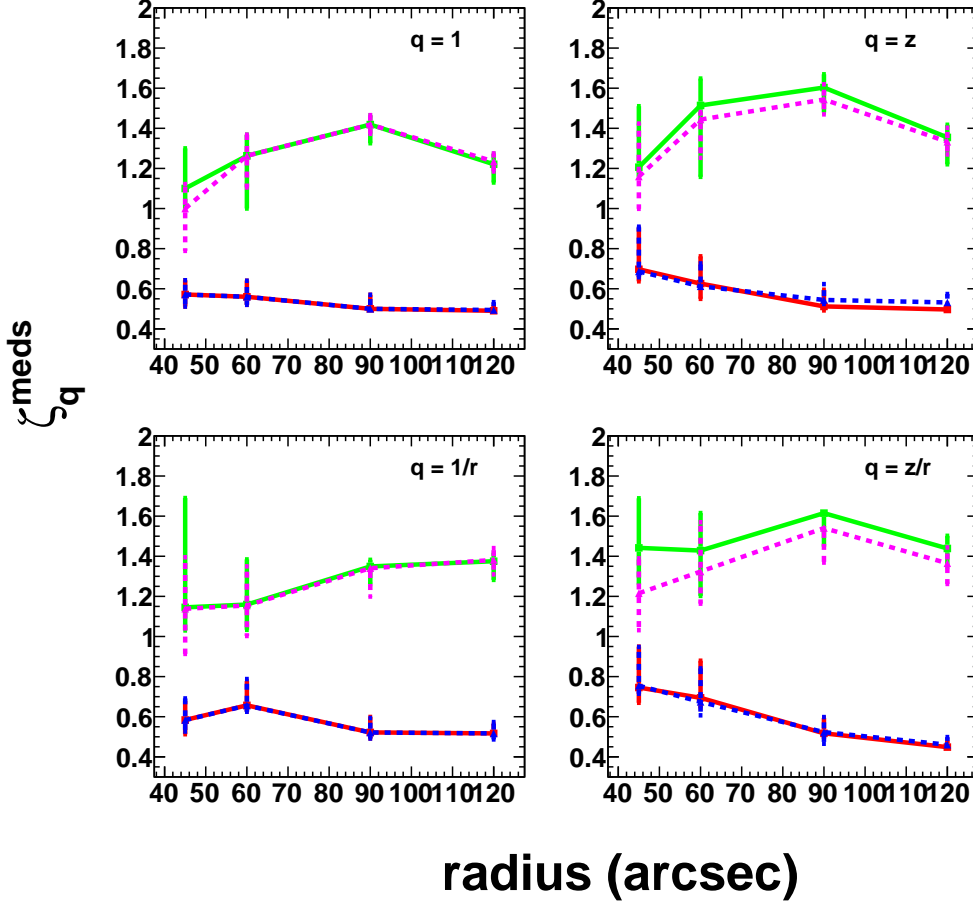


**Figure 14.** Radial plots of the measured weighted count ratios  $\zeta_q^{meds}$  calculated for aperture radii of  $45''$ ,  $60''$ ,  $90''$  and  $120''$ . DES J0408–5354: Red - DNF photometric redshifts, Blue - BPZ photometric redshifts. WGD 2038–4008 : Green - DNF photometric redshifts, Magenta - BPZ photometric redshifts

1143 in a decrease of approximately 0.4 percent so it is not explicitly 1164  
 1144 included in the mass model. For WGD 2038–4008, we find two 1165  
 1145 galaxy groups from our spectroscopic redshift sample, but neither 1166  
 1146 group has flexion shift above our cut. 1167

1147 To calculate the flexion shift for individual galaxies we start 1168  
 1148 with the general methodology described in Sluse et al. (2019) and 1169  
 1149 then use two different scaling relations (Zahid et al. 2016; Auger 1170  
 1150 et al. 2010) to estimate the line-of-sight central velocity dispersion 1171  
 1151 of the galaxy from its stellar mass. The stellar masses are calculated 1172  
 1152 using galaxy model fitting to DES photometry, as detailed in §3.3. 1173  
 1153 The Auger et al. (2010) relation between velocity dispersion and 1174  
 1154 stellar mass gives more conservative, larger flexion shift values, 1175  
 1155 resulting in four galaxies in DES J0408–5354 with flexion shifts 1176  
 1156 larger than our  $\log_{10} \Delta_{3,x} = -4.0$  cut; these galaxies (G3, G4, G5, 1177  
 1157 and G6 in Table 4) are therefore selected for explicit modeling by 1178  
 1158 Shajib et al. (2019a). For WGD 2038–4008, we do not find any 1179  
 1159 individual galaxies with flexion shift greater than our cut. 1180

1160 Our measurement of the external convergence  $\kappa_{ext}$  starts 1181  
 1161 with determining the line-of-sight under/overdensities for 1182  
 1162 DES J0408–5354 and WGD 2038–4008 using weighted number 1183  
 1163 counts. We use a catalog of galaxy properties for the two fields 1184

from the DES Year 3 Gold version 2.2 catalog. As both of these 1185  
 1164 fields are within the DES footprint we are able to select the control 1186  
 1165 fields from the DES catalog as well. This helps us to avoid potential 1187  
 1166 biases due to mismatches in, for example, image resolution between 1188  
 1167 the target and control fields. Where available we use the spectro- 1189  
 1168 scopic redshifts for the galaxies in the target fields. As detailed in §7, 1190  
 1169 for the galaxy counts we use four different sets of weights (including 1191  
 1170 weighting by redshift and/or radius), two different apertures (one 1192  
 1171 of radius  $120''$  and the other of radius  $45''$ ), as well as two photo- 1193  
 1172 metric redshift schemes (DNF and BPZ). For DES J0408–5354 we 1194  
 1173 remove the four galaxies (G3–G6 in Table 4) which are explicitly 1195  
 1174 incorporated into the lens model. Also for DES J0408–5354 we 1196  
 1175 calculate the weighted counts for both the case where the galaxy 1197  
 1176 group containing the main deflector G1 is included in the count 1198  
 1177 and the case where we explicitly exclude the group. We find that 1199  
 1178 DES J0408–5354 lives in a significantly under-dense environment 1200  
 1179 whereas WGD 2038–4008 is in an environment that is closer to 1201  
 1180 mean density. As described in §8, we then apply the same obser- 1202  
 1181 vational constraints to the MS, with galaxies from the De Lucia 1203  
 1182 & Blaizot (2007) semi-analytical model, to compute  $\zeta_q$ , the 1204  
 1183 ratio of weighted galaxy counts of target to control fields. We obtain 1205

**Table 5.** Weighted galaxy count ratios  $\overline{\zeta}_q$  for DES J0408–5354 and WGD 2038–4008.

Weight $q$	45''	120''	45''	120''
	$i < 22.5$	$i < 22.5$	$i < 22.5$	$i < 22.5$
	DNF	DNF	BPZ	BPZ
DES J0408–5354 w/ group				
1	$0.643^{+0.071}_{-0.06}$	$0.495^{+0.029}_{-0.01}$	$0.643^{+0.071}_{-0.06}$	$0.495^{+0.039}_{-0.01}$
$z$	$0.7^{+0.207}_{-0.06}$	$0.497^{+0.029}_{-0.017}$	$0.689^{+0.223}_{-0.029}$	$0.532^{+0.042}_{-0.01}$
$1/r$	$0.658^{+0.095}_{-0.071}$	$0.517^{+0.048}_{-0.018}$	$0.644^{+0.108}_{-0.057}$	$0.517^{+0.056}_{-0.03}$
$z/r$	$0.749^{+0.204}_{-0.076}$	$0.449^{+0.033}_{-0.009}$	$0.757^{+0.193}_{-0.04}$	$0.461^{+0.038}_{-0.011}$
DES J0408–5354 w/o group				
1	$0.286^{+0.298}_{-0.209}$	$0.388^{+0.068}_{-0.068}$	$0.286^{+0.214}_{-0.209}$	$0.388^{+0.058}_{-0.068}$
$z$	$0.389^{+0.376}_{-0.288}$	$0.373^{+0.100}_{-0.106}$	$0.394^{+0.278}_{-0.287}$	$0.388^{+0.093}_{-0.10}$
$1/r$	$0.282^{+0.306}_{-0.207}$	$0.370^{+0.085}_{-0.070}$	$0.282^{+0.230}_{-0.207}$	$0.368^{+0.081}_{-0.069}$
$z/r$	$0.379^{+0.346}_{-0.278}$	$0.342^{+0.065}_{-0.079}$	$0.391^{+0.276}_{-0.286}$	$0.345^{+0.068}_{-0.076}$
WGD 2038–4008				
1	$0.90^{+0.20}_{-0.10}$	$1.169^{+0.039}_{-0.052}$	$0.833^{+0.556}_{-0.167}$	$1.184^{+0.066}_{-0.064}$
$z$	$1.066^{+0.191}_{-0.123}$	$1.286^{+0.061}_{-0.055}$	$0.919^{+0.084}_{-0.154}$	$1.237^{+0.078}_{-0.065}$
$1/r$	$0.943^{+0.494}_{-0.114}$	$1.288^{+0.046}_{-0.065}$	$0.881^{+0.059}_{-0.164}$	$1.296^{+0.060}_{-0.077}$
$z/r$	$1.187^{+0.150}_{-0.131}$	$1.362^{+0.083}_{-0.115}$	$0.999^{+0.144}_{-0.131}$	$1.278^{+0.123}_{-0.116}$

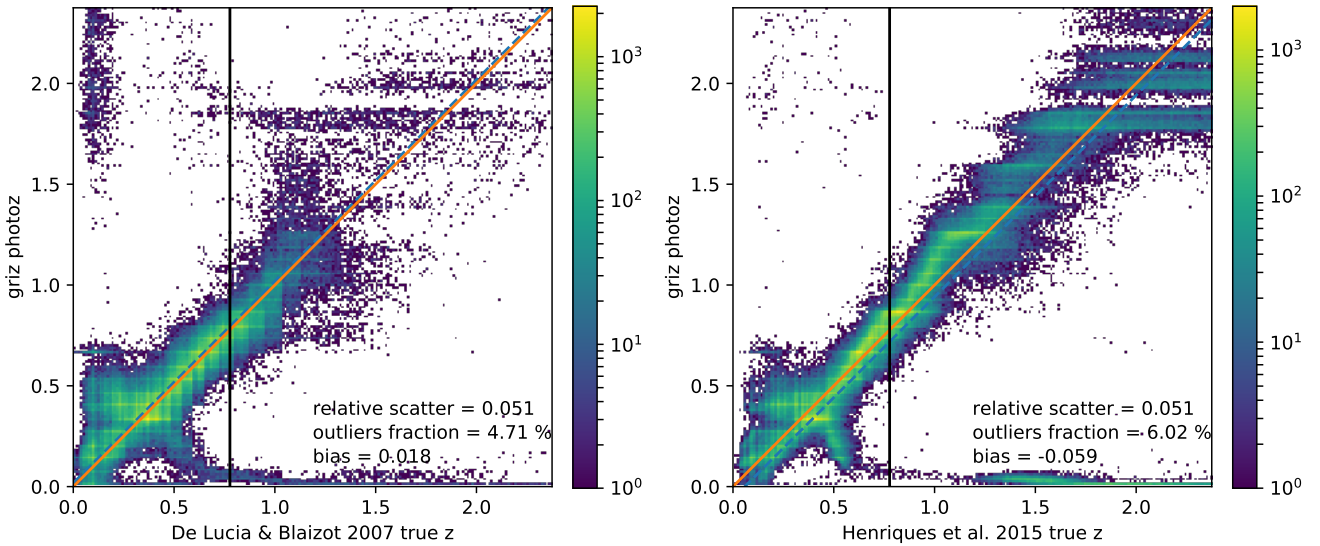


**Figure 15.** Comparison of catalogue versus photometric redshifts computed for a representative fraction of the MS galaxies painted over the dark matter halos, using the De Lucia & Blaizot (2007) (left) and Henriques et al. (2015) (right) semi-analytical galaxy models and resulting synthetic photometry. The photometric redshifts are computed using BPZ, with the errors on the photometry being representative of the DES measurement uncertainties for similar magnitudes. The limiting magnitude used is  $i < 22.5$  mag. The orange orange solid line marks the true  $z = \text{photoz}$  identity, and the blue dashed line marks the best linear fit. The plotting range extends to the redshift of DES J0408–5354. The vertical black line marks the redshift of WGD 2038–4008. For this lower redshifts, the scatter, fraction of outliers and bias become 0.051 (0.050 for Henriques et al. (2015)), 4.26% (3.08%) and 0.023 (–0.005), respectively.

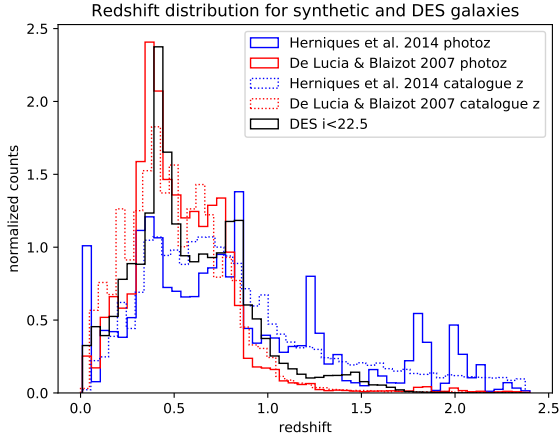


**Figure 16.** Histograms of the catalogue and BPZ-based photometric redshift distributions for a representative fraction of  $\sim 500000$  galaxies in the MS, using the semi-analytical models of De Lucia & Blaizot (2007) and Henriques et al. (2015). The BPZ-based photometric redshift distribution for a similar number of DES galaxies, down to the same  $i < 22.5$  mag limit, is also shown.

**Table 6.** Statistics of  $P(\kappa_{\text{ext}} | \zeta_1^{45''}, \zeta_{1/r}^{45''}, \zeta_1^{120''}, \zeta_{1/r}^{120''}, \gamma)$  as a function of  $\gamma$ , for the DES J0408–5354 and WGD 2038–4008 systems. We report the variation in the median and semi-difference of the 16th and 84th quantiles. The error bar around each  $\gamma$  constraint is 0.005. For WGD 2038–4008 the distributions for large  $\gamma$  are too noisy to report.

$\gamma$	DES J0408–5354		WGD 2038–4008	
	med $_{\kappa}$	$\sigma_{\kappa}$	med $_{\kappa}$	$\sigma_{\kappa}$
0.01	−0.053	0.025	−0.004	0.006
0.02	−0.052	0.025	−0.002	0.007
0.03	−0.049	0.026	0.002	0.008
0.04	−0.046	0.027	0.008	0.011
0.05	−0.041	0.029	0.016	0.017
0.06	−0.035	0.032	0.032	0.028
0.07	−0.028	0.035	0.056	0.038
0.08	−0.020	0.039	0.074	0.042
0.09	−0.009	0.043	0.101	0.046
0.10	0.002	0.048	0.128	0.054
0.11	0.018	0.054	...	...
0.12	0.032	0.060	...	...
0.13	0.046	0.067	...	...
0.14	0.067	0.075	...	...
0.15	0.088	0.083	...	...

1185  $P(\kappa_{\text{ext}})$ , the probability distribution of the external convergence  $\kappa_{\text{ext}}$ , 1244  
 1186 by selecting lines of sight from the MS that match the observed  $\zeta_q$  1245  
 1187 constraints. As expected from the significantly underdense field of 1246  
 1188 DES J0408–5354, the resulting fiducial  $P(\kappa_{\text{ext}})$  distributions are 1247  
 1189 tight (with width  $\approx 0.03$  in  $\kappa_{\text{ext}}$ ) and medians around  $\kappa_{\text{ext}} \sim -0.04$  1248  
 1190  $- -0.05$ . For the case excluding the group containing G1 from the 1249  
 1191 number counts, the median  $\kappa_{\text{ext}}$  decreases by  $\lesssim 0.01$ . The distribu- 1250

1192 tions for WGD 2038–4008 are much tighter, with width  $\sim 1\%$ . This 1193  
 1194 is expected due to the significantly lower source redshift ( $z_s = 0.777$  1195  
 1196 for WGD 2038–4008 vs.  $z_s = 2.375$  for DES J0408–5354), as there 1197  
 will be fewer structures along the line of sight to contribute to the 1198  
 convergence. 1199

## 1197 ACKNOWLEDGMENTS

1198 We thank the anonymous referee for their helpful comments.

1199 J.P. would like to thank Gourav Khullar for their help and 1200  
 1201 insightful discussions that helped improve the analysis in this paper. 1202  
 This work made use of computing resources and support provided 1203  
 by the Research Computing Center at the University of Chicago. J.P. 1204  
 is supported in part by the Kavli Institute for Cosmological Physics 1205  
 at the University of Chicago through grant NSF PHY-1125897 and 1206  
 an endowment from the Kavli Foundation and its founder Fred 1207  
 Kavli.

1208 AJS was supported by the National Aeronautics and Space 1209  
 Administration (NASA) through the Space Telescope Science In- 1210  
 stitute (STScI) grant HST-GO-15320. AJS was also supported by 1211  
 the Dissertation Year Fellowship from the University of California, 1212  
 Los Angeles (UCLA) graduate division.

1213 TA acknowledges support from Proyecto FONDECYT N: 1214  
 1190335.

1215 This work was supported by World Premier International Re- 1216  
 search Center Initiative (WPI Initiative), MEXT, Japan.

1217 CDF acknowledges support for this work from the National 1218  
 Science Foundation under Grant No. AST-1715611.

1219 SM acknowledges the funding from the European Research 1220  
 Council (ERC) under the EUs Horizon 2020 research and innovation 1221  
 program (COSMICLENS; grant agreement No. 787886).

1222 Funding for the DES Projects has been provided by the U.S. De- 1223  
 partment of Energy, the U.S. National Science Foundation, the Min- 1224  
 istry of Science and Education of Spain, the Science and Technol- 1225  
 ogy Facilities Council of the United Kingdom, the Higher Education 1226  
 Funding Council for England, the National Center for Supercomput- 1227  
 ing Applications at the University of Illinois at Urbana-Champaign, 1228  
 the Kavli Institute of Cosmological Physics at the University of 1229  
 Chicago, the Center for Cosmology and Astro-Particle Physics at 1230  
 the Ohio State University, the Mitchell Institute for Fundamental 1231  
 Physics and Astronomy at Texas A&M University, Financiadora 1232  
 de Estudos e Projetos, Fundação Carlos Chagas Filho de Amparo à 1233  
 Pesquisa do Estado do Rio de Janeiro, Conselho Nacional de Desen- 1234  
 volvimento Científico e Tecnológico and the Ministério da Ciência, 1235  
 Tecnologia e Inovação, the Deutsche Forschungsgemeinschaft and 1236  
 the Collaborating Institutions in the Dark Energy Survey.

1237 The Collaborating Institutions are Argonne National Labora- 1238  
 tory, the University of California at Santa Cruz, the University of 1239  
 Cambridge, Centro de Investigaciones Energéticas, Medioambien- 1240  
 tales y Tecnológicas-Madrid, the University of Chicago, Univer- 1241  
 sity College London, the DES-Brazil Consortium, the University 1242  
 of Edinburgh, the Eidgenössische Technische Hochschule (ETH) 1243  
 Zürich, Fermi National Accelerator Laboratory, the University of 1244  
 Illinois at Urbana-Champaign, the Institut de Ciències de l’Espai 1245  
 (IEEC/CSIC), the Institut de Física d’Altes Energies, Lawrence 1246  
 Berkeley National Laboratory, the Ludwig-Maximilians Universität 1247  
 München and the associated Excellence Cluster Universe, the Uni- 1248  
 versity of Michigan, the National Optical Astronomy Observatory, 1249  
 the University of Nottingham, The Ohio State University, the Uni- 1250  
 versity of Pennsylvania, the University of Portsmouth, SLAC Na-  
 tional Accelerator Laboratory, Stanford University, the University



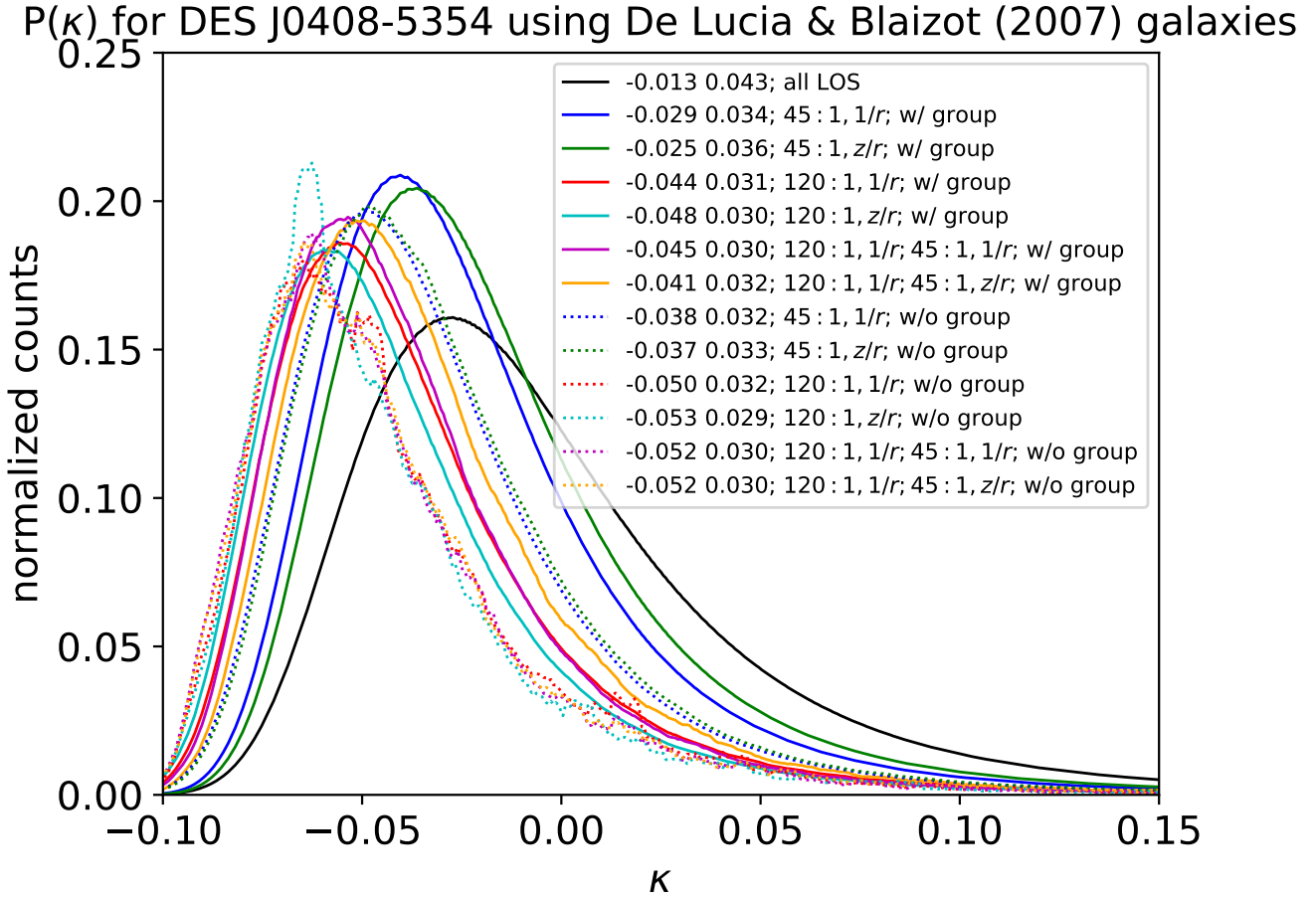


**Figure 17.** Histograms of smoothed  $\kappa_{\text{ext}}$  distributions for DES J0408–5354 for a variety of constraints, using the De Lucia & Blaizot (2007) semi-analytical galaxy models. “w/ group” and “w/o group” refer to the case when the member galaxies of the lens group are kept or not kept as part of the LOS, respectively. The first distribution shown is for the case when all LOS from MS are used, without constraints. The first two numbers in the legend are the median and the semi-difference between the 16th and the 84th percentiles of each distribution, respectively.

1251 of Sussex, Texas A&M University, and the OzDES Membership  
1252 Consortium.

1253 Based in part on observations at Cerro Tololo Inter-American  
1254 Observatory, National Optical Astronomy Observatory, which is oper-  
1255 ated by the Association of Universities for Research in Astronomy  
1256 (AURA) under a cooperative agreement with the National Science  
1257 Foundation.

1258 The DES data management system is supported by the National  
1259 Science Foundation under Grant Numbers AST-1138766  
1260 and AST-1536171. The DES participants from Spanish institu-  
1261 tions are partially supported by MINECO under grants AYA2015-  
1262 71825, ESP2015-88861, FPA2015-68048, SEV-2012-0234, SEV-  
1263 2016-0597, and MDM-2015-0509, some of which include ERDF  
1264 funds from the European Union. IFAE is partially funded by the  
1265 CERCA program of the Generalitat de Catalunya. Research leading  
1266 to these results has received funding from the European Research  
1267 Council under the European Union’s Seventh Framework Program  
1268 (FP7/2007-2013) including ERC grant agreements 240672, 291329,  
1269 and 306478. We acknowledge support from the Australian Research  
1270 Council Centre of Excellence for All-sky Astrophysics (CAAS-  
1271 TRO), through project number CE110001020.

1272 This manuscript has been authored by Fermi Research Al-

1273 liance, LLC under Contract No. DE-AC02-07CH11359 with the  
1274 U.S. Department of Energy, Office of Science, Office of High En-  
1275 ergy Physics. The United States Government retains and the pub-  
1276 lisher, by accepting the article for publication, acknowledges that  
1277 the United States Government retains a non-exclusive, paid-up, ir-  
1278 revocable, world-wide license to publish or reproduce the published  
1279 form of this manuscript, or allow others to do so, for United States  
1280 Government purposes.

1281 Based on observations obtained at the Gemini Observatory  
1282 (acquired through the Gemini Observatory Archive and processed  
1283 using the Gemini IRAF package), which is operated by the As-  
1284 sociation of Universities for Research in Astronomy, Inc., under a  
1285 cooperative agreement with the NSF on behalf of the Gemini part-  
1286 nership: the National Science Foundation (United States), National  
1287 Research Council (Canada), CONICYT (Chile), Ministerio de Cien-  
1288 cia, Tecnología e Innovación Productiva (Argentina), Ministério da  
1289 Ciência, Tecnologia e Inovação (Brazil), and Korea Astronomy and  
1290 Space Science Institute (Republic of Korea).

1291 This paper includes data gathered with the 6.5 meter Magellan  
1292 Telescopes located at Las Campanas Observatory, Chile.

1293 Based on observations collected at the European Southern Ob-  
1294 servatory under ESO programme 0102.A-0600(E).

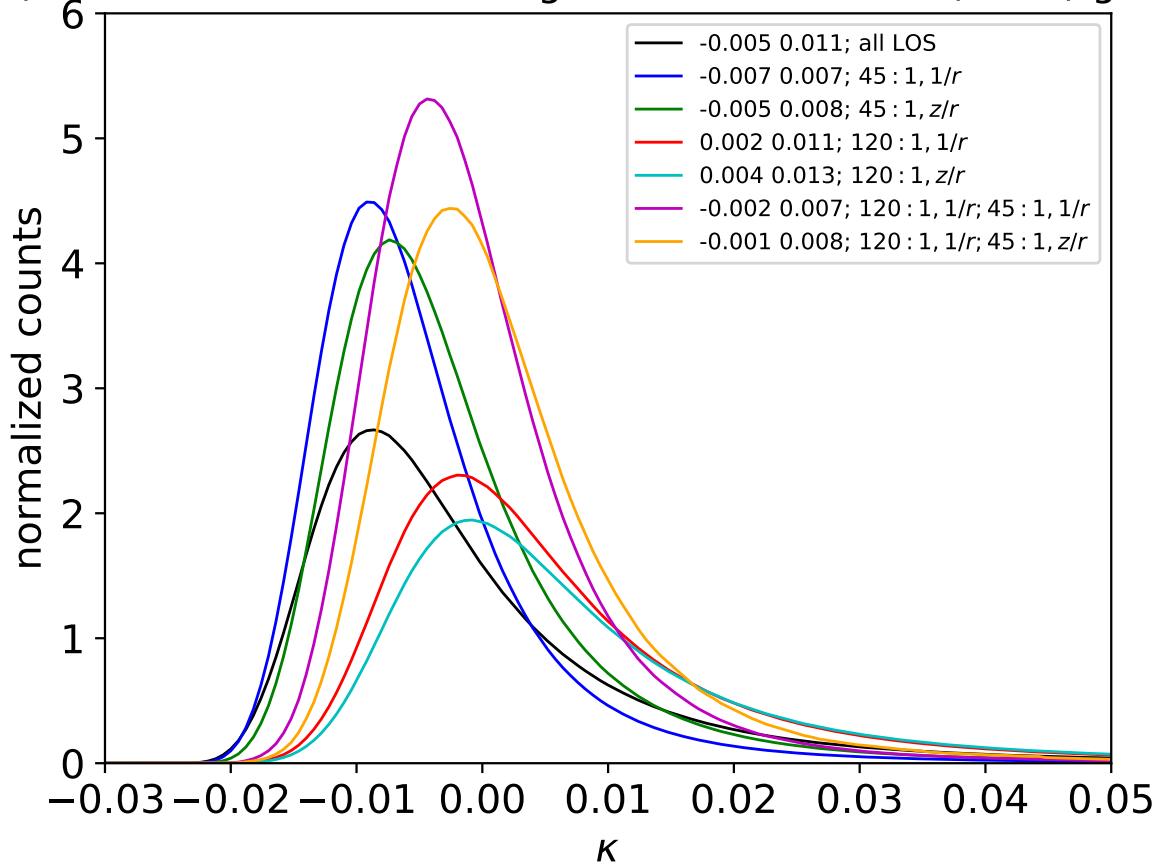
$P(\kappa)$  for WGD 2038-4008 using De Lucia & Blaizot (2007) galaxies

Figure 18. Similar to Figure 17, for the case of WGD 2038–4008.

- 1295 This work made extensive use of the Astropy library, a 1319  
 1296 community-developed core Python package for Astronomy ([As-](#) 1320  
 1297 [tropy Collaboration et al. 2013](#)).
- 1298 **REFERENCES**
- 1299 Abbott T. M. C., et al., 2018, [ApJS](#), 239, 18  
 1300 Agnello A., et al., 2018, [MNRAS](#), 479, 4345  
 1301 Ammons S. M., Wong K. C., Zabludoff A. I., Keeton C. R., 2014, [ApJ](#), 781,  
 1302 2  
 1303 Amorisco N. C., Evans N. W., 2012, [MNRAS](#), 424, 1899  
 1304 Andreon S., Hurn M. A., 2010, [MNRAS](#), 404, 1922  
 1305 Arnouts S., Cristiani S., Moscardini L., Matarrese S., Lucchin F., Fontana  
 1306 A., Giallongo E., 1999, [MNRAS](#), 310, 540  
 1307 Astropy Collaboration et al., 2013, [A&A](#), 558, A33  
 1308 Auger M. W., Treu T., Brewer B. J., Marshall P. J., 2010, [Monthly Notices](#)  
 1309 [of the Royal Astronomical Society: Letters](#), Volume 411, Issue 1, pp.  
 1310 L6-L10., 411, L6  
 1311 Beers T. C., Flynn K., Gebhardt K., 1990, [The Astronomical Journal](#), 100,  
 1312 32  
 1313 Benítez N., 2000, [ApJ](#), 536, 571  
 1314 Bertin E., Arnouts S., 1996, [Astronomy and Astrophysics Supplement Se-](#)  
 1315 [ries](#), 117, 393  
 1316 Birrer S., et al., 2019, [MNRAS](#), 484, 4726  
 1317 Bruzual G., Charlot S., 2003, [MNRAS](#), 344, 1000  
 1318 Chabrier G., 2003, [PASP](#), 115, 763  
 1319 Chen G. C. F., et al., 2019, [MNRAS](#), 490, 1743  
 1320 Collett T. E., et al., 2013, [MNRAS](#), 432, 679  
 1321 De Lucia G., Blaizot J., 2007, [MNRAS](#), 375, 2  
 1322 De Vicente J., Sánchez E., Sevilla-Noarbe I., 2016, [MNRAS](#), 459, 3078  
 1323 Desai S., et al., 2012, [The Astrophysical Journal](#), Volume 757, Issue 1,  
 1324 article id. 83, 22 pp. (2012)., 757  
 1325 Diehl H. T., et al., 2019, [J 10.2172/1596042](#)  
 1326 Dressler A., et al., 2011, [PASP](#), 123, 288  
 1327 Drlica-Wagner A., et al., 2018, [ApJS](#), 235, 33  
 1328 Fassnacht C. D., Koopmans L. V. E., Wong K. C., 2011, [MNRAS](#), 410, 2167  
 1329 Flaugher B., et al., 2015, [The Astronomical Journal](#), Volume 150, Issue 5,  
 1330 article id. 150, 43 pp. (2015)., 150  
 1331 Foreman-Mackey D., Hogg D. W., Lang D., Goodman J., 2013, [PASP](#), 125,  
 1332 306  
 1333 Goodman J., Weare J., 2010, [Communications in Applied Mathematics and](#)  
 1334 [Computational Science](#), Vol.~5, No.~1, p.~65-80, 2010, 5, 65  
 1335 Greene Z. S., et al., 2013, [ApJ](#), 768, 39  
 1336 Guérou A., et al., 2017, [A&A](#), 608, A5  
 1337 Hamilton A. J. S., Tegmark M., 2004, [MNRAS](#), 349, 115  
 1338 Henriques B. M. B., White S. D. M., Thomas P. A., Angulo R., Guo Q.,  
 1339 Lemson G., Springel V., Overzier R., 2015, [MNRAS](#), 451, 2663  
 1340 Heymans C., et al., 2012, [MNRAS](#), 427, 146  
 1341 Hilbert S., Hartlap J., White S. D. M., Schneider P., 2009, [A&A](#), 499, 31  
 1342 Hoyle B., et al., 2018, [MNRAS](#), 478, 592  
 1343 Ilbert O., et al., 2006, [A&A](#), 457, 841  
 1344 Koleva M., Prugniel P., Bouchard A., Wu Y., 2009, [A&A](#), 501, 1269  
 1345 Kogosov S. E., et al., 2011, [ApJ](#), 736, 146

- 1346 Kurtz M. J., Mink D. J., 1998, *Publications of the Astronomical Society of*  
1347 *the Pacific*, 110, 934
- 1348 Laporte C. F. P., Agnello A., Navarro J. F., 2019, *MNRAS*, 484, 245
- 1349 Lemson G., Virgo Consortium t., 2006, arXiv e-prints, [pp astro-ph/0608019](https://arxiv.org/abs/astro-ph/0608019)
- 1350 Lin H., et al., 2017, *ApJ*, 838, L15
- 1351 Martin N. F., Collins M. L. M., Longeard N., Tollerud E., 2018, *ApJ*, 859,  
1352 L5
- 1353 McCully C., Keeton C. R., Wong K. C., Zabludoff A. I., 2014, *MNRAS*,  
1354 443, 3631
- 1355 McCully C., Keeton C. R., Wong K. C., Zabludoff A. I., 2017, *ApJ*, 836,  
1356 141
- 1357 Morganson E., et al., 2018, *Publications of the Astronomical Society of the*  
1358 *Pacific*, 130, 074501
- 1359 Mosteller F., Tukey J. W., 1977, Data analysis and regression. A second  
1360 course in statistics. [http://adsabs.harvard.edu/abs/1977dars.](http://adsabs.harvard.edu/abs/1977dars.book.....M)  
1361 [book.....M](http://adsabs.harvard.edu/abs/1977dars.book.....M)
- 1362 Oemler A., Clardy K., Kelson D., Walth G., Villanueva E., 2017, COS-  
1363 MOS: Carnegie Observatories System for MultiObject Spectroscopy  
1364 (ascl:1705.001)
- 1365 Peng C. Y., Ho L. C., Impey C. D., Rix H.-W., 2010, *AJ*, 139, 2097
- 1366 Planck Collaboration et al., 2016, *A&A*, 596, A105
- 1367 Refsdal S., 1964, *Monthly Notices of the Royal Astronomical Society*, 128,  
1368 307
- 1369 Rusu C. E., et al., 2017, *MNRAS*, 467, 4220
- 1370 Rusu C. E., et al., 2019, arXiv e-prints,
- 1371 Rykoff E. S., et al., 2014, *The Astrophysical Journal*, 785, 104
- 1372 Salpeter E. E., 1955, *ApJ*, 121, 161
- 1373 Sánchez-Blázquez P., et al., 2006, *MNRAS*, 371, 703
- 1374 Shajib et al. 2019a, *MNRAS*, submitted
- 1375 Shajib A. J., et al., 2019b, *Monthly Notices of the Royal Astronomical*  
1376 *Society*, 483, 5649
- 1377 Sluse D., et al., 2017, *Monthly Notices of the Royal Astronomical Society*,  
1378 470, 4838
- 1379 Sluse D., et al., 2019, *MNRAS*, 490, 613
- 1380 Springel V., et al., 2005, *Nature*, 435, 629
- 1381 Suyu S. H., Marshall P. J., Auger M. W., Hilbert S., Blandford R. D.,  
1382 Koopmans L. V. E., 2010a, [j 10.1088/0004-637X/711/1/201.1](https://arxiv.org/abs/10.1088/0004-637X/711/1/201.1), 201
- 1383 Suyu S. H., Marshall P. J., Auger M. W., Hilbert S., Blandford R. D.,  
1384 Koopmans L. V. E., Fassnacht C. D., Treu T., 2010b, *The Astrophysical*  
1385 *Journal*, Volume 711, Issue 1, pp. 201–221 (2010), 711, 201
- 1386 Suyu S. H., Auger M. W., Hilbert S., Marshall P. J., Tewes M., Treu T.,  
1387 Fassnacht C. D., 2013, [j 10.1088/0004-637X/766/2/70.70](https://arxiv.org/abs/10.1088/0004-637X/766/2/70.70)
- 1388 Suyu S. H., et al., 2017, *MNRAS*, 468, 2590
- 1389 Swanson M. E. C., Tegmark M., Hamilton A. J. S., Hill J. C., 2008, *MNRAS*,  
1390 387, 1391
- 1391 Treu T., Koopmans L. V. E., 2002, *MNRAS*, 337, L6
- 1392 Treu T., Marshall P. J., 2016, *A&ARv*, 24, 11
- 1393 Treu T., et al., 2018, *MNRAS*, 481, 1041
- 1394 Vazdekis A., Sánchez-Blázquez P., Falcón-Barroso J., Cenarro A. J., Beasley  
1395 M. A., Cardiel N., Gorgas J., Peletier R. F., 2010, *MNRAS*, 404, 1639
- 1396 Wainer H., Thissen D., 1976, *Psychometrika*, 41, 9
- 1397 Walker M. G., Peñarrubia J., 2011, *ApJ*, 742, 20
- 1398 Wilman D. J., Balogh M. L., Bower R. G., Mulchaey J. S., Oemler A.,  
1399 Carlberg R. G., Morris S. L., Whitaker R. J., 2005, *MNRAS*, 358, 71
- 1400 Wilson M. L., Zabludoff A. I., Ammons S. M., Momcheva I. G., Williams  
1401 K. A., Keeton C. R., 2016, *ApJ*, 833, 194
- 1402 Wong K. C., et al., 2019, arXiv e-prints, [p. arXiv:1907.04869](https://arxiv.org/abs/1907.04869)
- 1403 Zahid H. J., Geller M. J., Fabricant D. G., Hwang H. S., 2016, *ApJ*, 832,  
1404 203
- 1410 <sup>3</sup>Department of Astronomy & Astrophysics, University of Chicago,  
1411 Chicago, IL 60637
- 1412 <sup>4</sup>Kavli Institute for Cosmological Physics, University of Chicago,  
1413 Chicago, IL 60637
- 1414 <sup>5</sup>DARK, Niels Bohr Institute, University of Copenhagen, Lyngbyvej  
1415 2, DK-2100 Copenhagen, Denmark
- 1416 <sup>6</sup>Department of Physics and Astronomy, PAB, 430 Portola Plaza,  
1417 Box 951547, Los Angeles, CA 90095-1547, USA
- 1418 <sup>7</sup>Institute of Cosmology & Gravitation, University of Portsmouth,  
1419 Portsmouth, PO1 3FX, UK
- 1420 <sup>8</sup>Kavli Institute for Particle Astrophysics and Cosmology, Stanford  
1421 University, 452 Lomita Mall, Stanford, CA 94305, USA
- 1422 <sup>9</sup>Departamento de Ciencias Físicas, Universidad Andres Bello Fer-  
1423 nandez Concha 700, Las Condes, Santiago, Chile
- 1424 <sup>10</sup>Millennium Institute of Astrophysics, Chile
- 1425 <sup>11</sup>Department of Physics, University of California Davis, 1 Shields  
1426 Avenue, Davis, CA 95616, USA
- 1427 <sup>12</sup>Laboratoire d’Astrophysique, Ecole Polytechnique Fédérale de  
1428 Lausanne (EPFL), Observatoire de Sauverny, CH-1290 Versoix,  
1429 Switzerland
- 1430 <sup>13</sup>STAR Institute, Quartier Agora - Allée du six Aout, 19c B-4000  
1431 Liège, Belgium <sup>14</sup>Kavli IPMU (WPI), UTIAS, The University of  
1432 Tokyo, Kashiwa, Chiba 277-8583, Japan
- 1433 <sup>15</sup> Departamento de Física Matemática, Instituto de Física, Univer-  
1434 sidade de São Paulo, CP 66318, São Paulo, SP, 05314-970, Brazil
- 1435 <sup>16</sup> Laboratório Interinstitucional de e-Astronomia - LIneA, Rua Gal.  
1436 José Cristino 77, Rio de Janeiro, RJ - 20921-400, Brazil
- 1437 <sup>17</sup> Instituto de Física Teórica UAM/CSIC, Universidad Autónoma  
1438 de Madrid, 28049 Madrid, Spain
- 1439 <sup>18</sup> CNRS, UMR 7095, Institut d’Astrophysique de Paris, F-75014,  
1440 Paris, France
- 1441 <sup>19</sup> Sorbonne Universités, UPMC Univ Paris 06, UMR 7095, Institut  
1442 d’Astrophysique de Paris, F-75014, Paris, France
- 1443 <sup>20</sup> Department of Physics and Astronomy, Pevensey Building, Uni-  
1444 versity of Sussex, Brighton, BN1 9QH, UK
- 1445 <sup>21</sup> Department of Physics & Astronomy, University College Lon-  
1446 don, Gower Street, London, WC1E 6BT, UK
- 1447 <sup>22</sup> Centro de Investigaciones Energéticas, Medioambientales y Tec-  
1448 nológicas (CIEMAT), Madrid, Spain
- 1449 <sup>23</sup> Department of Astronomy, University of Illinois at Urbana-  
1450 Champaign, 1002 W. Green Street, Urbana, IL 61801, USA
- 1451 <sup>24</sup> National Center for Supercomputing Applications, 1205 West  
1452 Clark St., Urbana, IL 61801, USA
- 1453 <sup>25</sup> Institut de Física d’Altes Energies (IFAE), The Barcelona Insti-  
1454 tute of Science and Technology, Campus UAB, 08193 Bellaterra  
1455 (Barcelona) Spain
- 1456 <sup>26</sup> Institut d’Estudis Espacials de Catalunya (IEEC), 08034  
1457 Barcelona, Spain
- 1458 <sup>27</sup> Institute of Space Sciences (ICE, CSIC), Campus UAB, Carrer  
1459 de Can Magrans, s/n, 08193 Barcelona, Spain
- 1460 <sup>28</sup> INAF-Osservatorio Astronomico di Trieste, via G. B. Tiepolo  
1461 11, I-34143 Trieste, Italy
- 1462 <sup>29</sup> Institute for Fundamental Physics of the Universe, Via Beirut 2,  
1463 34014 Trieste, Italy
- 1464 <sup>30</sup> Observatório Nacional, Rua Gal. José Cristino 77, Rio de Janeiro,  
1465 RJ - 20921-400, Brazil
- 1466 <sup>31</sup> Department of Physics, IIT Hyderabad, Kandi, Telangana  
1467 502285, India
- 1468 <sup>32</sup> Department of Astronomy/Steward Observatory, University of  
1469 Arizona, 933 North Cherry Avenue, Tucson, AZ 85721-0065, USA
- 1470 <sup>33</sup> Jet Propulsion Laboratory, California Institute of Technology,  
1471 4800 Oak Grove Dr., Pasadena, CA 91109, USA
- 1405 **AFFILIATIONS**
- 1406 <sup>1</sup>Fermi National Accelerator Laboratory, P. O. Box 500, Batavia, IL  
1407 60510, USA
- 1408 <sup>2</sup>National Astronomical Observatory of Japan, 2-21-1 Osawa, Mi-  
1409 taka, Tokyo 181-8588, Japan

- 1472 <sup>34</sup> Santa Cruz Institute for Particle Physics, Santa Cruz, CA 95064,  
 1473 USA  
 1474 <sup>35</sup> Department of Physics, Stanford University, 382 Via Pueblo Mall,  
 1475 Stanford, CA 94305, USA  
 1476 <sup>36</sup> Kavli Institute for Particle Astrophysics & Cosmology, P. O. Box  
 1477 2450, Stanford University, Stanford, CA 94305, USA  
 1478 <sup>37</sup> SLAC National Accelerator Laboratory, Menlo Park, CA 94025,  
 1479 USA  
 1480 <sup>38</sup> School of Mathematics and Physics, University of Queensland,  
 1481 Brisbane, QLD 4072, Australia  
 1482 <sup>39</sup> Center for Cosmology and Astro-Particle Physics, The Ohio State  
 1483 University, Columbus, OH 43210, USA  
 1484 <sup>40</sup> Department of Physics, The Ohio State University, Columbus,  
 1485 OH 43210, USA  
 1486 <sup>41</sup> Center for Astrophysics | Harvard & Smithsonian, 60 Garden  
 1487 Street, Cambridge, MA 02138, USA  
 1488 <sup>42</sup> Australian Astronomical Optics, Macquarie University, North  
 1489 Ryde, NSW 2113, Australia  
 1490 <sup>43</sup> Lowell Observatory, 1400 Mars Hill Rd, Flagstaff, AZ 86001,  
 1491 USA  
 1492 <sup>44</sup> George P. and Cynthia Woods Mitchell Institute for Fundamental  
 1493 Physics and Astronomy, and Department of Physics and Astronomy,  
 1494 Texas A&M University, College Station, TX 77843, USA  
 1495 <sup>45</sup> Department of Astrophysical Sciences, Princeton University,  
 1496 Peyton Hall, Princeton, NJ 08544, USA  
 1497 <sup>46</sup> Institució Catalana de Recerca i Estudis Avançats, E-08010  
 1498 Barcelona, Spain  
 1499 <sup>47</sup> Department of Physics, University of Michigan, Ann Arbor, MI  
 1500 48109, USA  
 1501 <sup>48</sup> School of Physics and Astronomy, University of Southampton,  
 1502 Southampton, SO17 1BJ, UK  
 1503 <sup>49</sup> Brandeis University, Physics Department, 415 South Street,  
 1504 Waltham MA 02453  
 1505 <sup>50</sup> Computer Science and Mathematics Division, Oak Ridge Na-  
 1506 tional Laboratory, Oak Ridge, TN 37831  
 1507 <sup>51</sup> Max Planck Institute for Extraterrestrial Physics, Giessenbach-  
 1508 strasse, 85748 Garching, Germany  
 1509 <sup>52</sup> Universitäts-Sternwarte, Fakultät für Physik, Ludwig-  
 1510 Maximilians Universität München, Scheinerstr. 1, 81679 München,  
 1511 Germany

1512 **APPENDIX A: PROPERTIES FOR ALL GALAXIES AND**  
 1513 **GALAXY GROUPS**

1514 We present the full sample of galaxies in the spectroscopic sample  
 1515 as well as the group membership of each identified group.

Table A1: Properties of all 199 galaxies in spectroscopic survey of the field of DES J0408–5354 and 54 galaxies in the spectroscopic survey of the field of WGD 2038–4008, arranged in order of decreasing flexion shift on the lens galaxy. The columns display, in order, the galaxy ID, coordinates (RA, DEC in degrees; ICRS), redshift  $z$ , DES MOF\_CM\_MAG\_CORRECTED  $i$ -band magnitudes (whenever possible), distances to the lensing galaxy and flexion shifts. Spectroscopic redshift uncertainties are about  $100 \text{ km s}^{-1}$ , or 0.00033 in redshift. Galaxies with bad MOF magnitudes are indicated with †; for these galaxies, we use MAG\_AUTO\_CORRECTED photometry and the corresponding stellar mass estimates from that photometric data. For the galaxy IDs, DES Y3 galaxies have 9-digit IDs, DES Y1 galaxies have 10-digit IDs, and MUSE galaxies were labeled with the prefix "MUSE" and sorted by ascending redshifts. Stellar masses and corresponding uncertainties were calculated using the Le PHARE galaxy template fitting code and DES Y3 photometry (see §3.3). Flexion shift and uncertainties are calculated following the method described in §6.1-6.1.1.

ID	RA (deg)	DEC (deg)	$z$	$i$ -band Mag	$\log_{10}(M_*)$ ( $\log_{10}(M_{\odot})$ )	$\Delta\theta$ (arcsec)	$\log_{10}(\Delta_{3\times\text{Zahid}})$ ( $\log_{10}(\text{arcsec})$ )	$\log_{10}(\Delta_{3\times\text{Auger}})$ ( $\log_{10}(\text{arcsec})$ )
DES J0408–5354								
488068102	62.090965	-53.901634	0.76866	20.096	$11.42^{+0.10}_{-0.12}$	6.4	$-2.21^{+0.25}_{-0.29}$	$-2.20^{+0.21}_{-0.22}$
488065185	62.095575	-53.898291	0.59441	21.867	$10.29^{+0.10}_{-0.17}$	12.4	$-3.95^{+0.42}_{-0.58}$	$-3.42^{+0.21}_{-0.24}$
488066144	62.090243	-53.903609	0.77069	22.015	$10.66^{+0.13}_{-0.17}$	13.4	$-4.07^{+0.38}_{-0.51}$	$-3.72^{+0.22}_{-0.24}$
488066768	62.092923	-53.900091	1.03197	23.682	$9.68^{+0.24}_{-0.25}$	5.4	$-4.93^{+0.63}_{-0.93}$	$-3.87^{+0.26}_{-0.27}$
488066462	62.083912	-53.903969	0.60048	22.304	$9.88^{+0.12}_{-0.19}$	20.2	$-5.24^{+0.52}_{-0.79}$	$-4.37^{+0.22}_{-0.25}$
MUSE6/488065214†	62.077898	-53.903878	0.59797	22.303	$10.37^{+0.11}_{-0.16}$	30.2	$-5.02^{+0.41}_{-0.56}$	$-4.53^{+0.21}_{-0.23}$
488070148	62.084648	-53.885204	0.27247	18.309	$10.99^{+0.04}_{-0.04}$	54.3	$-4.81^{+0.31}_{-0.37}$	$-4.61^{+0.20}_{-0.20}$
488066886	62.090541	-53.904725	0.77568	22.925	$9.91^{+0.16}_{-0.30}$	17.4	$-5.46^{+0.53}_{-0.90}$	$-4.61^{+0.23}_{-0.30}$
488070807	62.072770	-53.910296	0.59811	19.975	$11.27^{+0.05}_{-0.06}$	53.0	$-4.69^{+0.25}_{-0.30}$	$-4.61^{+0.20}_{-0.21}$
MUSE8/488067782	62.103108	-53.897861	0.59832	22.100	$10.11^{+0.13}_{-0.20}$	27.9	$-5.29^{+0.48}_{-0.71}$	$-4.62^{+0.22}_{-0.25}$
488071104	62.077670	-53.913521	0.29469	18.555	$11.05^{+0.04}_{-0.04}$	56.0	$-4.80^{+0.30}_{-0.36}$	$-4.62^{+0.20}_{-0.20}$
488070774	62.075134	-53.912907	0.29368	18.519	$11.01^{+0.04}_{-0.04}$	57.0	$-4.87^{+0.30}_{-0.37}$	$-4.67^{+0.20}_{-0.20}$
MUSE15/488066060†	62.080992	-53.904565	0.76785	22.762	$10.44^{+0.12}_{-0.18}$	26.1	$-5.19^{+0.40}_{-0.55}$	$-4.74^{+0.22}_{-0.24}$
488066584	62.071692	-53.906245	0.59727	21.426	$10.69^{+0.04}_{-0.03}$	45.8	$-5.18^{+0.35}_{-0.45}$	$-4.84^{+0.20}_{-0.20}$
MUSE12/488067196	62.093482	-53.905711	0.64363	23.311	$9.18^{+0.22}_{-0.28}$	21.9	$-6.60^{+0.65}_{-1.05}$	$-5.10^{+0.25}_{-0.29}$
MUSE10/488070958	62.085862	-53.910180	0.60029	22.304	$10.01^{+0.14}_{-0.22}$	38.3	$-5.86^{+0.50}_{-0.77}$	$-5.10^{+0.22}_{-0.26}$
489523481	62.078380	-53.881917	0.59451	19.918	$11.04^{+0.07}_{-0.18}$	69.6	$-5.31^{+0.30}_{-0.43}$	$-5.13^{+0.21}_{-0.24}$
MUSE9/488069251†	62.085632	-53.891330	0.59906	23.333	$9.49^{+0.26}_{-0.35}$	32.4	$-6.48^{+0.67}_{-1.12}$	$-5.26^{+0.27}_{-0.33}$
488070002	62.070997	-53.882405	0.37961	20.614	$10.39^{+0.05}_{-0.06}$	75.2	$-6.02^{+0.39}_{-0.51}$	$-5.54^{+0.20}_{-0.20}$
488070966	62.067875	-53.910488	0.59977	21.729	$10.11^{+0.15}_{-0.19}$	61.2	$-6.32^{+0.49}_{-0.70}$	$-5.65^{+0.23}_{-0.25}$
488067363	62.134647	-53.901754	0.59479	21.047	$10.86^{+0.05}_{-0.05}$	94.1	$-5.92^{+0.33}_{-0.41}$	$-5.66^{+0.20}_{-0.20}$
MUSE14/488070770	62.099785	-53.908977	0.76669	23.533	$9.85^{+0.21}_{-0.28}$	38.3	$-6.56^{+0.58}_{-0.89}$	$-5.66^{+0.24}_{-0.29}$
488070443	62.101056	-53.907011	1.17764	21.911	$11.01^{+0.34}_{-0.32}$	34.2	$-5.88^{+0.48}_{-0.55}$	$-5.68^{+0.31}_{-0.31}$
488071406	62.054830	-53.913785	0.44241	20.276	$10.58^{+0.06}_{-0.07}$	90.5	$-6.08^{+0.37}_{-0.48}$	$-5.69^{+0.20}_{-0.21}$
405340030	62.118966	-53.880474	0.57772	20.663	$10.71^{+0.07}_{-0.18}$	92.5	$-6.06^{+0.36}_{-0.50}$	$-5.73^{+0.21}_{-0.24}$
488071428	62.068708	-53.913477	0.59843	21.581	$10.15^{+0.12}_{-0.17}$	67.2	$-6.36^{+0.46}_{-0.66}$	$-5.73^{+0.22}_{-0.24}$
488072005	62.068079	-53.917283	0.54122	21.624	$10.32^{+0.10}_{-0.18}$	78.5	$-6.27^{+0.41}_{-0.58}$	$-5.76^{+0.21}_{-0.24}$

MUSE19/488068048	62.088268	-53.890642	0.91504	23.065	$9.92^{+0.30}_{-0.29}$	33.6	$-6.64^{+0.64}_{-0.87}$	$-5.80^{+0.29}_{-0.29}$
488067814	62.109798	-53.896296	0.78734	22.001	$9.90^{+0.20}_{-0.24}$	43.1	$-6.68^{+0.56}_{-0.83}$	$-5.83^{+0.24}_{-0.27}$
MUSE22/488065663	62.090044	-53.891845	1.09148	23.419	$10.22^{+0.28}_{-0.27}$	29.0	$-6.40^{+0.59}_{-0.75}$	$-5.83^{+0.28}_{-0.29}$
488072697	62.061177	-53.921532	0.27257	19.767	$10.33^{+0.04}_{-0.05}$	99.6	$-6.37^{+0.40}_{-0.52}$	$-5.87^{+0.20}_{-0.20}$
MUSE20/488065095	62.091419	-53.890585	0.94698	23.108	$9.91^{+0.34}_{-0.26}$	33.6	$-6.74^{+0.69}_{-0.85}$	$-5.89^{+0.31}_{-0.28}$
488070825	62.106067	-53.909453	0.77562	21.908	$9.93^{+0.21}_{-0.26}$	47.8	$-6.74^{+0.56}_{-0.84}$	$-5.91^{+0.24}_{-0.28}$
488066235	62.023367	-53.910705	0.57025	19.314	$11.28^{+0.06}_{-0.17}$	147.4	$-6.00^{+0.26}_{-0.36}$	$-5.92^{+0.20}_{-0.24}$
489523492	62.067524	-53.881235	0.78001	20.704	$10.92^{+0.12}_{-0.18}$	82.9	$-6.17^{+0.34}_{-0.46}$	$-5.93^{+0.22}_{-0.24}$
489521356	62.083229	-53.863995	0.57765	20.123	$11.02^{+0.07}_{-0.17}$	130.1	$-6.14^{+0.31}_{-0.42}$	$-5.95^{+0.21}_{-0.24}$
488070625	62.057786	-53.908625	0.93778	21.744	$11.27^{+0.05}_{-0.07}$	76.0	$-6.04^{+0.26}_{-0.31}$	$-5.96^{+0.20}_{-0.21}$
488073290	62.106161	-53.923866	0.57035	20.933	$10.36^{+0.07}_{-0.12}$	92.5	$-6.47^{+0.40}_{-0.54}$	$-5.98^{+0.21}_{-0.22}$
488074578	62.144676	-53.934498	0.27176	18.315	$11.11^{+0.05}_{-0.12}$	169.6	$-6.16^{+0.29}_{-0.37}$	$-6.01^{+0.20}_{-0.22}$
488070449	62.025309	-53.910519	0.42954	19.664	$10.95^{+0.05}_{-0.07}$	143.3	$-6.24^{+0.32}_{-0.39}$	$-6.01^{+0.20}_{-0.21}$
488073735	62.139479	-53.928501	0.42858	19.429	$10.95^{+0.05}_{-0.07}$	146.4	$-6.27^{+0.32}_{-0.39}$	$-6.04^{+0.20}_{-0.21}$
488072433	62.093088	-53.919040	0.30909	21.573	$9.45^{+0.09}_{-0.11}$	69.2	$-7.31^{+0.58}_{-0.88}$	$-6.06^{+0.21}_{-0.22}$
489522058	62.078867	-53.872863	0.09083	18.298	$9.90^{+0.04}_{-0.04}$	100.3	$-6.92^{+0.49}_{-0.68}$	$-6.07^{+0.20}_{-0.20}$
488066362	62.052505	-53.883271	0.94641	21.835	$11.50^{+0.03}_{-0.03}$	100.2	$-6.14^{+0.21}_{-0.24}$	$-6.17^{+0.20}_{-0.20}$
488072414	62.148320	-53.919275	0.42744	20.060	$10.70^{+0.10}_{-0.07}$	141.2	$-6.50^{+0.37}_{-0.45}$	$-6.17^{+0.21}_{-0.21}$
488072532	62.024006	-53.921066	0.44478	19.809	$10.87^{+0.06}_{-0.08}$	160.1	$-6.49^{+0.33}_{-0.42}$	$-6.23^{+0.20}_{-0.21}$
488067185	62.020675	-53.907526	0.30566	19.692	$10.58^{+0.04}_{-0.05}$	150.5	$-6.64^{+0.37}_{-0.47}$	$-6.25^{+0.20}_{-0.20}$
488076699	62.096336	-53.944173	0.30792	19.259	$10.67^{+0.05}_{-0.07}$	159.9	$-6.62^{+0.36}_{-0.46}$	$-6.27^{+0.20}_{-0.21}$
MUSE21/488071544	62.087179	-53.913732	0.98821	22.458	$10.21^{+0.23}_{-0.32}$	50.3	$-6.88^{+0.53}_{-0.81}$	$-6.30^{+0.25}_{-0.31}$
488067820	62.129495	-53.889946	0.25191	21.049	$9.53^{+0.09}_{-0.11}$	90.3	$-7.49^{+0.57}_{-0.86}$	$-6.30^{+0.21}_{-0.22}$
MUSE3/488069277	62.103394	-53.889095	0.40779	23.661	$8.52^{+0.27}_{-0.32}$	47.6	$-8.40^{+0.43}_{-0.53}$	$-6.31^{+0.27}_{-0.31}$
488068050	62.133568	-53.897135	0.46159	20.744	$9.75^{+0.09}_{-0.10}$	92.1	$-7.31^{+0.53}_{-0.77}$	$-6.32^{+0.21}_{-0.22}$
MUSE26/488070824	62.095831	-53.909607	1.25062	22.383	$10.49^{+0.19}_{-0.22}$	36.8	$-6.76^{+0.43}_{-0.57}$	$-6.33^{+0.24}_{-0.26}$
488071089	62.049904	-53.911313	0.30581	21.203	$9.64^{+0.10}_{-0.12}$	95.3	$-7.43^{+0.56}_{-0.83}$	$-6.34^{+0.21}_{-0.22}$
488065930	62.137580	-53.888784	0.57825	21.113	$10.08^{+0.11}_{-0.12}$	107.7	$-7.08^{+0.47}_{-0.65}$	$-6.38^{+0.21}_{-0.22}$
488069700	62.083413	-53.882657	0.27216	22.456	$8.80^{+0.16}_{-0.21}$	63.8	$-8.23^{+0.50}_{-0.72}$	$-6.39^{+0.23}_{-0.25}$
489521068	62.092960	-53.861224	0.27153	20.306	$10.21^{+0.07}_{-0.12}$	139.3	$-6.98^{+0.43}_{-0.60}$	$-6.40^{+0.20}_{-0.22}$
489521448	62.103449	-53.864717	0.43985	20.616	$10.23^{+0.10}_{-0.15}$	129.6	$-6.97^{+0.44}_{-0.62}$	$-6.41^{+0.21}_{-0.23}$
488072561	62.053602	-53.920059	0.62960	21.216	$10.16^{+0.09}_{-0.11}$	106.6	$-7.04^{+0.45}_{-0.61}$	$-6.41^{+0.21}_{-0.22}$
488074608	62.140970	-53.931443	0.43054	20.683	$10.53^{+0.05}_{-0.05}$	156.2	$-6.84^{+0.38}_{-0.48}$	$-6.43^{+0.20}_{-0.20}$
488070133	62.169886	-53.887360	0.59607	20.158	$10.84^{+0.14}_{-0.12}$	174.5	$-6.74^{+0.36}_{-0.44}$	$-6.47^{+0.22}_{-0.22}$
488073762	62.131777	-53.926465	0.42904	21.665	$10.11^{+0.08}_{-0.14}$	129.8	$-7.15^{+0.45}_{-0.65}$	$-6.49^{+0.21}_{-0.23}$
488073021	62.080583	-53.922670	0.30741	21.184	$9.21^{+0.08}_{-0.09}$	84.6	$-7.96^{+0.59}_{-0.89}$	$-6.49^{+0.21}_{-0.21}$
489522199	62.081990	-53.870601	0.39730	21.866	$9.72^{+0.14}_{-0.24}$	106.9	$-7.51^{+0.56}_{-0.90}$	$-6.50^{+0.22}_{-0.27}$
488072604	62.073251	-53.920150	0.77290	22.129	$10.07^{+0.16}_{-0.19}$	81.5	$-7.20^{+0.50}_{-0.71}$	$-6.50^{+0.23}_{-0.25}$
489521528	62.088464	-53.864945	0.24688	20.718	$9.83^{+0.09}_{-0.08}$	125.9	$-7.43^{+0.52}_{-0.73}$	$-6.52^{+0.21}_{-0.21}$
488069699	62.097258	-53.886716	0.92560	22.617	$9.67^{+0.22}_{-0.23}$	49.6	$-7.58^{+0.61}_{-0.91}$	$-6.52^{+0.25}_{-0.27}$
488070602	62.030809	-53.908820	0.26729	20.096	$9.86^{+0.06}_{-0.06}$	130.4	$-7.45^{+0.50}_{-0.71}$	$-6.56^{+0.20}_{-0.21}$

489523576	62.050079	-53.881679	0.94745	22.694	11.08 <sup>+0.07</sup> <sub>-0.08</sub>	107.8	-6.73 <sup>+0.29</sup> <sub>-0.36</sub>	-6.57 <sup>+0.20</sup> <sub>-0.21</sub>
MUSE24/488069253	62.104998	-53.902502	1.14831	23.055	9.55 <sup>+0.26</sup> <sub>-0.28</sub>	32.3	-7.76 <sup>+0.66</sup> <sub>-1.01</sub>	-6.59 <sup>+0.27</sup> <sub>-0.29</sub>
488074678	62.146922	-53.934938	0.27044	19.713	10.34 <sup>+0.04</sup> <sub>-0.04</sub>	174.0	-7.09 <sup>+0.40</sup> <sub>-0.52</sub>	-6.59 <sup>+0.20</sup> <sub>-0.20</sub>
488074840	62.107311	-53.932685	0.73105	21.409	10.54 <sup>+0.09</sup> <sub>-0.11</sub>	123.4	-7.00 <sup>+0.38</sup> <sub>-0.50</sub>	-6.59 <sup>+0.21</sup> <sub>-0.22</sub>
488071415	62.113750	-53.913080	0.74981	22.287	9.54 <sup>+0.18</sup> <sub>-0.15</sub>	68.6	-7.78 <sup>+0.61</sup> <sub>-0.89</sub>	-6.60 <sup>+0.24</sup> <sub>-0.23</sub>
488070947	62.158048	-53.912350	0.76818	18.274	11.02 <sup>+0.10</sup> <sub>-0.14</sub>	150.3	-6.80 <sup>+0.32</sup> <sub>-0.41</sub>	-6.60 <sup>+0.21</sup> <sub>-0.23</sub>
488067669	62.135908	-53.895219	0.46127	22.257	9.47 <sup>+0.18</sup> <sub>-0.28</sub>	98.0	-7.85 <sup>+0.62</sup> <sub>-1.03</sub>	-6.61 <sup>+0.23</sup> <sub>-0.29</sub>
488071411	62.045447	-53.913359	0.30642	21.438	9.44 <sup>+0.10</sup> <sub>-0.11</sub>	107.0	-7.89 <sup>+0.58</sup> <sub>-0.89</sub>	-6.63 <sup>+0.21</sup> <sub>-0.22</sub>
489523301	62.097716	-53.879281	0.27278	22.768	8.75 <sup>+0.16</sup> <sub>-0.22</sub>	75.8	-8.53 <sup>+0.46</sup> <sub>-0.67</sub>	-6.65 <sup>+0.23</sup> <sub>-0.26</sub>
488072531	62.108813	-53.919489	0.75070	22.550	9.73 <sup>+0.17</sup> <sub>-0.20</sub>	80.6	-7.68 <sup>+0.57</sup> <sub>-0.86</sub>	-6.67 <sup>+0.23</sup> <sub>-0.25</sub>
488070816	62.035444	-53.909470	0.60004	22.347	9.92 <sup>+0.23</sup> <sub>-0.24</sub>	121.6	-7.52 <sup>+0.58</sup> <sub>-0.82</sub>	-6.68 <sup>+0.25</sup> <sub>-0.27</sub>
404169047	62.136795	-53.861686	0.16020	18.916	10.04 <sup>+0.04</sup> <sub>-0.04</sub>	169.1	-7.42 <sup>+0.46</sup> <sub>-0.63</sub>	-6.69 <sup>+0.20</sup> <sub>-0.20</sub>
488070607	62.037079	-53.908383	0.59964	22.356	9.76 <sup>+0.18</sup> <sub>-0.21</sub>	117.2	-7.72 <sup>+0.57</sup> <sub>-0.85</sub>	-6.74 <sup>+0.23</sup> <sub>-0.26</sub>
488067357	62.163804	-53.896708	0.72762	21.625	10.72 <sup>+0.06</sup> <sub>-0.11</sub>	156.1	-7.10 <sup>+0.36</sup> <sub>-0.46</sub>	-6.77 <sup>+0.20</sup> <sub>-0.22</sub>
404169634	62.112378	-53.871809	0.80252	21.675	10.34 <sup>+0.15</sup> <sub>-0.37</sub>	111.3	-7.28 <sup>+0.43</sup> <sub>-0.72</sub>	-6.79 <sup>+0.22</sup> <sub>-0.34</sub>
488074345	62.179533	-53.930268	0.43930	20.522	10.58 <sup>+0.06</sup> <sub>-0.12</sub>	218.3	-7.23 <sup>+0.37</sup> <sub>-0.50</sub>	-6.84 <sup>+0.20</sup> <sub>-0.22</sub>
489521853	62.084697	-53.867583	0.27148	21.675	9.27 <sup>+0.12</sup> <sub>-0.13</sub>	116.9	-8.25 <sup>+0.60</sup> <sub>-0.92</sub>	-6.84 <sup>+0.21</sup> <sub>-0.22</sub>
488078736	62.114845	-53.953040	0.42826	21.346	10.35 <sup>+0.07</sup> <sub>-0.09</sub>	198.2	-7.36 <sup>+0.40</sup> <sub>-0.53</sub>	-6.86 <sup>+0.21</sup> <sub>-0.21</sub>
488066250	62.017973	-53.905064	0.57028	21.306	10.05 <sup>+0.10</sup> <sub>-0.14</sub>	154.8	-7.59 <sup>+0.47</sup> <sub>-0.68</sub>	-6.87 <sup>+0.21</sup> <sub>-0.23</sub>
488069992	62.129682	-53.882696	0.23970	21.880	8.93 <sup>+0.10</sup> <sub>-0.12</sub>	103.8	-8.63 <sup>+0.53</sup> <sub>-0.78</sub>	-6.91 <sup>+0.21</sup> <sub>-0.22</sub>
488074838	62.144448	-53.932510	0.50871	21.484	9.97 <sup>+0.09</sup> <sub>-0.13</sub>	164.1	-7.75 <sup>+0.49</sup> <sub>-0.70</sub>	-6.96 <sup>+0.21</sup> <sub>-0.22</sub>
488078018	62.078114	-53.949484	0.51766	21.911	10.14 <sup>+0.09</sup> <sub>-0.17</sub>	180.4	-7.60 <sup>+0.45</sup> <sub>-0.67</sub>	-6.96 <sup>+0.21</sup> <sub>-0.24</sub>
488073172	62.142324	-53.923373	0.39342	21.554	9.52 <sup>+0.12</sup> <sub>-0.12</sub>	138.8	-8.18 <sup>+0.58</sup> <sub>-0.87</sub>	-6.98 <sup>+0.21</sup> <sub>-0.22</sub>
488077424	62.142854	-53.946644	0.39071	21.170	10.14 <sup>+0.07</sup> <sub>-0.09</sub>	201.7	-7.65 <sup>+0.44</sup> <sub>-0.60</sub>	-7.01 <sup>+0.21</sup> <sub>-0.21</sub>
488077861	62.077259	-53.948516	0.51744	21.566	10.04 <sup>+0.10</sup> <sub>-0.12</sub>	177.3	-7.75 <sup>+0.48</sup> <sub>-0.66</sub>	-7.01 <sup>+0.21</sup> <sub>-0.22</sub>
488075668	62.133767	-53.937477	0.42807	20.447	9.77 <sup>+0.07</sup> <sub>-0.06</sub>	163.6	-8.01 <sup>+0.52</sup> <sub>-0.71</sub>	-7.04 <sup>+0.21</sup> <sub>-0.21</sub>
488067945	62.019121	-53.902892	0.57171	21.720	9.77 <sup>+0.10</sup> <sub>-0.13</sub>	151.6	-8.02 <sup>+0.53</sup> <sub>-0.79</sub>	-7.04 <sup>+0.21</sup> <sub>-0.23</sub>
488072443	62.054344	-53.919213	0.27226	22.046	8.75 <sup>+0.14</sup> <sub>-0.13</sub>	103.4	-8.94 <sup>+0.45</sup> <sub>-0.58</sub>	-7.06 <sup>+0.22</sup> <sub>-0.22</sub>
488068654	62.143374	-53.894424	0.81351	22.007	10.04 <sup>+0.19</sup> <sub>-0.23</sub>	114.0	-7.79 <sup>+0.53</sup> <sub>-0.77</sub>	-7.06 <sup>+0.24</sup> <sub>-0.27</sub>
488071272	62.133772	-53.912201	0.15809	22.207	8.60 <sup>+0.13</sup> <sub>-0.16</sub>	102.1	-9.09 <sup>+0.29</sup> <sub>-0.36</sub>	-7.07 <sup>+0.22</sup> <sub>-0.23</sub>
488072984	62.146444	-53.921724	0.60815	22.144	9.68 <sup>+0.13</sup> <sub>-0.18</sub>	142.5	-8.13 <sup>+0.56</sup> <sub>-0.86</sub>	-7.08 <sup>+0.22</sup> <sub>-0.24</sub>
488068672	62.140255	-53.894233	0.16682	21.453	8.67 <sup>+0.13</sup> <sub>-0.14</sub>	107.7	-9.04 <sup>+0.37</sup> <sub>-0.47</sub>	-7.09 <sup>+0.22</sup> <sub>-0.23</sub>
488073629	62.125366	-53.926127	0.63364	22.258	9.43 <sup>+0.16</sup> <sub>-0.16</sub>	120.1	-8.38 <sup>+0.61</sup> <sub>-0.92</sub>	-7.10 <sup>+0.23</sup> <sub>-0.23</sub>
488073466	62.165107	-53.925645	0.93736	20.916	11.24 <sup>+0.05</sup> <sub>-0.07</sub>	183.5	-7.21 <sup>+0.26</sup> <sub>-0.31</sub>	-7.12 <sup>+0.20</sup> <sub>-0.21</sub>
488073766	62.050530	-53.926881	0.75824	22.336	9.92 <sup>+0.21</sup> <sub>-0.34</sub>	128.8	-8.00 <sup>+0.57</sup> <sub>-0.95</sub>	-7.17 <sup>+0.25</sup> <sub>-0.33</sub>
488070459	62.171977	-53.907068	0.37773	21.361	9.65 <sup>+0.11</sup> <sub>-0.12</sub>	174.9	-8.25 <sup>+0.56</sup> <sub>-0.83</sub>	-7.17 <sup>+0.21</sup> <sub>-0.22</sub>
488070459	62.171977	-53.907068	0.37779	21.361	9.65 <sup>+0.11</sup> <sub>-0.12</sub>	174.9	-8.25 <sup>+0.56</sup> <sub>-0.83</sub>	-7.17 <sup>+0.21</sup> <sub>-0.22</sub>
488072024	62.037238	-53.917791	0.37796	22.807	9.08 <sup>+0.18</sup> <sub>-0.26</sub>	129.9	-8.78 <sup>+0.62</sup> <sub>-1.01</sub>	-7.19 <sup>+0.24</sup> <sub>-0.28</sub>
488070460	62.171213	-53.906968	0.79720	22.595	10.56 <sup>+0.08</sup> <sub>-0.08</sub>	173.2	-7.60 <sup>+0.38</sup> <sub>-0.48</sub>	-7.19 <sup>+0.21</sup> <sub>-0.21</sub>
488072618	62.142800	-53.919871	0.77739	22.398	10.00 <sup>+0.17</sup> <sub>-0.35</sub>	132.3	-7.96 <sup>+0.52</sup> <sub>-0.93</sub>	-7.19 <sup>+0.23</sup> <sub>-0.33</sub>
488070460	62.171213	-53.906968	0.79737	22.595	10.56 <sup>+0.08</sup> <sub>-0.08</sub>	173.2	-7.60 <sup>+0.38</sup> <sub>-0.48</sub>	-7.19 <sup>+0.21</sup> <sub>-0.21</sub>

488074030	62.163437	-53.927404	0.46567	21.400	9.79 <sup>+0.10</sup> <sub>-0.11</sub>	183.8	-8.16 <sup>+0.53</sup> <sub>-0.76</sub>	-7.20 <sup>+0.21</sup> <sub>-0.22</sub>
488070027	62.154997	-53.888704	0.81379	22.887	10.25 <sup>+0.18</sup> <sub>-0.26</sub>	142.8	-7.74 <sup>+0.49</sup> <sub>-0.73</sub>	-7.20 <sup>+0.24</sup> <sub>-0.28</sub>
404169734	62.125315	-53.873569	0.76243	22.755	9.75 <sup>+0.23</sup> <sub>-0.30</sub>	120.3	-8.20 <sup>+0.61</sup> <sub>-0.96</sub>	-7.21 <sup>+0.26</sup> <sub>-0.30</sub>
488075485	62.112254	-53.935970	0.29471	22.103	9.08 <sup>+0.12</sup> <sub>-0.14</sub>	137.9	-8.80 <sup>+0.58</sup> <sub>-0.89</sub>	-7.21 <sup>+0.22</sup> <sub>-0.23</sub>
404169375	62.133682	-53.867494	0.16039	20.977	9.07 <sup>+0.11</sup> <sub>-0.12</sub>	148.4	-8.82 <sup>+0.58</sup> <sub>-0.88</sub>	-7.22 <sup>+0.21</sup> <sub>-0.22</sub>
MUSE25/488070944	62.098868	-53.909951	1.25002	23.508	9.42 <sup>+0.19</sup> <sub>-0.26</sub>	40.4	-8.50 <sup>+0.63</sup> <sub>-1.02</sub>	-7.22 <sup>+0.24</sup> <sub>-0.28</sub>
488067796	62.025664	-53.892284	0.91979	21.768	10.53 <sup>+0.10</sup> <sub>-0.31</sub>	140.1	-7.65 <sup>+0.39</sup> <sub>-0.63</sub>	-7.24 <sup>+0.21</sup> <sub>-0.31</sub>
488073160	62.043694	-53.923652	0.91456	22.098	10.36 <sup>+0.18</sup> <sub>-0.20</sub>	130.9	-7.75 <sup>+0.44</sup> <sub>-0.58</sub>	-7.26 <sup>+0.24</sup> <sub>-0.25</sub>
404169737	62.148449	-53.873747	0.75002	22.097	10.09 <sup>+0.15</sup> <sub>-0.19</sub>	155.0	-7.95 <sup>+0.49</sup> <sub>-0.70</sub>	-7.26 <sup>+0.22</sup> <sub>-0.25</sub>
MUSE28/488067056	62.107634	-53.905654	1.25400	23.100	9.45 <sup>+0.23</sup> <sub>-0.25</sub>	42.0	-8.52 <sup>+0.65</sup> <sub>-1.00</sub>	-7.26 <sup>+0.25</sup> <sub>-0.28</sub>
404169584	62.156567	-53.871330	0.80070	21.188	10.48 <sup>+0.29</sup> <sub>-0.13</sub>	174.0	-7.70 <sup>+0.49</sup> <sub>-0.52</sub>	-7.27 <sup>+0.28</sup> <sub>-0.22</sub>
405340085	62.140943	-53.880240	0.30034	21.842	8.88 <sup>+0.18</sup> <sub>-0.13</sub>	128.4	-9.04 <sup>+0.55</sup> <sub>-0.74</sub>	-7.27 <sup>+0.24</sup> <sub>-0.22</sub>
488077259	62.092037	-53.945258	0.54971	22.234	9.56 <sup>+0.15</sup> <sub>-0.18</sub>	163.4	-8.44 <sup>+0.59</sup> <sub>-0.91</sub>	-7.28 <sup>+0.22</sup> <sub>-0.24</sub>
489521272	62.090218	-53.862527	0.63286	22.813	9.36 <sup>+0.23</sup> <sub>-0.25</sub>	134.5	-8.64 <sup>+0.66</sup> <sub>-1.02</sub>	-7.30 <sup>+0.25</sup> <sub>-0.28</sub>
489523103	62.037949	-53.878208	0.89700	21.083	10.30 <sup>+0.13</sup> <sub>-0.17</sub>	136.0	-7.83 <sup>+0.43</sup> <sub>-0.58</sub>	-7.31 <sup>+0.22</sup> <sub>-0.24</sub>
488076578	62.107604	-53.941787	0.79782	21.477	10.19 <sup>+0.14</sup> <sub>-0.16</sub>	155.2	-7.91 <sup>+0.47</sup> <sub>-0.64</sub>	-7.32 <sup>+0.22</sup> <sub>-0.23</sub>
489521533	62.082318	-53.864622	0.67459	23.344	9.38 <sup>+0.26</sup> <sub>-0.28</sub>	128.1	-8.65 <sup>+0.68</sup> <sub>-1.05</sub>	-7.33 <sup>+0.27</sup> <sub>-0.29</sub>
489522088	62.038672	-53.869800	0.59969	22.534	9.40 <sup>+0.27</sup> <sub>-0.25</sub>	154.2	-8.66 <sup>+0.68</sup> <sub>-1.02</sub>	-7.36 <sup>+0.27</sup> <sub>-0.28</sub>
488072301	62.160850	-53.917944	0.59760	22.185	9.47 <sup>+0.16</sup> <sub>-0.18</sub>	162.9	-8.61 <sup>+0.61</sup> <sub>-0.93</sub>	-7.37 <sup>+0.23</sup> <sub>-0.24</sub>
404169401	62.147459	-53.869008	0.75141	21.712	10.05 <sup>+0.24</sup> <sub>-0.28</sub>	164.3	-8.10 <sup>+0.57</sup> <sub>-0.82</sub>	-7.38 <sup>+0.26</sup> <sub>-0.29</sub>
404169402	62.130404	-53.867675	0.59397	23.104	9.20 <sup>+0.26</sup> <sub>-0.33</sub>	143.7	-8.88 <sup>+0.68</sup> <sub>-1.12</sub>	-7.40 <sup>+0.27</sup> <sub>-0.32</sub>
404169758	62.146052	-53.874054	0.75095	22.586	9.85 <sup>+0.16</sup> <sub>-0.21</sub>	150.3	-8.31 <sup>+0.55</sup> <sub>-0.82</sub>	-7.40 <sup>+0.23</sup> <sub>-0.25</sub>
404169588	62.151601	-53.871104	0.56693	22.810	9.40 <sup>+0.18</sup> <sub>-0.19</sub>	166.1	-8.73 <sup>+0.62</sup> <sub>-0.95</sub>	-7.43 <sup>+0.23</sup> <sub>-0.25</sub>
488076552	62.105955	-53.941347	0.36171	22.388	9.03 <sup>+0.16</sup> <sub>-0.17</sub>	152.8	-9.06 <sup>+0.59</sup> <sub>-0.89</sub>	-7.43 <sup>+0.23</sup> <sub>-0.24</sub>
488078159	62.047075	-53.950191	0.56953	21.811	9.71 <sup>+0.09</sup> <sub>-0.12</sub>	203.1	-8.49 <sup>+0.54</sup> <sub>-0.80</sub>	-7.46 <sup>+0.21</sup> <sub>-0.22</sub>
489522305	62.030458	-53.871796	0.91911	22.148	10.48 <sup>+0.19</sup> <sub>-0.38</sub>	162.5	-7.90 <sup>+0.43</sup> <sub>-0.70</sub>	-7.46 <sup>+0.24</sup> <sub>-0.35</sub>
488073582	62.036870	-53.925643	0.91818	21.953	10.27 <sup>+0.18</sup> <sub>-0.28</sub>	146.6	-8.01 <sup>+0.45</sup> <sub>-0.66</sub>	-7.48 <sup>+0.23</sup> <sub>-0.29</sub>
489522522	62.023889	-53.873587	0.59935	22.742	9.35 <sup>+0.18</sup> <sub>-0.25</sub>	170.0	-8.87 <sup>+0.63</sup> <sub>-1.03</sub>	-7.52 <sup>+0.24</sup> <sub>-0.28</sub>
488075100	62.135113	-53.933925	0.42804	22.300	8.97 <sup>+0.07</sup> <sub>-0.07</sub>	154.9	-9.22 <sup>+0.54</sup> <sub>-0.79</sub>	-7.54 <sup>+0.21</sup> <sub>-0.21</sub>
404168970	62.143547	-53.858498	0.84037	22.020	10.35 <sup>+0.16</sup> <sub>-0.17</sub>	186.9	-8.04 <sup>+0.43</sup> <sub>-0.57</sub>	-7.55 <sup>+0.23</sup> <sub>-0.24</sub>
404169534	62.142829	-53.870321	0.80082	21.848	9.86 <sup>+0.19</sup> <sub>-0.17</sub>	153.9	-8.45 <sup>+0.56</sup> <sub>-0.78</sub>	-7.55 <sup>+0.24</sup> <sub>-0.24</sub>
488073010	62.046958	-53.922500	0.27124	22.409	8.37 <sup>+0.16</sup> <sub>-0.14</sub>	123.0	-9.78 <sup>+0.25</sup> <sub>-0.22</sub>	-7.56 <sup>+0.23</sup> <sub>-0.23</sub>
488079339	62.108903	-53.956880	0.42895	21.139	9.48 <sup>+0.09</sup> <sub>-0.08</sub>	208.9	-8.80 <sup>+0.58</sup> <sub>-0.86</sub>	-7.56 <sup>+0.21</sup> <sub>-0.21</sub>
488070430	62.027802	-53.906937	0.95625	22.490	10.13 <sup>+0.21</sup> <sub>-0.32</sub>	135.2	-8.23 <sup>+0.53</sup> <sub>-0.84</sub>	-7.57 <sup>+0.24</sup> <sub>-0.31</sub>
488071245	62.030863	-53.912062	0.77531	22.736	9.46 <sup>+0.25</sup> <sub>-0.19</sub>	133.7	-8.84 <sup>+0.66</sup> <sub>-0.94</sub>	-7.59 <sup>+0.26</sup> <sub>-0.25</sub>
488078889	62.046282	-53.955925	0.19565	20.697	9.31 <sup>+0.10</sup> <sub>-0.10</sub>	222.4	-8.98 <sup>+0.59</sup> <sub>-0.90</sub>	-7.60 <sup>+0.21</sup> <sub>-0.21</sub>
489521965	62.045558	-53.868686	0.89759	22.513	10.04 <sup>+0.21</sup> <sub>-0.24</sub>	147.2	-8.33 <sup>+0.55</sup> <sub>-0.78</sub>	-7.60 <sup>+0.25</sup> <sub>-0.27</sub>
488065215	62.027412	-53.885104	1.10526	22.372	10.66 <sup>+0.26</sup> <sub>-0.37</sub>	143.9	-7.99 <sup>+0.45</sup> <sub>-0.67</sub>	-7.63 <sup>+0.27</sup> <sub>-0.34</sub>
488075166	62.149266	-53.934182	0.50880	22.887	9.14 <sup>+0.19</sup> <sub>-0.24</sub>	175.5	-9.18 <sup>+0.63</sup> <sub>-1.00</sub>	-7.64 <sup>+0.24</sup> <sub>-0.27</sub>
488068535	62.149540	-53.895034	0.77707	22.702	9.28 <sup>+0.24</sup> <sub>-0.22</sub>	126.6	-9.06 <sup>+0.66</sup> <sub>-0.99</sub>	-7.65 <sup>+0.26</sup> <sub>-0.26</sub>
488073904	62.151510	-53.927139	0.27214	22.822	8.74 <sup>+0.12</sup> <sub>-0.16</sub>	162.5	-9.55 <sup>+0.43</sup> <sub>-0.58</sub>	-7.66 <sup>+0.22</sup> <sub>-0.23</sub>



488068835	62.019738	-53.894319	0.91905	22.531	10.05 <sup>+0.21</sup> <sub>-0.26</sub>	151.3	-8.40 <sup>+0.54</sup> <sub>-0.80</sub>	-7.68 <sup>+0.25</sup> <sub>-0.28</sub>
405340125	62.147848	-53.880963	0.82674	22.738	9.58 <sup>+0.23</sup> <sub>-0.27</sub>	139.6	-8.83 <sup>+0.64</sup> <sub>-0.99</sub>	-7.69 <sup>+0.26</sup> <sub>-0.29</sub>
488076126	62.098545	-53.939165	0.29568	22.286	8.45 <sup>+0.12</sup> <sub>-0.11</sub>	142.4	-9.86 <sup>+0.19</sup> <sub>-0.18</sub>	-7.71 <sup>+0.21</sup> <sub>-0.22</sub>
488074972	62.158897	-53.933231	0.27187	22.261	8.93 <sup>+0.11</sup> <sub>-0.13</sub>	188.4	-9.43 <sup>+0.54</sup> <sub>-0.79</sub>	-7.71 <sup>+0.21</sup> <sub>-0.22</sub>
488073464	62.128601	-53.924891	1.08324	22.899	10.15 <sup>+0.25</sup> <sub>-0.33</sub>	121.1	-8.35 <sup>+0.57</sup> <sub>-0.85</sub>	-7.72 <sup>+0.26</sup> <sub>-0.32</sub>
488072862	62.014278	-53.921997	0.44369	22.954	8.99 <sup>+0.17</sup> <sub>-0.23</sub>	180.0	-9.41 <sup>+0.59</sup> <sub>-0.92</sub>	-7.73 <sup>+0.23</sup> <sub>-0.26</sub>
488071425	62.019165	-53.913520	0.77498	22.912	9.57 <sup>+0.18</sup> <sub>-0.24</sub>	158.9	-8.89 <sup>+0.60</sup> <sub>-0.96</sub>	-7.74 <sup>+0.23</sup> <sub>-0.27</sub>
488077585	62.091222	-53.947042	0.85319	23.034	9.94 <sup>+0.17</sup> <sub>-0.20</sub>	169.8	-8.57 <sup>+0.54</sup> <sub>-0.77</sub>	-7.75 <sup>+0.23</sup> <sub>-0.25</sub>
404169398	62.129582	-53.867590	1.04896	22.750	10.28 <sup>+0.30</sup> <sub>-0.36</sub>	142.9	-8.28 <sup>+0.51</sup> <sub>-0.72</sub>	-7.75 <sup>+0.29</sup> <sub>-0.34</sub>
488076873	62.062246	-53.943414	0.51666	22.956	8.90 <sup>+0.28</sup> <sub>-0.27</sub>	167.7	-9.51 <sup>+0.64</sup> <sub>-0.89</sub>	-7.76 <sup>+0.28</sup> <sub>-0.28</sub>
404169833	62.165627	-53.875815	0.61452	22.767	9.16 <sup>+0.22</sup> <sub>-0.18</sub>	181.6	-9.30 <sup>+0.65</sup> <sub>-0.95</sub>	-7.78 <sup>+0.25</sup> <sub>-0.24</sub>
488074337	62.173464	-53.929392	0.40472	22.616	9.08 <sup>+0.15</sup> <sub>-0.17</sub>	205.6	-9.40 <sup>+0.60</sup> <sub>-0.92</sub>	-7.81 <sup>+0.22</sup> <sub>-0.24</sub>
488067934	62.032469	-53.898319	1.34023	21.519	10.94 <sup>+0.05</sup> <sub>-0.04</sub>	123.0	-8.04 <sup>+0.32</sup> <sub>-0.39</sub>	-7.81 <sup>+0.20</sup> <sub>-0.20</sub>
488077841	62.133208	-53.947857	0.35684	22.687	8.91 <sup>+0.17</sup> <sub>-0.23</sub>	195.1	-9.57 <sup>+0.56</sup> <sub>-0.85</sub>	-7.83 <sup>+0.23</sup> <sub>-0.26</sub>
488070960	62.031874	-53.910446	1.23026	21.226	10.58 <sup>+0.19</sup> <sub>-0.19</sub>	129.8	-8.25 <sup>+0.42</sup> <sub>-0.54</sub>	-7.86 <sup>+0.24</sup> <sub>-0.25</sub>
489521442	62.031862	-53.864100	0.90591	22.699	9.96 <sup>+0.24</sup> <sub>-0.26</sub>	179.0	-8.74 <sup>+0.58</sup> <sub>-0.83</sub>	-7.94 <sup>+0.26</sup> <sub>-0.28</sub>
488076117	62.040622	-53.939310	1.01820	22.596	10.24 <sup>+0.18</sup> <sub>-0.21</sub>	176.9	-8.54 <sup>+0.49</sup> <sub>-0.67</sub>	-7.99 <sup>+0.23</sup> <sub>-0.26</sub>
404169065	62.156908	-53.860476	0.75027	22.948	9.44 <sup>+0.23</sup> <sub>-0.25</sub>	200.1	-9.34 <sup>+0.65</sup> <sub>-1.01</sub>	-8.07 <sup>+0.25</sup> <sub>-0.28</sub>
489520262	62.067931	-53.853616	0.91854	22.457	9.71 <sup>+0.25</sup> <sub>-0.23</sub>	173.3	-9.12 <sup>+0.63</sup> <sub>-0.89</sub>	-8.10 <sup>+0.26</sup> <sub>-0.26</sub>
404169193	62.141088	-53.862996	1.16021	22.384	10.50 <sup>+0.21</sup> <sub>-0.30</sub>	170.9	-8.52 <sup>+0.44</sup> <sub>-0.63</sub>	-8.10 <sup>+0.25</sup> <sub>-0.30</sub>
404169489	62.136503	-53.870431	0.04355	21.430	7.60 <sup>+0.37</sup> <sub>-0.32</sub>	144.3	-11.07 <sup>+0.59</sup> <sub>-0.51</sub>	-8.16 <sup>+0.32</sup> <sub>-0.31</sub>
404169659	62.146071	-53.872477	1.14904	21.682	9.98 <sup>+0.17</sup> <sub>-0.22</sub>	153.9	-9.09 <sup>+0.53</sup> <sub>-0.78</sub>	-8.31 <sup>+0.23</sup> <sub>-0.26</sub>
488075055	62.169444	-53.933578	1.03614	22.691	10.13 <sup>+0.17</sup> <sub>-0.32</sub>	206.8	-8.97 <sup>+0.50</sup> <sub>-0.84</sub>	-8.32 <sup>+0.23</sup> <sub>-0.31</sub>
404169176	62.145040	-53.862782	1.14723	22.928	10.20 <sup>+0.24</sup> <sub>-0.30</sub>	176.9	-8.92 <sup>+0.55</sup> <sub>-0.80</sub>	-8.33 <sup>+0.26</sup> <sub>-0.30</sub>
404169154	62.149335	-53.862340	1.14884	22.251	9.78 <sup>+0.20</sup> <sub>-0.24</sub>	184.1	-9.66 <sup>+0.59</sup> <sub>-0.88</sub>	-8.69 <sup>+0.24</sup> <sub>-0.27</sub>
488073779	62.020985	-53.927277	1.38408	22.280	10.52 <sup>+0.18</sup> <sub>-0.24</sub>	177.2	-9.12 <sup>+0.42</sup> <sub>-0.58</sub>	-8.70 <sup>+0.23</sup> <sub>-0.27</sub>
488072310	62.161986	-53.918003	1.25287	22.603	9.08 <sup>+0.18</sup> <sub>-0.14</sub>	165.2	-10.89 <sup>+0.61</sup> <sub>-0.89</sub>	-9.31 <sup>+0.23</sup> <sub>-0.23</sub>
488072700	62.160696	-53.920293	1.25468	22.908	9.07 <sup>+0.25</sup> <sub>-0.24</sub>	166.2	-10.93 <sup>+0.66</sup> <sub>-0.98</sub>	-9.33 <sup>+0.26</sup> <sub>-0.27</sub>
488072408	62.161866	-53.918519	1.25018	22.937	8.95 <sup>+0.18</sup> <sub>-0.19</sub>	165.7	-11.10 <sup>+0.58</sup> <sub>-0.86</sub>	-9.40 <sup>+0.24</sup> <sub>-0.25</sub>
404169985	62.153722	-53.878539	1.41999	22.613	9.23 <sup>+0.26</sup> <sub>-0.24</sub>	154.7	-11.00 <sup>+0.68</sup> <sub>-1.02</sub>	-9.55 <sup>+0.27</sup> <sub>-0.27</sub>
489520462	62.073666	-53.855405	1.17034	22.110	7.69 <sup>+0.45</sup> <sub>-0.45</sub>	164.0	-12.93 <sup>+0.72</sup> <sub>-0.72</sub>	-10.10 <sup>+0.37</sup> <sub>-0.39</sub>
489520752	62.055153	-53.858062	1.59303	22.328	9.14 <sup>+0.29</sup> <sub>-0.23</sub>	168.1	-11.75 <sup>+0.70</sup> <sub>-0.99</sub>	-10.21 <sup>+0.28</sup> <sub>-0.27</sub>
3070263610	62.040098	-53.885262	1.32360	-	-	119.0	-	-
3070263850	62.075161	-53.892278	0.91583	-	-	42.4	-	-
3070265512	62.076105	-53.885866	0.91540	-	-	58.9	-	-
3070264072	62.073661	-53.889176	0.76790	-	-	52.4	-	-
MUSE1	62.093482	-53.907716	0.23983	-	-	28.9	-	-
MUSE2	62.088497	-53.889554	0.28757	-	-	37.4	-	-
MUSE4	62.079502	-53.896486	0.55446	-	-	26.2	-	-
MUSE5	62.092164	-53.902560	0.59221	-	-	10.3	-	-
MUSE7	62.086607	-53.902732	0.59822	-	-	13.0	-	-

MUSE11	62.092623	-53.909149	0.64338	-	-	33.7	-	-
MUSE13	62.088612	-53.911555	0.76379	-	-	42.2	-	-
MUSE16	62.075319	-53.889095	0.76863	-	-	50.4	-	-
MUSE17	62.095373	-53.907544	0.82980	-	-	29.5	-	-
MUSE18	62.069991	-53.898778	0.85458	-	-	43.5	-	-
MUSE23	62.082424	-53.891043	1.13208	-	-	36.1	-	-
MUSE27	62.084658	-53.911326	1.25152	-	-	42.9	-	-
WGD 2038–4008								
169190452	309.539131	-40.115839	0.22917	18.213	10.76 <sup>+0.04</sup> <sub>-0.04</sub>	107.9	-6.39 <sup>+0.35</sup> <sub>-0.43</sub>	-6.08 <sup>+0.20</sup> <sub>-0.20</sub>
169192596	309.492815	-40.140131	0.23003	21.389	9.28 <sup>+0.11</sup> <sub>-0.18</sub>	52.3	-7.61 <sup>+0.60</sup> <sub>-0.96</sub>	-6.21 <sup>+0.21</sup> <sub>-0.24</sub>
169191228	309.535586	-40.122881	0.22900	20.025	10.13 <sup>+0.07</sup> <sub>-0.11</sub>	83.9	-6.86 <sup>+0.45</sup> <sub>-0.62</sub>	-6.21 <sup>+0.21</sup> <sub>-0.22</sub>
169189459	309.539963	-40.103707	0.22827	17.848	11.00 <sup>+0.04</sup> <sub>-0.04</sub>	143.5	-6.47 <sup>+0.30</sup> <sub>-0.37</sub>	-6.27 <sup>+0.20</sup> <sub>-0.20</sub>
169192249	309.537431	-40.135642	0.22864	21.077	9.60 <sup>+0.08</sup> <sub>-0.09</sub>	71.9	-7.50 <sup>+0.56</sup> <sub>-0.82</sub>	-6.38 <sup>+0.21</sup> <sub>-0.21</sub>
169192351	309.523347	-40.137071	0.42874	20.494	10.12 <sup>+0.10</sup> <sub>-0.12</sub>	32.9	-7.05 <sup>+0.46</sup> <sub>-0.63</sub>	-6.39 <sup>+0.21</sup> <sub>-0.22</sub>
169191897	309.517763	-40.130806	0.34445	22.210	8.69 <sup>+0.13</sup> <sub>-0.12</sub>	28.5	-8.56 <sup>+0.40</sup> <sub>-0.49</sub>	-6.63 <sup>+0.22</sup> <sub>-0.22</sub>
169193594	309.514195	-40.155037	0.27820	21.126	9.31 <sup>+0.11</sup> <sub>-0.13</sub>	65.3	-8.19 <sup>+0.60</sup> <sub>-0.92</sub>	-6.81 <sup>+0.21</sup> <sub>-0.22</sub>
169194640	309.471495	-40.170293	0.23647	19.289	10.42 <sup>+0.06</sup> <sub>-0.06</sub>	162.4	-7.38 <sup>+0.39</sup> <sub>-0.51</sub>	-6.91 <sup>+0.20</sup> <sub>-0.21</sub>
169192636	309.498710	-40.140676	0.42710	22.669	9.45 <sup>+0.16</sup> <sub>-0.26</sub>	37.3	-8.27 <sup>+0.61</sup> <sub>-1.01</sub>	-7.02 <sup>+0.23</sup> <sub>-0.28</sub>
169193902	309.487074	-40.160804	0.42725	18.676	11.35 <sup>+0.03</sup> <sub>-0.03</sub>	108.6	-7.09 <sup>+0.24</sup> <sub>-0.27</sub>	-7.04 <sup>+0.20</sup> <sub>-0.20</sub>
169191786	309.521701	-40.129094	0.34157	22.937	8.60 <sup>+0.23</sup> <sub>-0.18</sub>	40.3	-9.15 <sup>+0.43</sup> <sub>-0.40</sub>	-7.13 <sup>+0.26</sup> <sub>-0.24</sub>
169191437	309.540911	-40.125437	0.22716	21.577	8.65 <sup>+0.10</sup> <sub>-0.10</sub>	91.4	-9.34 <sup>+0.33</sup> <sub>-0.39</sub>	-7.37 <sup>+0.21</sup> <sub>-0.21</sub>
169193432	309.557474	-40.152652	0.34079	19.475	10.47 <sup>+0.07</sup> <sub>-0.07</sub>	138.8	-7.83 <sup>+0.39</sup> <sub>-0.50</sub>	-7.39 <sup>+0.21</sup> <sub>-0.21</sub>
169194065	309.562909	-40.162398	0.34506	19.299	10.78 <sup>+0.07</sup> <sub>-0.05</sub>	168.7	-7.75 <sup>+0.35</sup> <sub>-0.43</sub>	-7.45 <sup>+0.20</sup> <sub>-0.20</sub>
169191326	309.496715	-40.122896	0.34271	22.345	8.96 <sup>+0.18</sup> <sub>-0.19</sub>	64.9	-9.20 <sup>+0.58</sup> <sub>-0.86</sub>	-7.50 <sup>+0.23</sup> <sub>-0.25</sub>
169189145	309.516470	-40.095073	0.20084	19.786	9.31 <sup>+0.11</sup> <sub>-0.11</sub>	151.7	-8.89 <sup>+0.60</sup> <sub>-0.91</sub>	-7.51 <sup>+0.21</sup> <sub>-0.22</sub>
169192814	309.520646	-40.143046	0.52902	22.046	9.57 <sup>+0.20</sup> <sub>-0.22</sub>	33.5	-8.75 <sup>+0.62</sup> <sub>-0.94</sub>	-7.60 <sup>+0.24</sup> <sub>-0.26</sub>
169194067	309.482408	-40.160695	0.07580	20.890	8.19 <sup>+0.26</sup> <sub>-0.19</sub>	116.7	-10.15 <sup>+0.41</sup> <sub>-0.31</sub>	-7.77 <sup>+0.27</sup> <sub>-0.25</sub>
169193455	309.496328	-40.151391	0.36829	22.005	8.79 <sup>+0.11</sup> <sub>-0.12</sub>	66.3	-9.68 <sup>+0.46</sup> <sub>-0.62</sub>	-7.83 <sup>+0.21</sup> <sub>-0.22</sub>
169189914	309.518874	-40.103760	0.19742	22.878	8.00 <sup>+0.20</sup> <sub>-0.17</sub>	121.5	-10.71 <sup>+0.32</sup> <sub>-0.27</sub>	-8.16 <sup>+0.24</sup> <sub>-0.24</sub>
169194531	309.503092	-40.167505	0.42654	21.622	9.83 <sup>+0.10</sup> <sub>-0.12</sub>	112.1	-9.10 <sup>+0.52</sup> <sub>-0.75</sub>	-8.18 <sup>+0.21</sup> <sub>-0.22</sub>
169189067	309.542813	-40.092954	0.28598	21.217	9.10 <sup>+0.14</sup> <sub>-0.12</sub>	180.7	-9.92 <sup>+0.60</sup> <sub>-0.89</sub>	-8.35 <sup>+0.22</sup> <sub>-0.22</sub>
169193237	309.561418	-40.148516	0.34018	22.225	9.14 <sup>+0.12</sup> <sub>-0.14</sub>	143.8	-9.92 <sup>+0.59</sup> <sub>-0.91</sub>	-8.39 <sup>+0.22</sup> <sub>-0.23</sub>
169193555	309.568673	-40.153285	0.34218	21.564	9.39 <sup>+0.12</sup> <sub>-0.14</sub>	168.2	-9.75 <sup>+0.59</sup> <sub>-0.92</sub>	-8.43 <sup>+0.21</sup> <sub>-0.23</sub>
169191966	309.541745	-40.132233	0.60086	20.513	10.76 <sup>+0.07</sup> <sub>-0.23</sub>	85.3	-9.01 <sup>+0.35</sup> <sub>-0.52</sub>	-8.70 <sup>+0.21</sup> <sub>-0.26</sub>
169189826	309.535769	-40.102557	0.47794	22.031	9.99 <sup>+0.08</sup> <sub>-0.09</sub>	141.1	-9.52 <sup>+0.48</sup> <sub>-0.67</sub>	-8.75 <sup>+0.21</sup> <sub>-0.21</sub>
169193901	309.570179	-40.158238	0.47405	21.269	10.18 <sup>+0.09</sup> <sub>-0.11</sub>	178.9	-9.50 <sup>+0.44</sup> <sub>-0.60</sub>	-8.89 <sup>+0.21</sup> <sub>-0.22</sub>
169189023	309.491739	-40.092652	0.54487	20.724	10.80 <sup>+0.03</sup> <sub>-0.03</sub>	168.6	-9.26 <sup>+0.34</sup> <sub>-0.42</sub>	-8.97 <sup>+0.20</sup> <sub>-0.20</sub>
169193078	309.564077	-40.146099	0.34071	22.869	8.37 <sup>+0.14</sup> <sub>-0.14</sub>	148.7	-11.21 <sup>+0.23</sup> <sub>-0.23</sub>	-8.99 <sup>+0.22</sup> <sub>-0.23</sub>
169191992	309.457026	-40.131800	0.51834	21.469	9.85 <sup>+0.11</sup> <sub>-0.13</sub>	150.8	-10.17 <sup>+0.52</sup> <sub>-0.75</sub>	-9.27 <sup>+0.21</sup> <sub>-0.22</sub>
169191596	309.458841	-40.126588	0.48342	22.409	8.93 <sup>+0.18</sup> <sub>-0.17</sub>	149.4	-11.35 <sup>+0.57</sup> <sub>-0.82</sub>	-9.63 <sup>+0.23</sup> <sub>-0.24</sub>
169193763	309.500311	-40.155916	0.67100	22.476	9.75 <sup>+0.27</sup> <sub>-0.19</sub>	74.5	-11.24 <sup>+0.65</sup> <sub>-0.84</sub>	-10.25 <sup>+0.28</sup> <sub>-0.25</sub>

169189572	309.526023	-40.099386	0.62258	20.045	9.74 <sup>+0.07</sup> <sub>-0.05</sub>	141.4	-11.35 <sup>+0.53</sup> <sub>-0.75</sub>	-10.35 <sup>+0.20</sup> <sub>-0.20</sub>
169192546	309.545721	-40.139586	0.67484	21.345	10.03 <sup>+0.11</sup> <sub>-0.16</sub>	95.0	-11.16 <sup>+0.48</sup> <sub>-0.70</sub>	-10.43 <sup>+0.21</sup> <sub>-0.23</sub>
169194605	309.556455	-40.168268	0.60064	22.811	9.43 <sup>+0.21</sup> <sub>-0.27</sub>	167.4	-11.80 <sup>+0.64</sup> <sub>-1.02</sub>	-10.52 <sup>+0.25</sup> <sub>-0.28</sub>
14	309.515660	-40.134512	0.77392	21.462	10.55 <sup>+0.08</sup> <sub>-0.12</sub>	14.9	-14.27 <sup>+0.38</sup> <sub>-0.50</sub>	-13.87 <sup>+0.21</sup> <sub>-0.22</sub>
13	309.515880	-40.135034	0.77492	20.761	11.32 <sup>+0.05</sup> <sub>-0.06</sub>	14.3	-14.00 <sup>+0.24</sup> <sub>-0.29</sub>	-13.94 <sup>+0.20</sup> <sub>-0.20</sub>
169194395	309.544629	-40.165182	0.76076	22.386	10.04 <sup>+0.32</sup> <sub>-0.18</sub>	136.6	-14.95 <sup>+0.66</sup> <sub>-0.71</sub>	-14.22 <sup>+0.30</sup> <sub>-0.24</sub>
169194256	309.543818	-40.163338	0.76067	22.326	9.84 <sup>+0.19</sup> <sub>-0.27</sub>	130.2	-15.19 <sup>+0.57</sup> <sub>-0.29</sub>	-14.29 <sup>+0.24</sup> <sub>-0.29</sub>
15	309.516878	-40.135319	0.77619	22.884	10.18 <sup>+0.13</sup> <sub>-0.20</sub>	16.3	-17.18 <sup>+0.46</sup> <sub>-0.69</sub>	-16.58 <sup>+0.22</sup> <sub>-0.25</sub>
169190526	309.539140	-40.111919	0.91987	21.537	10.65 <sup>+0.18</sup> <sub>-0.33</sub>	118.4	-	-
169190626	309.551365	-40.113228	0.78249	22.480	9.87 <sup>+0.21</sup> <sub>-0.30</sub>	139.5	-	-
169190809	309.511333	-40.116436	0.81855	20.801	10.56 <sup>+0.18</sup> <sub>-0.24</sub>	74.1	-	-
169195181	309.510546	-40.177017	1.17836	22.655	9.61 <sup>+0.15</sup> <sub>-0.17</sub>	144.0	-	-
169192635	309.485842	-40.140711	1.35058	20.463	7.58 <sup>+0.37</sup> <sub>-0.41</sub>	71.5	-	-
169196130	309.490867	-40.190128	0.81949	21.775	10.90 <sup>+0.04</sup> <sub>-0.05</sub>	199.3	-	-
169195495	309.501974	-40.181155	0.92178	21.862	9.98 <sup>+0.19</sup> <sub>-0.16</sub>	161.0	-	-
169195905	309.520673	-40.186885	0.82054	21.349	10.42 <sup>+0.15</sup> <sub>-0.20</sub>	181.3	-	-
169194113	309.498489	-40.161174	0.87838	22.655	10.00 <sup>+0.22</sup> <sub>-0.26</sub>	93.9	-	-
169194495	309.511978	-40.166836	1.13033	22.524	10.29 <sup>+0.24</sup> <sub>-0.27</sub>	107.3	-	-
169193629	309.483800	-40.153801	0.82247	21.200	10.41 <sup>+0.16</sup> <sub>-0.16</sub>	97.0	-	-
169196183	309.518797	-40.190901	0.97564	21.295	10.77 <sup>+0.24</sup> <sub>-0.32</sub>	195.0	-	-
169192350	309.514393	-40.137815	-9.00000	-	-	8.8	-	-

Table A2: Properties of galaxies in each trial group. The columns display, in order, the coordinates (RA, DEC in degrees; ICRS), redshift  $z$ , DES  $i$ -band MOF\_CM\_MAG\_CORRECTED magnitudes (if available; assigned a value of -99 if not), ID, and whether that galaxy passes the iterative group membership algorithm described in §5.1. Spectroscopic redshift uncertainties are about  $100 \text{ km s}^{-1}$ , or 0.00033 in redshift. Galaxies with DES Y3 IDs have 9 digits, while galaxies with DES Y1 IDs have 10 digits. The lens galaxy is indicated as such, and galaxies with spectroscopic redshifts from MUSE have IDs that begin with "MUSE"

RA	DEC	$z$	$i$ -band Mag	ID	Group Member?
DES J0408–5354					
Group 1					
62.030809	-53.908820	0.26729	20.096	488070602	False
62.084697	-53.867583	0.27148	21.675	489521853	True
62.061177	-53.921532	0.27257	19.767	488072697	True
62.144676	-53.934498	0.27176	18.315	488074578	True
62.084648	-53.885204	0.27247	18.309	488070148	True
62.097716	-53.879281	0.27278	22.768	489523301	True
62.046958	-53.922500	0.27124	22.409	488073010	True
62.092960	-53.861224	0.27153	20.306	489521068	True
62.054344	-53.919213	0.27226	22.046	488072443	True
62.151510	-53.927139	0.27214	22.822	488073904	True

62.146922	-53.934938	0.27044	19.713	488074678	False
62.158897	-53.933231	0.27187	22.261	488074972	True
62.083413	-53.882657	0.27216	22.456	488069700	True
Group 2					
62.049904	-53.911313	0.30581	21.203	488071089	True
62.045447	-53.913359	0.30642	21.438	488071411	True
62.080583	-53.922670	0.30741	21.184	488073021	True
62.093088	-53.919040	0.30909	21.573	488072433	True
62.096336	-53.944173	0.30792	19.259	488076699	True
62.020675	-53.907526	0.30566	19.692	488067185	True
Group 3					
62.139479	-53.928501	0.42858	19.429	488073735	True
62.025309	-53.910519	0.42954	19.664	488070449	False
62.114845	-53.953040	0.42826	21.346	488078736	True
62.108903	-53.956880	0.42895	21.139	488079339	True
62.131777	-53.926465	0.42904	21.665	488073762	True
62.148320	-53.919275	0.42744	20.060	488072414	True
62.133767	-53.937477	0.42807	20.447	488075668	True
62.135113	-53.933925	0.42804	22.300	488075100	True
62.140970	-53.931443	0.43054	20.683	488074608	False
Group 4					
62.106161	-53.923866	0.57035	20.933	488073290	True
62.023367	-53.910705	0.57025	19.314	488066235	True
62.151601	-53.871104	0.56693	22.810	404169588	False
62.047075	-53.950191	0.56953	21.811	488078159	True
62.017973	-53.905064	0.57028	21.306	488066250	True
62.019121	-53.902892	0.57171	21.720	488067945	True
Group 5					
62.037079	-53.908383	0.59964	22.356	488070607	True
62.169886	-53.887360	0.59607	20.158	488070133	True
62.160850	-53.917944	0.59760	22.185	488072301	True
62.130404	-53.867675	0.59397	23.104	404169402	False
62.035444	-53.909470	0.60004	22.347	488070816	True
62.068708	-53.913477	0.59843	21.581	488071428	True
62.071692	-53.906245	0.59727	-9999.000	488066584	True
62.134647	-53.901754	0.59479	21.047	488067363	False
62.078380	-53.881917	0.59451	19.918	489523481	False
62.072770	-53.910296	0.59811	19.975	488070807	True
62.083912	-53.903969	0.60048	22.304	488066462	True
62.067875	-53.910488	0.59977	21.729	488070966	True
62.038672	-53.869800	0.59969	22.534	489522088	True

62.023889	-53.873587	0.59935	22.742	489522522	True
62.095575	-53.898291	0.59441	21.867	488065185	False
62.090417	-53.899889	0.59671	19.770	Lens	True
62.092164	-53.902560	0.59221	-99.000	MUSE5	False
62.077898	-53.903878	0.59797	-99.000	MUSE6	True
62.086607	-53.902732	0.59822	-99.000	MUSE7	True
62.103108	-53.897861	0.59832	-99.000	MUSE8	True
62.085632	-53.891330	0.59906	-99.000	MUSE9	True
62.085862	-53.910180	0.60029	-99.000	MUSE10	True
Group 6					
62.148449	-53.873747	0.75002	22.097	404169737	True
62.113750	-53.913080	0.74981	22.287	488071415	False
62.147459	-53.869008	0.75141	21.712	404169401	True
62.156908	-53.860476	0.75027	22.948	404169065	False
62.146052	-53.874054	0.75095	22.586	404169758	True
62.108813	-53.919489	0.75070	22.550	488072531	False
Group 7					
62.106067	-53.909453	0.77562	21.908	488070825	False
62.158048	-53.912350	0.76818	18.274	488070947	False
62.125315	-53.873569	0.76243	22.755	404169734	False
62.073251	-53.920150	0.77290	22.129	488072604	False
62.090965	-53.901634	0.76866	20.096	488068102	True
62.050530	-53.926881	0.75824	22.336	488073766	False
62.090541	-53.904725	0.77568	22.925	488066886	False
62.030863	-53.912062	0.77531	22.736	488071245	False
62.019165	-53.913520	0.77498	22.912	488071425	False
62.090243	-53.903609	0.77069	22.015	488066144	False
62.073661	-53.889176	0.76790	-99.000	3070264072.0	True
62.088612	-53.911555	0.76379	-99.000	MUSE13	False
62.099785	-53.908977	0.76669	-99.000	MUSE14	True
62.080992	-53.904565	0.76785	-99.000	MUSE15	True
62.075319	-53.889095	0.76863	-99.000	MUSE16	True
Group 8					
62.142829	-53.870321	0.80082	21.848	404169534	True
62.107604	-53.941787	0.79782	21.477	488076578	True
62.171213	-53.906968	0.79737	22.595	488070460	True
62.156567	-53.871330	0.80070	21.188	404169584	True
62.112378	-53.871809	0.80252	21.675	404169634	True
62.171213	-53.906968	0.79720	22.595	488070460	True
Group 9					
62.036870	-53.925643	0.91818	21.953	488073582	True

62.043694	-53.923652	0.91456	22.098	488073160	True
62.025664	-53.892284	0.91979	21.768	488067796	True
62.030458	-53.871796	0.91911	22.148	489522305	True
62.019738	-53.894319	0.91905	22.531	488068835	True
62.067931	-53.853616	0.91854	22.457	489520262	True
62.075161	-53.892278	0.91583	-99.000	3070263850.0	True
62.076105	-53.885866	0.91540	-99.000	3070265512.0	True
62.088268	-53.890642	0.91504	-99.000	MUSE19	True
Group 10					
62.161866	-53.918519	1.25018	22.937	488072408	True
62.160696	-53.920293	1.25468	22.908	488072700	True
62.161986	-53.918003	1.25287	22.603	488072310	True
62.098868	-53.909951	1.25002	-99.000	MUSE25	True
62.095831	-53.909607	1.25062	-99.000	MUSE26	True
62.084658	-53.911326	1.25152	-99.000	MUSE27	True
62.107634	-53.905654	1.25400	-99.000	MUSE28	True
WGD 2038–4008					
Group 1					
309.492815	-40.140131	0.23003	21.389	169192596	True
309.539963	-40.103707	0.22827	17.848	169189459	True
309.539131	-40.115839	0.22917	18.213	169190452	True
309.535586	-40.122881	0.22900	20.025	169191228	True
309.540911	-40.125437	0.22716	21.577	169191437	True
309.537431	-40.135642	0.22864	21.077	169192249	True
309.511379	-40.137024	0.22829	–	169191076/Lens	True
Group 2					
309.521701	-40.129094	0.34157	22.937	169191786	True
309.517763	-40.130806	0.34445	22.210	169191897	True
309.564077	-40.146099	0.34071	22.869	169193078	True
309.561418	-40.148516	0.34018	22.225	169193237	True
309.557474	-40.152652	0.34079	19.475	169193432	True
309.496715	-40.122896	0.34271	22.345	169191326	True
309.568673	-40.153285	0.34218	21.564	169193555	True
309.562909	-40.162398	0.34506	19.299	169194065	True

1516 This paper has been typeset from a  $\text{\TeX}/\text{\LaTeX}$  file prepared by the author.

**Table A3.** Properties of redMaPPer clusters in the field of view of WGD 2038–4008. The columns show the cluster ID, cluster redshift, richness, velocity dispersion (rounded to the nearest  $10 \text{ km s}^{-1}$ ), the group centroid (in RA and Dec), projected distance of the centroid to the lens ( $\Delta\theta$ ), and flexion shift  $\log(\Delta_{3x}(\text{arcsec}))$ . See §6.3 for further discussion

MEM_MATCH_ID	$\bar{z}_{\text{group}}$	$\lambda$	$\sigma_{\text{group}}$ ( $\text{km s}^{-1}$ )	RA <sub>ctr</sub> , DEC <sub>ctr</sub> (deg)	$\Delta\theta$ (arcsec)	$\log_{10}(\Delta_{3x})$ ( $\log_{10}(\text{arcsec})$ )
62659	$0.221 \pm 0.008$	$5.1 \pm 1.7$	$340^{+60}_{-70}$	309.53913, -40.11584	107.9	$-5.1^{+0.3}_{-0.4}$
138669	$0.405 \pm 0.017$	$10.8 \pm 2.0$	$430^{+50}_{-60}$	309.48707, -40.16080	108.6	$-6.0 \pm 0.2$